8-2016

Low-dimensional Materials for Organic Electronic Applications

Sumit Beniwal
University of Nebraska-Lincoln, sbeniwal2@unl.edu

LOW-DIMENSIONAL MATERIALS FOR ORGANIC ELECTRONIC APPLICATIONS

by

Sumit Beniwal

A DISSERTATION

Presented to the Faculty of

The Graduate College at the University of Nebraska

In Partial Fulfilment of Requirements

For the Degree of Doctor of Philosophy

Major: Physics and Astronomy

Under the Supervision of Professor Axel Enders

Lincoln, Nebraska

August, 2016

LOW-DIMENSIONAL MATERIALS FOR ORGANIC ELECTRONIC APPLICATIONS

Sumit Beniwal, Ph.D.

University of Nebraska, 2016

Adviser: Axel Enders

This thesis explores the self-assembly, surface interactions and electronic properties of functional molecules that have potential applications in electronics. Three classes of molecules - organic ferroelectric, spin-crossover complex, and molecules that assemble into a 2D semiconductor, have been studied through scanning tunneling microscopy and surface-sensitive spectroscopic methods. The scientific goal of this thesis is to understand the self-assembly of these molecules in low-dimensional (2D) configurations and the influence of substrate on their properties.

First, a H-bonded organic ferroelectric, the 3-Hydroxyphenalenone, is studied on two noble metal substrates. It is demonstrated how a variety of different assemblies including 1D chains, π-π stacked structures and chiral network can be fabricated using the substrate as a growth parameter. Especially 1D chains are interesting as they still exhibit the structural motif that is the origin of their ferroelectric behavior in bulk, namely the coupling between the H-bonds and the molecular π electron system.

Second, the self-assembly of Fe(II) spin crossover complex is studied on Au(111) substrate. This organic complex can be reversibly switched between paramagnetic high-spin (S=2) and diamagnetic low-spin state (S=0) in the bulk. The magnetic and electronic properties of this complex were found to be drastically influenced by the substrate. Interestingly, the reversible spin-state transition is suppressed in the interfacial molecules, likely due to a conformational change these molecules experience when in contact with the substrate.

Third, the 2D boron containing semiconductors were synthesized by covalent linking of

boron based precursor molecules. Two molecules, bis-BN cyclohexane and m-carborane-9-thiol are studied on Ir(111) and Au(111) substrates, respectively. In the first case, the covalent bonding between de-hydrogenated bis-BN cyclohexane rings led to the formation of a new 2D B, C, and N containing material. This material is isostructural to graphene and h-BN, but with the useful band gap of 0.9 eV. In the second case, the m-carborane monolayer films were synthesized on Au(111). A microscopic study of the effect of the electron-induced crosslinking of the carborane cages and the resulting change in the HOMO-LUMO gap is presented. The significance of this study is in the relation it establishes between the structure and properties of these molecular systems on metal substrates through basic surface science, which will potentially enable multi-functional organic electronics applications.

Acknowledgements

First and foremost, I would like to offer my sincere appreciation and thanks to my advisor, Dr. Axel Enders. He has been a tremendous mentor for me by allowing me to grow as a researcher. Throughout my Ph.D., he has been very encouraging, supportive, and has given me freedom to pursue various projects without any objections. His scientific advice, knowledge and many insightful discussions and suggestions, have made this thesis possible. On a personal note, his warm and approachable personality has made working with him very enjoyable.

I would also like to thank my committee members, Dr. Peter Dowben, Dr. Shireen Adenwalla, and Dr. Alexander Sinitskii for their service both as committee members as well as mentors. Furthermore, I would like to thank my numerous collaborators Dr. Eva Zurek, Dr. James Hooper, Dr. Shuang Chen, Dr. Xiao Cheng Zheng, and Dr. Sai Mu for providing theoretical insights into my research, which added significant value to my thesis. Aside from the committee service, I also would like to thank Dr. Peter Dowben and his student Xin Zhang for their scientific collaborations.

I would like to thank my former lab mate Donna Kunkel for training me on the instrumentation, helping me in various aspects of research and valuable scientific discussions. I would also like to thank my fellow researcher Paulo Costa who aided me in everything from routine maintenance of instruments to providing valuable scientific discussions. Finally, I wish to sincerely thank my wife, my family and friends for providing unconditional support during my graduate years. With that, to everyone mentioned above: Thank you!

Table of Contents

List of Figures

List of Tables

Chapter 1

Introduction

Organic electronics is expected to create unprecedented opportunities for new electronic devices that derive their functionality from the complex physical and electronic properties of single molecules [4–7]. Designed from the bottom-up, molecular materials have the potential to enhance the functionality of electronic devices in ways not possible with conventional Si technology. Individual molecules and self-assembled monolayers(SAMs) are able to perform the functions of conventional electronic circuits such as electrical switch [8–10], diodes [11–13], and transistors [14–17]. Additionally organic electronics may enable a variety of electronic functions such as chemical sensing [18,19] and thermoelectricity through molecular junctions [20]. The major advantages of organics, compared with inorganic semiconductors, is the low power consumption [21], flexibility [22], and lower cost [22]. Due to their structural flexibility, these electronic devices can be assembled on variety of surfaces, including flexible sheets and fabrics [22].

Organic molecules have been incorporated into devices such as organic light emitting diodes (OLEDs) [23], organic photovoltaic cells (OPVs) [24], sensors and photodetectors [25]. Further progress in this field requires concerted efforts from experimental and theoretical physicists, synthetic chemists and physical chemists to synthesize organics by

design, and to build nanostructures from them that allow to make their unique properties observable and exploitable. In addition, new analytical techniques are required to characterize these electronic devices [26–28].

The properties that can be useful in the context of devices are: electron transport, magnetic and electric polarization. Therefore, it is necessary to study those properties in organic materials. Also, the devices that utilize these properties on the molecular level require that the molecules are in contact with metal electrodes, where interactions may not only determine the functionality of the molecular structures, but also their integrity. It is of critical importance to understand the structure-properties relationship of those organic materials with and without supporting substrate or electrode, to control the molecular orientation, interfacial binding, and interaction between the molecules and electrodes to achieve desired and consistent performance from these devices.

One signature property of practical use is the switchable magnetic moment. Magnetism at the molecular level is exhibited by two types of molecules: single molecule magnets (SMMs) [29] and spin-crossover (SCO) complexes [30]. The SMMs, such as the prototypical Mn_{12}, are of limited practical use because they exhibit magnetic behavior only at very low temperatures ($<$10K) [29]. By contrast, the SCO complexes show reversible spin state transition near the room temperature [31–33]. The magnetic moment in these complexes is localized at the central transition metal ion. It has been demonstrated that the SCO complexes, in powdered form, can be reversibly switched between high-spin and low-spin states, by external stimuli such as temperature [30], pressure [34], electric field [35] and light [36]. But this switching of the spin state is strongly dependent on the local environment of the metal ion, which is susceptible to substrate interactions, crystal packing or the presence of an extraneous matrix, and which can also be affected by long-range effects such as cooperativity between adjacent molecules.

Just like the molecules with switchable magnetic moment, molecules with electric po-

larization can be of practical use, especially molecular ferroelectrics (MFE) [37]. MFEs are a special class of organic materials that exhibit a bistable electric polarization that can be reversed by applying an external electric field. MFEs can be engineered with molecular precision and possess superior scalability. While several of the popular FEs, including polyvinylidene fluoride (VDF) based polymers and oligomers, the KH_2PO_4 (KDP) and the recently discovered diisopropylammonium bromide (DIPA-B) may have their limitations regarding scalability and designability, there is one group of MFE, the proton transfer systems, that deserves particular attention. Their ferroelectric properties emerge from the hydrogen bonding where the strong coupling between the proton and the π-electron system of the molecule is essential for the switchable molecular dipole moments. The polarization exhibited by these organics is within molecular plane, which provides interesting possibility of surface supported *two dimensional* ferroelectrics.

Organic electronics will further benefit from the development of new materials that function as electrical conductors and semi-conductors. An interesting possibility in this regard is offered by actively studied 2D materials such as graphene, hexagonal boron nitride (h-BN), and transition metal dichalcogenides [38, 39]. Graphene has very high electron mobility [40] but the transistors from graphene cannot be switched off completely due to its zero band gap. By contrast, the structurally related h-BN is isoelectronic to graphene but it is an insulator with a band gap of 5.5 eV. The dichalcogenides, such as MoS_2 exhibit small direct band gap (1-2 eV) but they are essentially not two-dimensional as they exist in three atomic layered structure, where a layer of transition metal atoms is sandwiched between layers of sulphur atoms [41].

The band gaps in graphene and h-BN lies on the opposite ends of the spectrum as graphene is a zero band gap semiconductor and h-BN is an insulator. It is reasonable to assume that a material consisting of B, C and N atoms in graphenic lattice can have intermediate band gap that might be of practical importance. Theoretical studies have shown

that the band gap in such a material can be tailored in the range of 0-2 eV, by changing the stoichiometry as well as the arrangement of B, C and N atoms. In this thesis, I will validate this prediction experimentally.

This thesis is aimed at contributing to a fundamental understanding of the basic properties of the three types of organics discussed above. The research is focused on surface supported networks of three organic molecules (i) a proton transfer type ferroelectric, (ii) a Fe(II) spin-crossover complex, and (iii) a precursor molecule for synthesis of 2D graphene-like semiconductor. The motivation for this thesis research was the challenge to build nanostructures from functional organic molecules, to explore their structural arrangement through surface-supported growth that does not exist in the bulk, and to evaluate their properties that arise from nanostructuring and surface interaction. The main idea that was explored in this thesis research: can new organic materials be constructed molecule by molecule, that exhibit useful electronic or magnetic properties?

This research has produced a number of breakthrough discoveries and advances. Among them are:

- various 1D, 2D and 3D nanostructures of H-bonded 3-HPLN, wherein the molecular motif - coupling between H-bonds and π - electron system, is still preserved so that 1D and 2D - ferroelectricis appear to be a possibility
- substrate induced spin-state locking in the spin crossover complexes
- the discovery of a new 2D graphene-like sheet of B, C and N atoms with a predicted band gap of 1 eV
- band-gap engineering in m-carborane derivatives through electron bombardment induced crosslinking

Chapter 2

Experimental techniques

This chapter provides an overview of experimental techniques and instrumentation used for my doctoral research. The study of organics on surfaces requires defect free and atomically flat substrates, and the deposition of films of sub-monolayer to few monolayers molecular thickness. The synthesis and characterization of these samples must be done in ultra-high vacuum (UHV) chambers to avoid contamination. As a part of my doctoral research, I installed a multi-chamber surface science facility. This facility combines state-of-the-art comprehensive suite of sample preparation, microscopy and spectroscopic techniques to obtain atomic and electronic structure and properties of molecular thin films, metal thin films and metallic oxides. Figure 2.1 shows a schematic of the facility and its main components are described below:

1. **Preparation chamber :** The preparation chamber, with a base pressure of 10^{-10} mbar, is used for cleaning substrates and thin film synthesis. It combines the items described in 2-8.

2. **Molecular evaporator :** Home built Knudsen-like molecular evaporator for deposition of organic molecules on substrates. The evaporator has four quartz crucibles that

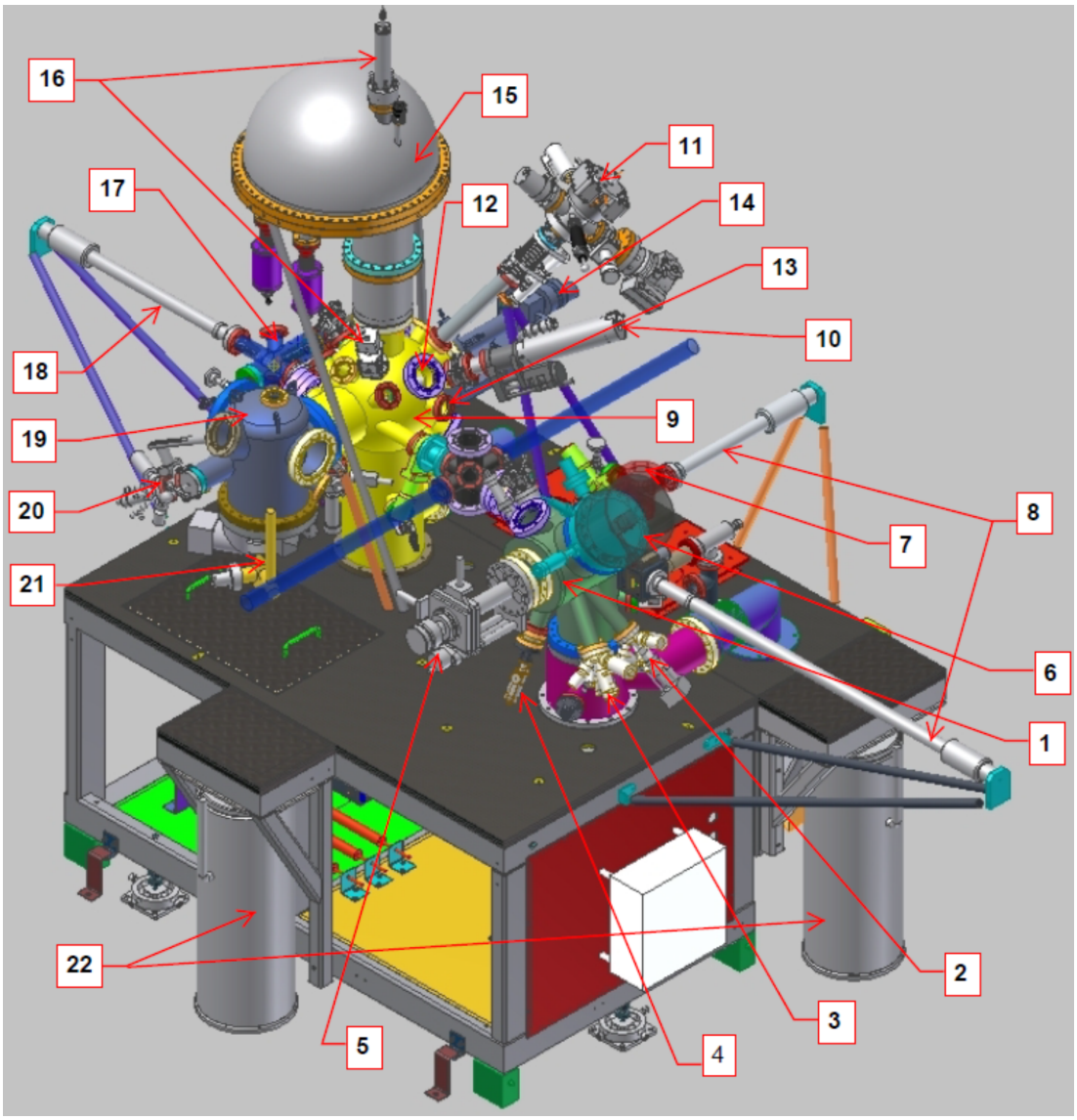

Figure 2.1: Schematic view of the surface science facility.

can be loaded with different molecular powders. Each crucible is equipped with its own thermocouple for temperature monitoring and filament for heating the crucibles. The molecular evaporator is water cooled to keep other crucibles cold when one or more crucible is heated.

3. **EFM3 metal evaporator :** Two commercially available (Omicron) metal evapora-

tors are installed on the preparation chamber for synthesis of metal thin films on substrates. The evaporation of the desired metal is achieved by electron bombardment of the evaporant that can be in the form of a rod or metal chunks inside a crucible. The evaporator is designed for precise sub-monolayer to multi-layer deposition of variety of evaporants. An integrated flux monitor once calibrated can be used for high-precision metal thin films deposition.

4. **Sputter gun** : The NGI3000 sputter gun is used to obtain atomically clean substrates. The substrate surface held at 0 V, is bombarded with Ar+ ions with energy upto 5 kV and sample currents upto 10 μA can be achieved.

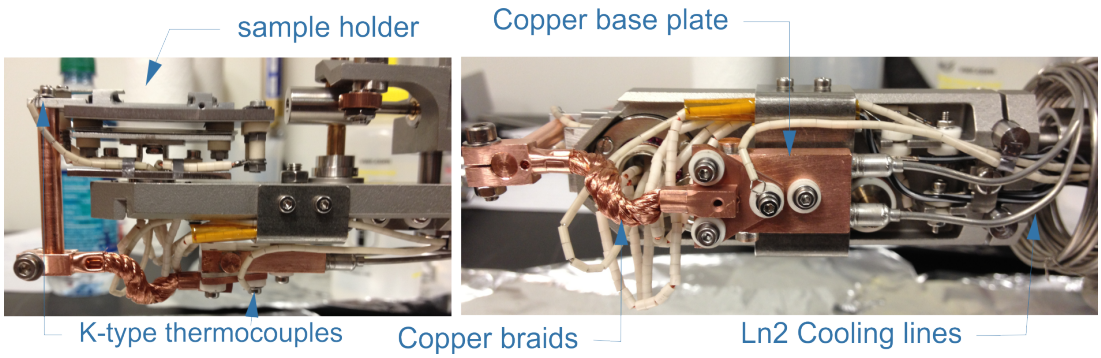

Figure 2.2: Side view (left) and bottom-up view of the manipulator.

5. **Manipulator :** The sample holder with x, y, z motion and 360° rotation of the sample is shown in figure 2.2. The conducting samples can be heated with e-beam bombardment at -650 V from the filament located beneath. Additionally, semiconducting samples can be heated by direct current heating. Also, the samples can be cooled to 100 K using LN_2 cooling. The copper base plate is cooled by passing pressurized cold nitrogen gas through the cooling lines. The copper braids connected between the copper base plate and sample holder then cools the sample. Simultaneous LN_2 cooling and e-beam heating is required for sample temperatures above 1000 K to

avoid melting the copper base plate. The sample temperature is monitored by two K-type thermocouples: one is located near the sample holder and second is located at the cooling base plate.

6. **Omicron SPECTALEED 590 :** A low energy electron diffraction (LEED) unit is installed in the preparation chamber. LEED allows for the structural characterization of substrates and thin films. The analysis of diffraction pattern for crystalline surfaces gives information about the symmetry of the surface structures [42, 43]. In the presence of adsorbates, such as organic molecules, the analysis of LEED pattern may reveal information about the size and rotational alignment of the adsorbate unit cell with respect to the substrate unit cell [44, 45].

7. **Load lock :** Fast-entry load lock (FEL) for sample, tip loading and removal from the UHV chamber.

8. **Magprobe :** Magnetic transfer arms for sample transfer between the preparation chamber, the analysis chamber and the FEL.

9. **Analysis Chamber :** The analysis chamber, with a base pressure of 10^{-11} mbar, is equipped with various spectroscopy techniques. It combines the items described in 10-18.

10. **X-ray source :** The DAR 400 is a twin electrode X-ray source for core level X-ray photoemission spectroscopy. The twin electrode configuration allows either Al K_α (1486.6 eV) or Mg K_α (1253.6 eV) radiation to be selected. Figure 2.3 shows the schematic of operating principle of the DAR 400. The electrons are extracted from the thoria coated tungstun filament and these electrons bombard the selected anode, which is held at high positive potential (13kV-15kV). The focus ring and shape of the nose cone ensures that the electrons hit the selected anode only. By switching the

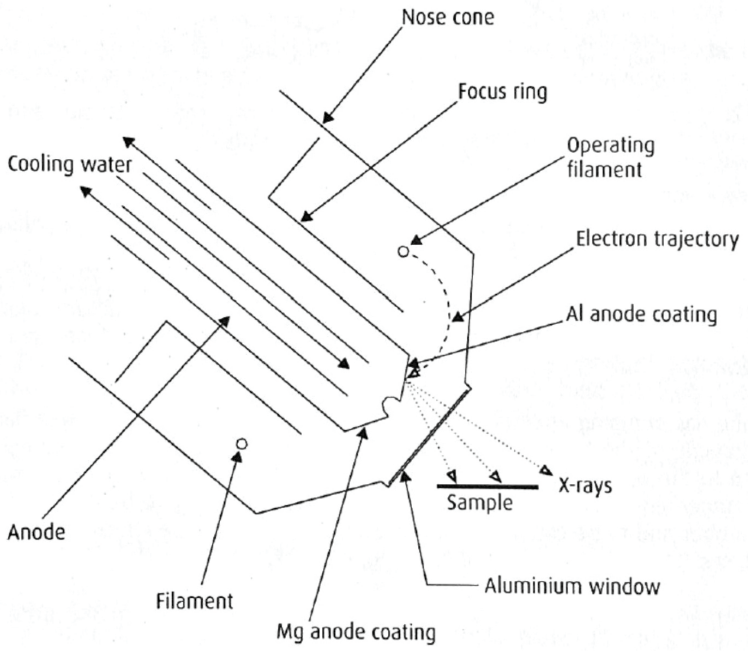

Figure 2.3: DAR 400 schematic reproduced from the user manual.

filament, Al or Mg anodes can be excited. The generated X-ray are passed through the aluminum window to the sample. The anode is water cooled to avoid heating the sample, anode surface and prevent the evaporation of Al or Mg coatings.

11. **Ultra violet source :** The UVS 10/35 is a differentially pumped light source for ultraviolet photoemission spectroscopy (Figure 2.4). The source can be used to study solid, liquid or gaseous samples by exciting distinct line spectra. The light source is designed to produce high intensity ultraviolet photon beam directed onto the sample by discharge and beam guide capillaries. It can be operated with a variety of noble gases (He, Ne, Ar, Kr, Xe) to produce photon beams of different energies. The photon energy ranges from 10 eV to 50 eV, with linewidth of few meV, and is useful for studying the occupied density of states of a sample. Figure 2.5 shows the schematic of the setup of UVS 10/35 photon source in the surface science facility. The quartz capillary is milled at two places to allow differential pumping via roughing pump (1st

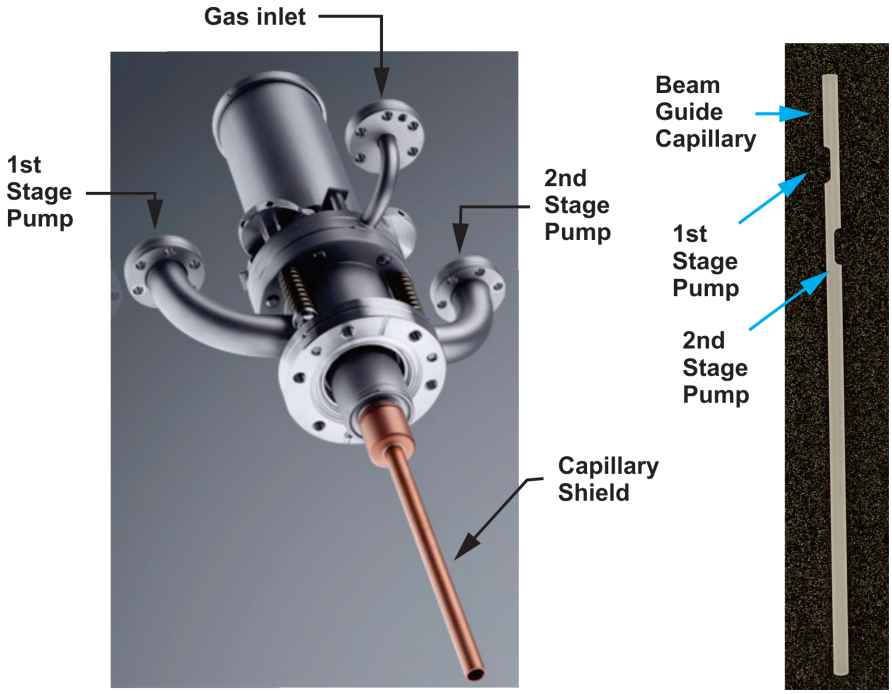

Figure 2.4: Specs UVS 10/35 photon source (left, reproduced from the user manual) and quartz beam guide capillary (right) is fitted inside the capillary shield.

stage) and turbo pump (2nd stage). The fist stage pump lowers the pressure inside the beam guide capillary to 10^{-3} mbar and the second stage turbo pump lowers the pressure to 10^{-5} mbar. A noble gas is injected through the leak valve connected to the photon source and arc discharge creates the radiation inside the capillary. The differential pumping pressure stages allow the radiation to be carried into the UHV chamber through the beam guide capillary.

12. **Electron gun :** The commercially available Kimball ELG-2 electron gun is used for electron stimulated studies such as inverse photoemission spectroscopy (IPES). The electron beam energy, beam current and spot size can be varied independently. The beam energy can be varied from 5 eV to 200 eV with a thermal energy spread of 0.3 eV. The e-beam spot size can be varied from 0.5 mm to 5mm and the beam current can be adjusted from 1 nA to 10 μA.

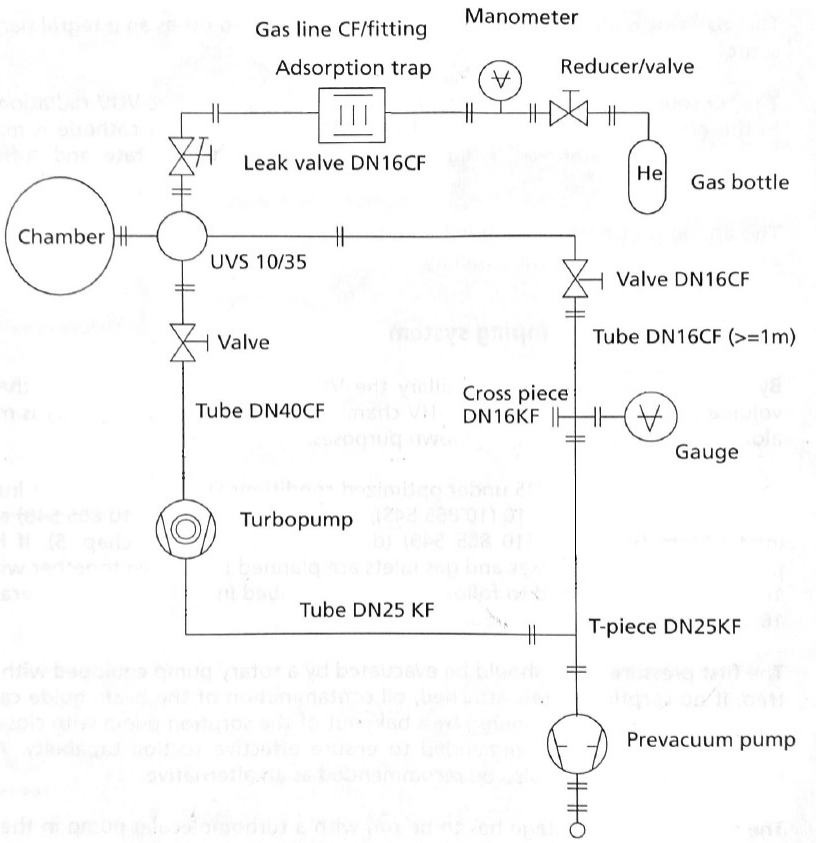

Figure 2.5: Schematic of differentially pumped UV lamp (reproduced from user manual).

13. **Photon detector :** Omnivac IPES 1000 photon detector for inverse photoemission spectroscopy. The sample is bombarded with electrons from the ELG-2 electron gun. These electrons are absorbed by the sample and the emitted photons are absorbed by the IPES 1000 detector. The photon flux is plotted as a function of incident electron energy to obtain the IPES spectra, which represents the unoccupied density of states for the specimen under investigation.

14. **Manipulator :** Sample stage (Figure 2.2) with manual x,y,z motion and motorized polar and azimuthal rotation of sample. The polar and azimuthal rotation of the sample allows the mapping of band structure in k-space.

15. **Phoibos 100/150 analyzer :** The high resolution spectrometer for measurement of energy of emitted electrons during the photoemission process, over a wide range (10 V - 3500 V). The sample electrons are excited using the UVS 10/35 light source or DAR 400 X-ray source. The electrons emitted from the sample are passed through the iris and 10 lens system inside the analyzer. The size of the electron beam entering the analyzer can be controlled by the iris, which can be set between 2.5-50 mm and the lens system focuses the electrons as they have wide angular distribution. The focused beam is passed through the entrance slit. This beam can then be further reduced by choosing one of the 8 entrance slits. A wide entrance slit increases the signal and reduces the energy resolution while a narrow slit increases the energy resolution and reduces the signal. After passing through the entrance slit beam is curved using the magnetic field and passed through the hemisphere. The inner and outer hemispheres are held at different voltage bias so that only electrons with a particular energy range will pass through. These electrons are passed through one of the three exit slits and hit the CCD detector.

16. **Sample alignment :** The alignment of the sample is necessary for good energy resolution in photoemission spectroscopy. A thin beam of light is shined through the viewport located at the top of the hemispherical analyzer and the light spot on the sample is seen on the camera. The sample position is adjusted until the spot is at the center of the sample.

17. **Load lock :** FEL chamber with three fold sample loading into the analysis chamber.

18. **Magprobe :** Magnetic transfer arms for sample/tip transfer between the FEL and the analysis chamber.

19. **Microscopy chamber :** Variable temperature scanning probe microscopy (VT-SPM)

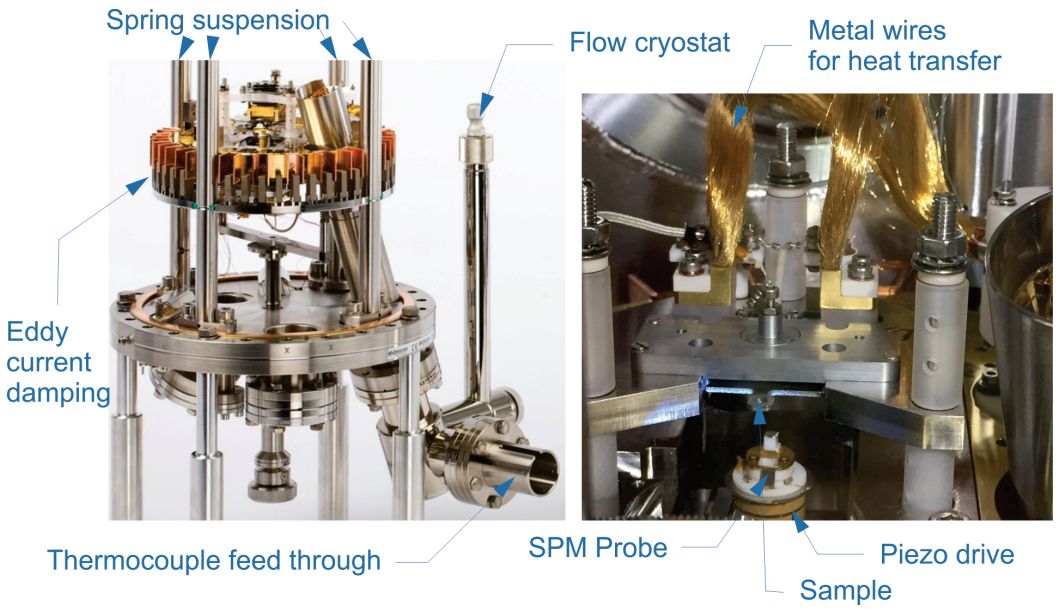

Figure 2.6: Variable temperature SPM (left). Close-up of the VT-SPM (right).

is capable of imaging wide variety of samples with 0.1 nm or better spatial resolution over wide range of temperatures. The SPM is shown in figure 2.6. The probe of the microscope can be changed to use it in various modes: metal tip for scanning tunneling microscopy (STM), cantilever tips for atomic force microscopy (contact and non-contact AFM) and conducting cantilever tips for piezoresponse force microscopy (PFM). These different modes can be used to study a variety of samples such as organic films, metal thin films, metal oxides and semiconducting films. The sample temperature can be precisely controlled using a flow cryostat with built-in heater. With the simultaneous use of liquid He cooling and built-in heater, stable sample temperatures between 60 K and 500 K can be achieved. The variable temperature SPM requires stable sample temperatures to reduce the thermal drift between the sample and the scanning probe. This is achieved by using thin metallic braid for heat flow between sample and cryostat. The fluctuations in the cryostat temperature due to liquid flow or heater are not propagated quickly to the sample. The

braid is flexible so that the vibrations from the cryostat do not propagate to the sample. Also, for high resolution imaging, the SPM is vibrationally decoupled from the UHV chamber using eddy current damping and spring suspension.

20. **Metal Evaporator :** One EFM3 evaporator is installed such that film deposition can be done with the sample in the SPM position.

21. **Flow Cryostat :** A Cryovac KONTI-cryostat is installed in the SPM chamber. The gas flow type cryostat with Helium can provide operating temperature range from 3.5 K to 500K.

22. **Vibration Damping :** The Newport S-2000 vibration control system is installed to isolate the system from the floor vibrations. The pneumatic system lifts the system above the floor and the noise can be reduced during the SPM operation for achieving atomic resolution.

In the next sections, I will describe the surface science techniques that are implemented in this system.

2.1 Scanning tunneling microscopy

The first scanning tunneling microscope (STM) was built by Binning and Rohrer in 1981 at IBM [46, 47]. Figure 2.7 illustrates the STM set up for imaging. A STM probe or tip, typically tungsten or platinum-iridium alloy, is mounted on a piezoelectric tube, which is connected with three transducers: x piezo, y piezo and z piezo [48, 49]. The piezoelectric tube can expand or contract when external voltage is applied to it, thus providing means of moving the STM probe in x, y and z directions. A voltage is applied in the x and y direction to scan over a pre-defined area and tip position over the sample is controlled

using the feedback amplifier. The piezoelectric effect allows high-precision control of the tip and the specimen surfaces can be imaged at atomic level with 0.1 nm or better lateral resolution and 0.01nm depth resolution [50]. The tip is positioned at sub-nm distance above the sample surface. At this distance, the electron wavefunctions in the tip overlap with the electron wavefunctions of the sample such that a finite tunnel conductance is established. When a bias voltage is applied between the sample and tip, a tunneling current is generated.

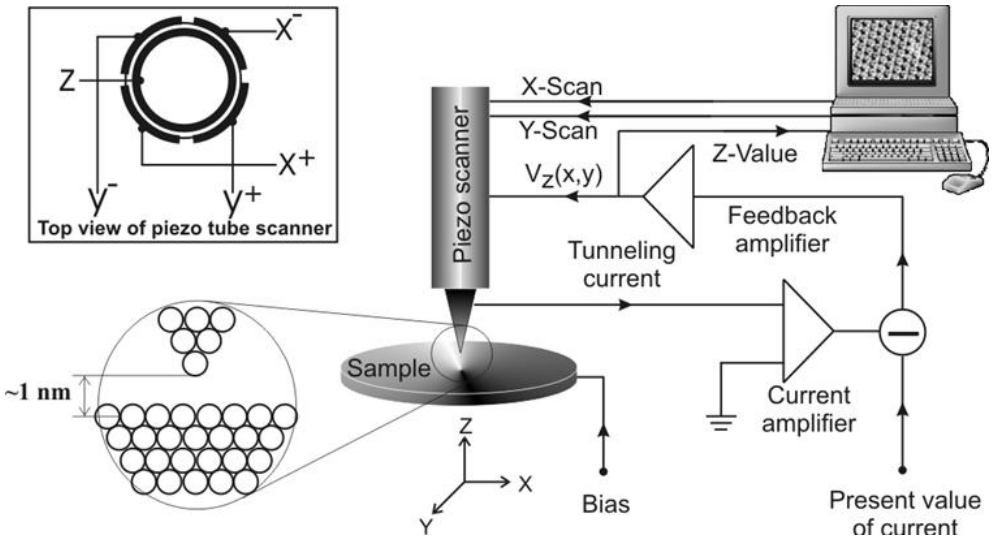

Figure 2.7: The Scanning Tunneling Microscopy schematic (source: *http://home.iitk.ac.in/gopan*).

The STM can be operated in two modes: constant current and constant height. In the constant current mode, the feedback signal from the amplifier is used to adjust the sample and tip distance to maintain a constant tunneling current as the tip is moved across the sample surface. The path of the STM tip i.e., z(x,y) is used to obtain the surface topography image. In the constant height mode, the tip-sample distance is kept constant and the changes in tunneling current are recorded as the tip scans over the sample. The variation of the tunnel current across the scan area is reproduced as the STM image.

The STM is best suited to image metal surfaces as the tunnel conductance is highest for metal-vacuum-metal junction. However, it can also be operated to investigate less conductive samples, such as thin oxide films [51–54] and organic molecules [55–59]. Organics have a large HOMO-LUMO gap, and the oxides have very large band gap. Hence, the STM on those materials requires thinnest film samples and high tunnel voltages. Figure 2.8 shows three types of samples imaged with VT-STM during the setup of the instrument. The atomic resolution on reconstructed Si surface shows the atoms and defects in the surface (Figure 2.8(a)), where each bright lobe represents one Si atom. The atomic resolution on thick oxide film ($SrRuO_3$) was difficult but the surface morphology at nm scale is easily possible (Figure 2.8(b)). Also, molecular resolution allows to identify individual pentacene molecules on Au(111), where each bright lobe represents one pentacene molecule and the herringbone reconstruction of Au(111) is visible under the molecules (Figure 2.8(c)).

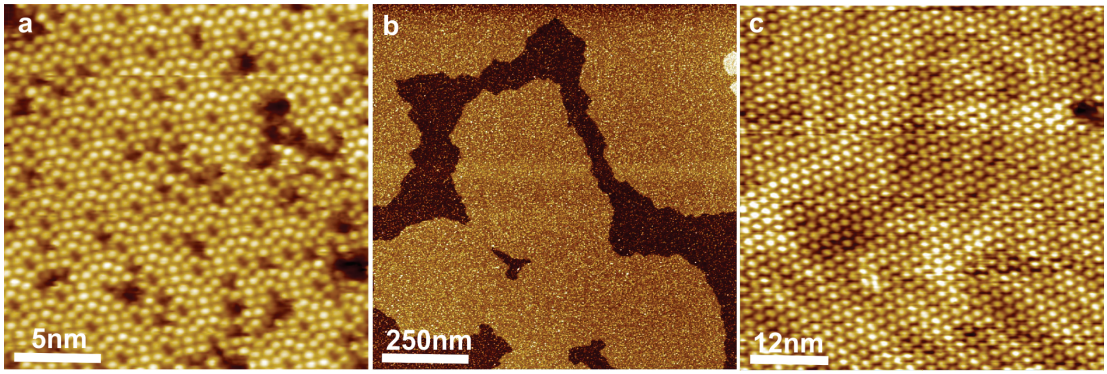

Figure 2.8: Examples of various types of samples imaged with VT-STM during instrument setup. All the images were taken at room temperature (a) atomically resolved Si reconstructed surface (b) strontium ruthenium oxide (c) nitrogen derivative of pentacene molecules on Au(111) surface.

The tunneling mechanism that is the basis of STM measurements has originated from quantum physics, which deals with the dynamics of objects at microscopic level. In a typical STM measurement the tip and sample are separated by small vacuum gap (0.4-0.7 nm). The alignment of the relevant electronic levels of this sample-vacuum-tip junction can

be represented by figure 2.9(a). According to classical mechanics that treats electrons as particles, the vacuum acts as a potential barrier for electrons such that the electrons cannot go from sample to the tip and vice versa, unless the total energy of the electrons is higher than the height of the potential barrier. However, this description of electrons does not consider their wave-like nature. Quantum mechanically, electrons have a finite probability to overcome the vacuum potential barrier even if their energy is lower than the height of the potential barrier. This phenomenon is called tunneling effect and can be explained by solving the Schrodinger equation for electrons as explained below:

$$\frac{-\hbar^2}{2m}\frac{\partial^2\psi_n(z)}{\partial^2 z} + U(z)\psi_n(z) = E_n\psi_n(z) \tag{2.1}$$

where $\psi_n(z)$ are the electron eigen wavefunctions, E_n is the energy corresponding to eigenfunctions, and U(z) is the potential energy of electrons. Inside the sample and tip, the total energy of an electron is larger than potential energy so that the electron wavefunction is a traveling wave solution:

$$\psi_n(z) = \psi_n(0)e^{\pm ikz} \tag{2.2}$$

where $k = \frac{\sqrt{2m(E-U(z)}}{\hbar}$

Inside the barrier, the total energy of electrons is less than U(z), the electron wavefunction is thus a decaying wave solution:

$$\psi_n(z) = \psi_n(0)e^{-ikz} \tag{2.3}$$

where $k = \frac{\sqrt{2m(U-E)}}{\hbar}$

The probability of finding an electron at any location in the vacuum barrier, shown in figure 2.9, is given by wave function squared. If the gap between the tip and sample is

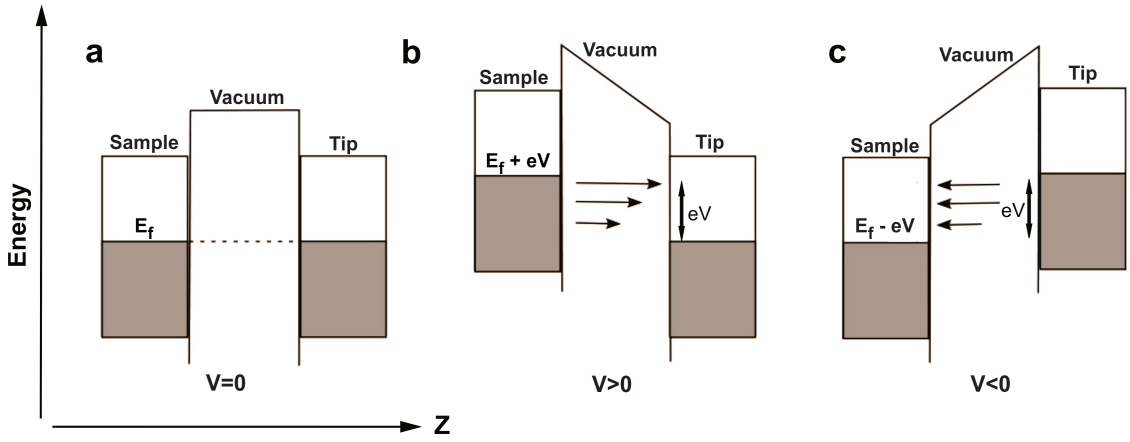

Figure 2.9: Sample-vacuum-tip junction for a STM. Gray area represent filled energy states and white area represents empty energy states (a) at zero bias voltage Fermi energy levels of the sample and the tip are aligned (b) at positive bias voltage V, the Fermi energy of the sample is increased by eV (c) at negative bias voltage V, the Fermi energy of the sample is lowered by eV.

small, it is possible that the electron wavefunction in tip and the sample extend into the barrier and overlap such that there is a finite probability for an electron to exist within the barrier:

$$P \propto |\psi_n(z)|^2 e^{-2kz} \tag{2.4}$$

Under the applied external bias voltage or the electric field, the electrons in barrier region can move between the tip and the sample. When a small positive bias V is applied to the tip and sample junction, the Fermi levels of tip and sample are offset by eV as shown in figure 2.9 (b). Electrons with in E_f and $E_f \pm$ eV energy range contribute to tunnel current. Therefore, the local density of states of sample and tip near the Fermi level determine the tunneling current. Lateral variations in density of states across the sample surface are observable with the STM images. The density of states of the tip also determine the tunneling current. Depending on the sign of the bias voltage, the electrons tunnel from the occupied states of the tip into unoccupied states of the sample or from occupied states of sample into the unoccupied states of tip, as shown in figure 2.8(b)-(c).

An approximation of the tunnel current was derived by John Bardeen for a metal-insulator-metal junction [60]. It was shown that:

$$I \propto |M|^2 \int_{-\infty}^{+\infty} [f(E_f - eV + \varepsilon) - f(E_f + \varepsilon)\rho_S(E_f - eV + \varepsilon)\rho_T(E_f + \varepsilon)\, d\varepsilon \tag{2.5}$$

where M is the transfer matrix element, ρ_S and ρ_T are the density of electronic states in the sample and tip respectively. Analysis of STM image would require the knowledge of M, ρ_S and ρ_T. This expression for the tunnel current can be simplified with some approximations as described in the Tersoff and Hamann model [61, 62]. Those approximation from the model are summarized below:

1. The tunneling matrix element M is independent of the energy level.
2. The tip is spherically symmetric.
3. The tip density of states are constant and featureless.
4. The sample density of states are smooth function of energy.

Based on these approximations, the tunnel current can be expressed as

$$I \propto \rho_T |\Psi(r_0)|^2 \int_0^{eV} \rho_S(E_F + \varepsilon)\, d\varepsilon \tag{2.6}$$

where ρ_S, ρ_T are the density of states of sample and tip, respectively. $\psi(r_0)$ is the sample wavefunction at the center of curvature of the tip, E_F is the Fermi energy. By differentiating each side, it is shown that the differential conductance at the tunneling voltage is proportional to the sample local density of states (LDOS), ρ_s,

$$\left.\frac{dI}{dU}\right|_{U=V} \propto \rho_s(E_F + eV, r_0) \tag{2.7}$$

This can be of huge practical importance, as it opens up a direct way to measure the LDOS of thin films and nanostructures with STM directly, as discussed below.

The direct consequence of equation 2.7 is that the STM capabilities can be expanded beyond the sample imaging. The STM can be used in spectrocopy mode, called scanning tunneling spectroscopy (STS). The STS can be used to study the local density of states [63–66], vibrational states [67–69], measure band gap [70, 71], and measure molecular conductivity [72]. The origin of STS was found in the early work of Gerd Binnig and Heinrich Rohrer where they observed change in the appearance of Si atoms depending on the applied voltage bias [73].

To measure the LDOS experimentally, the STM tip is moved to the point of interest on the sample surface with chosen values of bias voltage and tunnel current, which determine the tip-sample distance z. The tunneling voltage is ramped while the feedback loop is opened, i. e. z stays constant, and the current is recorded to obtain I(V) curves. To obtain the dI/dV curves from I(V) data, a lock-in technique is used. A detailed description can be found in the thesis [74]. In the lock-in technique, the tunneling voltage is modulated with a small sinusoidal voltage $V_m = sin(\omega_m t)$. The modulation frequency, $f_m = \omega_m/2\pi$, is thereby set to much higher values (1-7 kHz) as the regulation speed of the feedback loop that holds the tunneling current constant in closed-loop mode, thus it is guaranteed that the modulation does not influence the recording of constant-current images. The derivative of the signal is proportional to the LDOS.

As for example, I have used the STS to determine the band gap of m-9-carboranethiol molecules on Au(111), see chapter 5. Figure 2.10 shows the dI/dV spectra as a function of voltage for m-9-carboranethiol on Au(111). As can be noted from the spectra, the conductivity is low in an energy window of $E_F \pm 1.5$ V, where E_F is located at 0 V. This region corresponds to electronic band gap, which is directly observable. At bias voltages larger than the band gap, the conductivity of electron involves the energy states of the molecule,

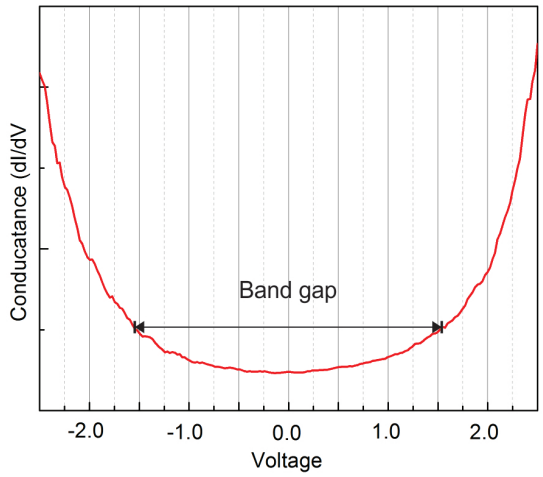

Figure 2.10: dI/dV spectra as a function of bias voltage for m-9-carboranethiol molecules deposited on Au(111).

which results in a drastic increase of local conductivity. The molecule has band gap of (HOMO-LUMO gap) approximately 3 eV, which suggests that it is an insulator and the shape of this curve represents the LDOS for this as a function of energy above and below the Fermi level.

Since the tunneling current in a scanning tunneling microscope only flows in a region with diameter $\leqslant$ 0.5 nm, STS is unusual in comparison with other surface spectroscopy techniques, which average over a larger surface region. Therefore, the STS provides the possibility for probing the LDOS of metals, semiconductors, and thin insulators on a scale unobtainable with other spectroscopic methods.

2.2 Atomic force microscopy

Atomic force microscopy (AFM) is another type of scanning probe microscopy with spatial resolution of the order of nanometers or better. It was the next microscopy technique de-

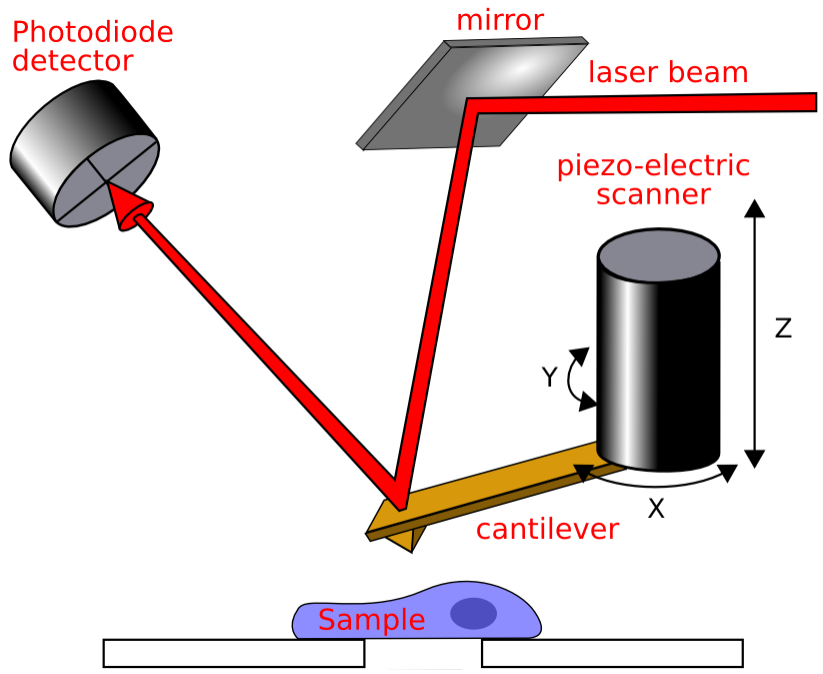

Figure 2.11: Schematic of an atomic force microscope (source: http://www.freesbi.ch/).

veloped after STM by scientists working at IBM [75]. While STM uses a tunnel current to image sample surface, the AFM uses the force of interaction between the sample and probe for imaging. Figure 2.11 shows the schematic for an AFM. The AFM probe is mounted on a piezoelectric scanner, much in analogy to STM. The AFM probe consists of a cantilever with a sharp tip at its end that is used to scan the sample surface. When the AFM probe is brought closer (with in nm distance) to a sample surface, forces between the tip and the sample lead to a deflection of the cantilever. Depending on the type of sample and tip, forces between them can be mechanical contact force, electrostatic force [76, 77] , van der Waals forces, capillary forces [78, 79], chemical bonding [80] , or magnetic forces [81, 82]. Typically an optical method is used to measure the deflection of the AFM probe. Here, a laser light from a solid state diode is reflected from the back of the cantilever and collected by a position-sensitive detector (PSD). This PSD is effectively a split photodiode, which outputs a signal proportional to the deflection of the cantilever. The PSD signal is evalu-

ated as function of the tip position data to produce topography images of the sample. As an example, figure 2.12 shows the AFM topography and force map for bismuth ferrite imaged using VT-AFM during the facility setup.

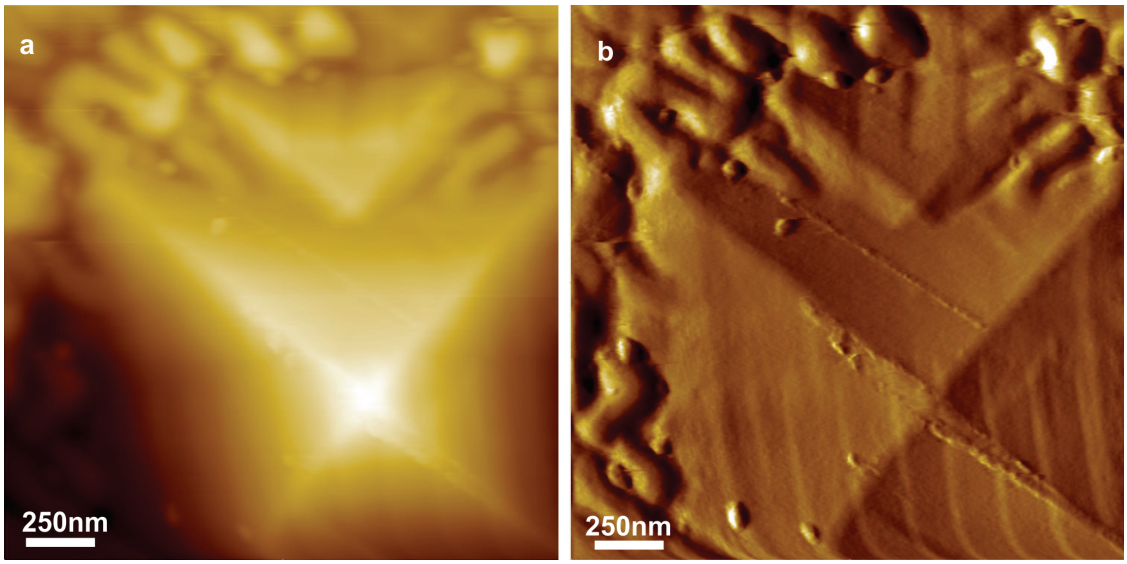

Figure 2.12: AFM contact mode images of bismuth ferrite taken during the testing of VT-SPM (a) topography of the BFO film (b) interaction force map between the tip and sample.

The AFM can be operated in a number of modes, depending on the application. In general, possible imaging modes are divided into static, also called contact mode and a variety of dynamic, non-contact or ”tapping” modes where the cantilever is vibrated or oscillated at a given frequency. In a contact mode, the tip is dragged across the sample surface and the deflection of the tip is recorded due to the change in the interaction force between the probe and the tip. However, in the contact mode the tip is prone to damage, which limits the life of the tip. Also, the adsorbates on the surface can stick to the tip, which in turn affects the resolution of the AFM. Contact mode measurements are necessary, for instance, in PFM mode. In non-contact mode [83], the cantilever does not touch the sample surface but it is instead oscillated above the surface at its resonant frequency. Interaction force between the tip and the sample changes, usually decrease, the resonance frequency of the tip. The

change in this resonance frequency is used to measure the tip-sample distance and software uses that information to convert it into topography of the surface. The AFM tip and sample are less prone to degradation effects as compared to contact mode measurements. Non-contact mode is the preferred mode for fragile samples such as organic thin films.

As mentioned earlier, AFM can measure different forces of interaction. This can be achieved by modifying the AFM tip. One such method have been described in the next section to investigate oxide ferroelectric films.

2.3 Piezoresponse force microscopy

Piezoresponse force microscopy (PFM) is a mode of atomic force microscopy (AFM) that allows imaging and manipulation of oxide piezoelectric materials [84–87]. The PFM exploits the piezoelectric effect, where application of external voltage expands or contracts the ferroelectric material. This is achieved by applying modulation alternating bias voltage to the sample and the resulting deformation of the sample is detected through the AFM photodiode detector. The signal is then demodulated using the lock-in amplifier to obtain the amplitude and direction of polarization of ferroelectric domains. The PFM was first implemented by Guthner and Dransfeld [88]. Since, it has become a widely used tool to investigate ferroelectrics. The PFM is ideal for identification of domains from relatively large scale, 100 x 100 μm^2 scans to the nanoscale along with the simultaneous imaging of sample surface topography. Also, it can be used to write polarization pattern and switch polarization domains by applying external bias voltage.

Figure 2.13 shows the polarization patterning done on a 48-unit cell BTO film using the VT-PFM at room temperature. The larger 1000 nm x 1000 nm square was polarized by applying 4 V bias voltage between the sample and the tip and scanning the tip over this area such that it creates a domain with the polarization out of the plane. The smaller

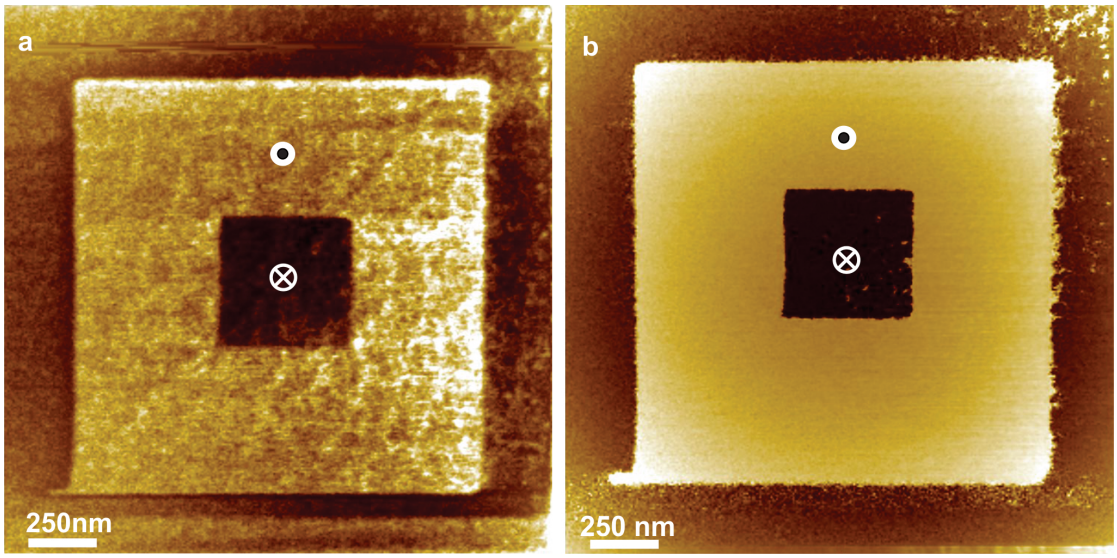

Figure 2.13: PFM image of polarized 48 unit cell $BaTiO_3$ taken from VT-SPM (a) amplitude PFM signal (b) hase PFM signal.

500 nm x 500 nm was polarized by applying -4 V bias voltage and scanning the tip over the smaller area. The image was obtained by using small modulation voltage and reading the corresponding piezoelectric response. The measurement technique can be described by the illustration shown in figure 2.14. The blue line shows the modulation voltage applied to the tip and red line shows the piezoelectric response. When the applied electric field is aligned with the direction of polarization, the positive half of the modulation voltage results in an expansion of the domain, giving a positive deflection. A negative half cycle contracts the domain giving a negative deflection. In such a case, the piezoresponse is always in-phase with the driving voltage as shown in figure 2.14(b). The corresponding area in PFM looks bright in phase map. When the applied bias voltage is opposite to the direction of the polarization the piezoresponse is out of phase by 180° with respect to the modulation voltage as shown in figure 2.14(d). Those areas in PFM look dark in the phase map. This results in the contrast with the domains pointing in opposite directions.

All the microscopy methods described above are techniques for investigating properties

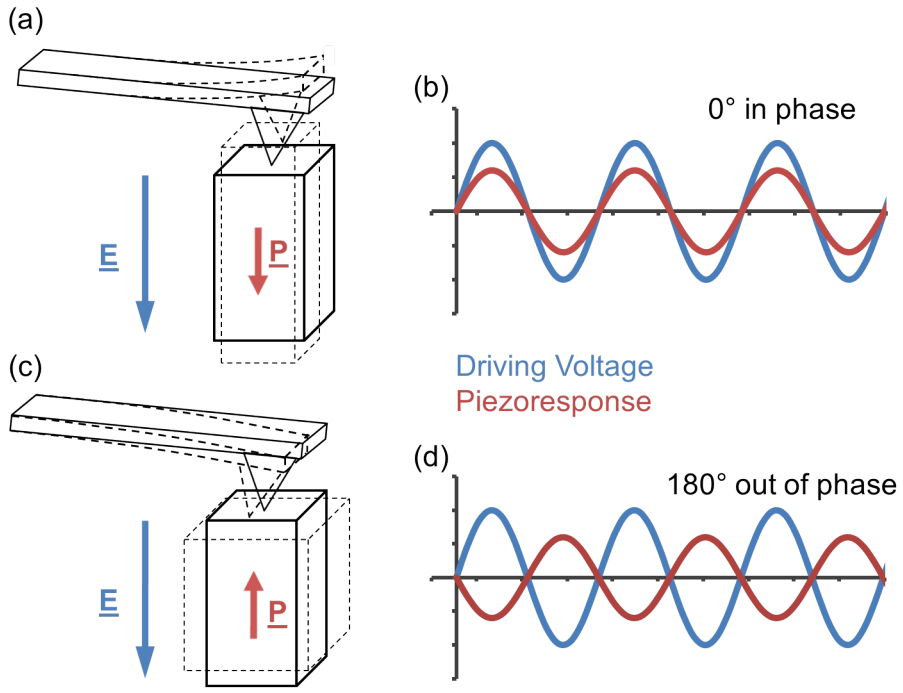

Figure 2.14: Illustration of PFM measurement (source: www.wikipedia.org).

of the materials locally due to their resolution of nanometer or better. These techniques are complimented by spectroscopy techniques described in the next sections. The surface sensitivity of theses techniques can be explained using the graph shown in figure 2.15. The techniques I used for my research include low energy electron diffraction (LEED) with electron energy range 20-200 eV, X-ray photoemission energy (XPS) with electron energy range 0-1500 eV, ultraviolet photoemission energy (UPS) with electron energy range 10-50 eV and inverse photoemission energy (IPES) with electron energy range 5-20 eV. Based on the energy of electrons involved, it is seen from figure 2.15 that electron mean free path in LEED, UPS and IPES is less than 1nm, which means these techniques are highly surface sensitive and probe only topmost layers. However, the energy range of electrons in the XPS is very large, upto 1500 eV, and it can obtain signal from thicker surface region.

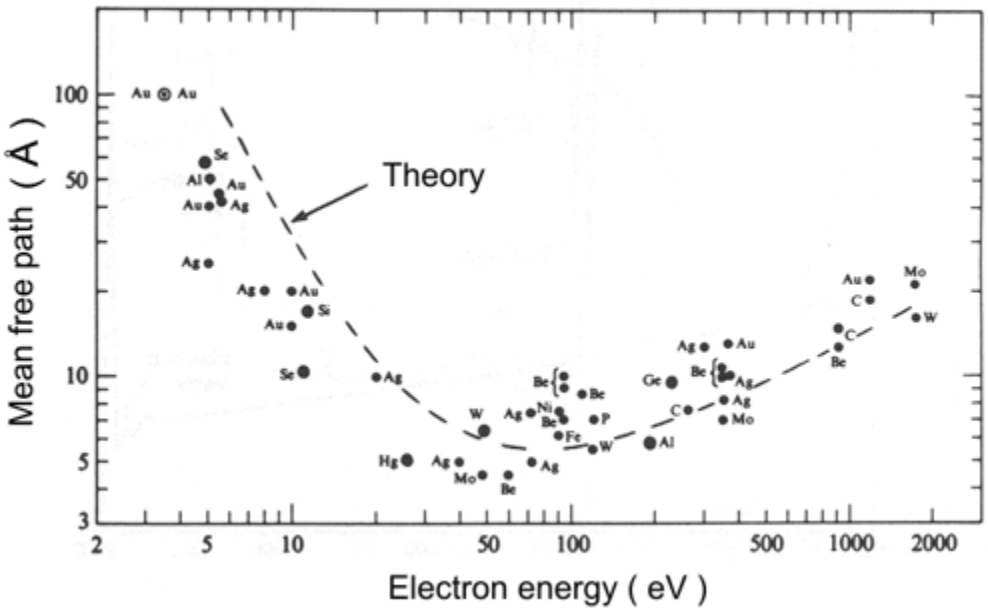

Figure 2.15: Electron mean free path as a function of energy. Reproduced from [89].

2.4 Low-energy elctron diffraction

Low-energy electron diffraction (LEED) is an experimental technique used for the determination of surface structure of crystalline materials [42, 43]. The origin of this technique is based on the groundbreaking work of Loise de Broglie who introduced the concept of wave-particle duality, for which he was awarded the Nobel prize [90]. According to de Broglie, the wavelength of any particle with momentum p is given by:

$$\lambda = \frac{h}{p} \tag{2.8}$$

where h is Planck's constant. The de Broglie hypothesis was confirmed by diffraction experiment performed by Clinton Davisson and Lester Germer at Bell labs [91]. They observed that the back scattered electrons from the nickel target showed similarity to the diffraction patterns observed for X-ray diffraction performed by Laue and Bragg.

As the name suggests, the energy of incident electrons used in the diffraction experi-

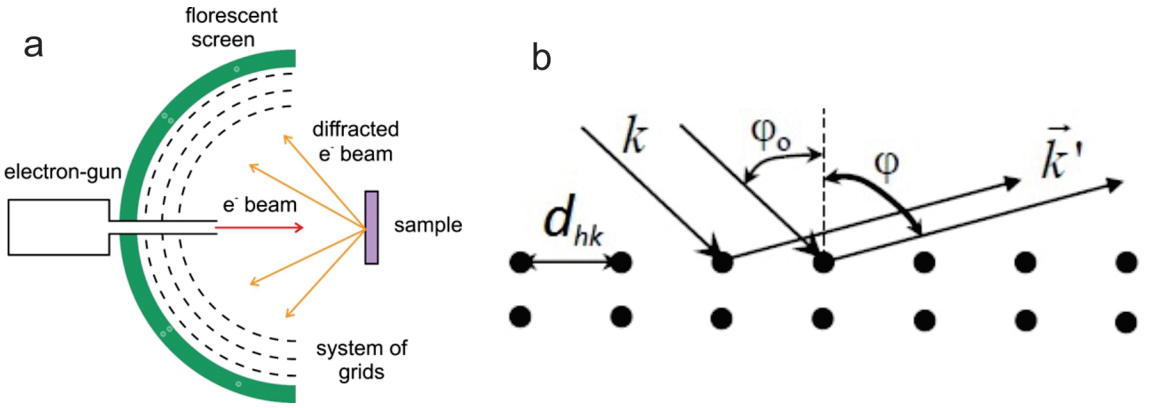

Figure 2.16: (a) Schematic for LEED instrument (b) Diffraction from a 2D crystal (source: https://www.uni-marburg.de/fb13/researchgroups/molecular-solid-state-physics/methods).

ments lies below 200 eV. At these energy values, the wavelength of the incident electrons is of the order of atomic separation in most single crystals, which is an important consideration for the observation of diffraction pattern. Figure 2.16 shows schematic for a typical LEED instrument and diffraction of electrons from a two dimensional lattice. The diffraction maxima is observed when the condition of constructive interference is fulfilled, such that for 1D case,

$$a_i[\frac{2\pi}{\lambda}(sin\phi - sin\phi_0)] = 2\pi n \tag{2.9}$$

where a_i is the lattice vector. It can be rewritten in terms of incident and scattered wave vectors, such that

$$\vec{a_i}.\vec{k} - \vec{a_i}.\vec{k'} = 2\pi n \tag{2.10}$$

For a 2D surface, the equation 2.10 can be rewritten in terms of Miller indices (h,k) of the atomic planes, such that

$$\vec{a_1}.(\vec{k} - \vec{k'}) = 2\pi h \tag{2.11}$$

$$\vec{a_2}.(\vec{k} - \vec{k'}) = 2\pi k \tag{2.12}$$

where a_1 and a_2 are the unit cell vectors for 2D lattice. Adding equation 2.11 and 2.12, we

get

$$\vec{k} - \vec{k'} = 2\pi(\frac{h}{\vec{a}_1} + \frac{k}{\vec{a}_2}) \tag{2.13}$$

The above equation can be written in terms of reciprocal lattice vectors,

$$\vec{k} - \vec{k'} = 2\pi(h\vec{a_1}^* + k\vec{a_2}^*) = \vec{G_{hk}} \tag{2.14}$$

where G_{hk} is the reciprocal lattice vector for atomic plane with Miller indices (h,k). Therefore, the direction of the diffraction maxima is determined by the reciprocal lattice vector. Thus, the diffraction pattern observed on the LEED instrument screen is a direct representation of reciprocal lattice. Figure 2.17 shows the diffraction pattern from a 2D square lattice and corresponding Ewald sphere construction using the LEED screen as the surface of Ewald sphere. First incident vector, $\vec{K_0}$, is drawn to terminate at origin of reciprocal lattice. Next, an Ewald sphere of radius k_0 with center at start of vector, is drawn. Rods are drawn from reciprocal lattice positions perpendicular to surface to intersect the sphere surface. Next, a wave vector $\vec{K}$ is drawn from the center of the sphere to terminate at the point where Ewald sphere intersects a rod. For any rod that intersects the LEED screen, the diffraction equation can be written as

$$2d.sin\theta = \sqrt{h^2 + k^2}.\lambda \tag{2.15}$$

the angle, θ, can be determined from the geometry for any diffraction spot. For a known value of d and θ, the miller indices for diffraction spots can be identified.

All LEED surface diffraction patterns show a symmetry reflecting that of the surface structure. In the presence of an adsorbate the qualitative analysis may reveal information about the size and rotational alignment of the adsorbate unit cell with respect to the substrate unit cell. For example figure 2.18 shows the LEED pattern obtained for Ir(111)

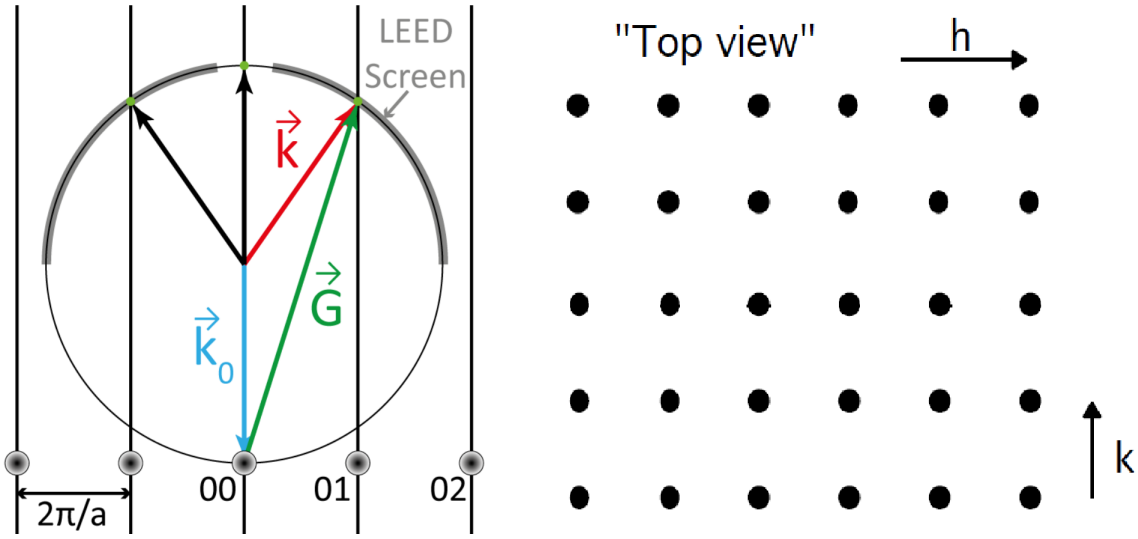

Figure 2.17: Ewald sphere construction for diffraction from 2D crystal (source: http://www.maths.tcd.ie/ bmurphy/figures/techniques/ewald.png).

surface (left) and 2D BCN sheet on Ir(111)(right). The Ir(111) surface has hexagonal symmetry, which is seen in LEED pattern with the presence of six diffraction spots. When a 2D BCN sheet is synthesized on top of Ir(111), the resulting diffraction pattern shows satellite diffraction spots surrounding the Ir(111) spots. This is the evidence of Moire superstructure due to lattice mismatch between the Ir(111) substrate and BCN sheet, explained in chapter 6.

2.5 Photoemission spectroscopy

Direct photoemission and inverse photoemission spectroscopy are surface science techniques to determine the occupied energy levels and unoccupied energy levels of a material, respectively. In direct photoemission spectroscopy (PES) or photoelectron spectroscopy, the electrons are removed from a material by the absorption of photons. The energy of the photoelectrons is measured to determine their binding energy in that material. The energy of incident photon can be varied by using different sources and electronic struc-

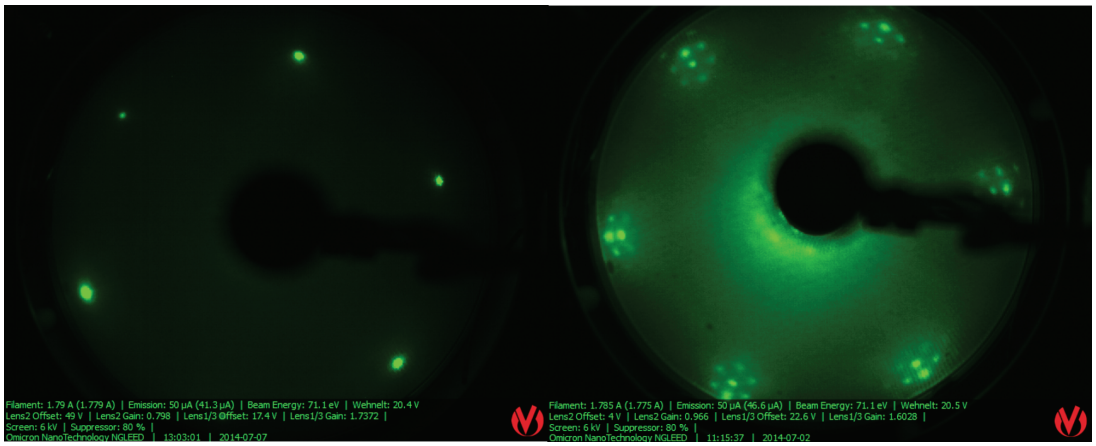

Figure 2.18: LEED pattern for Ir(111) (left) and BCN sheet on Ir(111) (right). The diffraction pattern shows six fold symmetry of Ir(111) surface and Moire superstructure formed due to lattice mismatch between Ir(111) and BCN sheet (explained in Chapter 6).

ture of a material can be probed with different energy range and resolution. Regardless of the energy of the photons, the general theme is to measure the binding energy of the ejected photoelectrons. This can be achieved by using the conservation of energy equation $E_B = h\nu - E_K - \phi$, where E_K is the kinetic energy of the ejected photoelectron, $h\nu$ is the energy of incident photon and ϕ is the work function of the material and detector. In comparison, the inverse photoemission spectroscopy (IPES) uses absorption of incident electrons by the empty electron energy levels to determine the unocccupied band structure of a material.

For a comparison Figure 2.19 shows the energy levels probed by 3 different spectroscopy techniques: XPS, UPS and IPES. The difference and sensitivity of the three techniques can be understood by the relation between electron energy and inelastic mean free path of the electrons as explained earlier with reference to figure 2.15. In our system, the XPS uses the DAR 400 as the photon source, which emits either Al Kα (1486.6 eV) or Mg Kα (1253.6 eV) radiation. Therefore, the maximum energy of electrons emitted during the XPS measurement is approximately 1486 eV. From figure 2.15, it can be seen that the

electron mean free path in such case is few nm. That means XPS can probe the top few nm layers of a specimen. Also, the X-ray photon energy is sufficiently high such that it can excite the electrons from the core levels of most elements (Figure 2.19(a)).

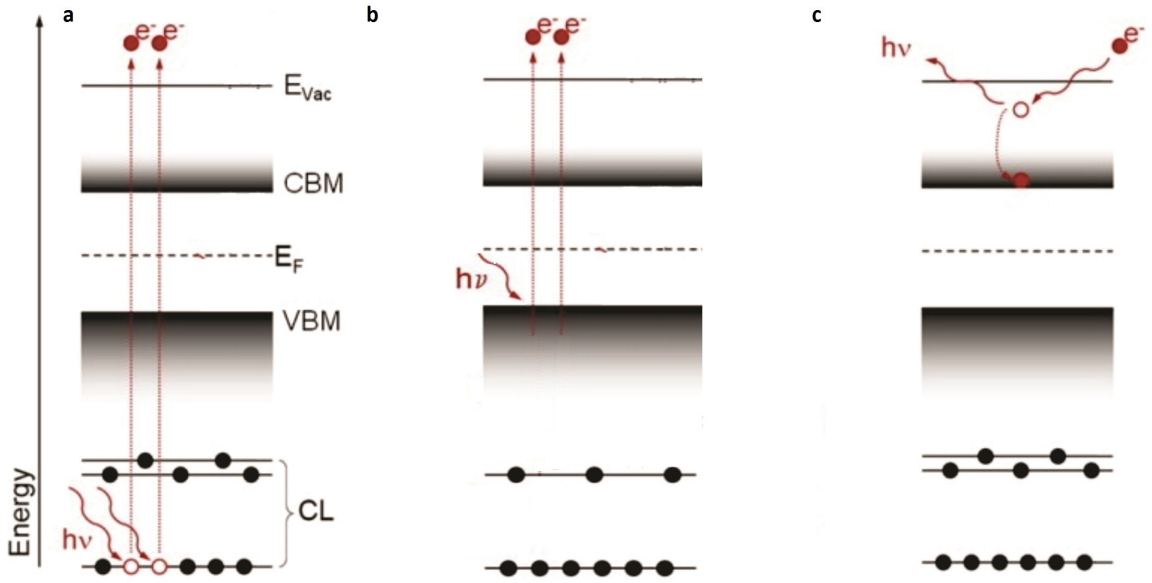

Figure 2.19: (a) Core-level XPS probes the atomic levels (b) UPS probes occupied energy levels few eV below the Fermi level (c) IPES probes unoccupied electronic states above the Fermi level.

Since the energy of emitted photoelectrons in UPS and incident electrons in IPES is less than 50 eV, the probing depth is limited to typically less than 5 monolayers of a specimen surface. The energy of the photons in UPS is so small that it can only excite the electrons immediately below the Fermi level (Figure 2.18(b)). Therefore, the UPS spectra is representative of the valence band of a specimen. The IPES uses electrons as a source that can only be absorbed by the unoccupied energy states that lie above the Fermi level. Therefore, the IPES spectra is representative of unoccupied electronic energy states of a specimen (Figure 2.18(c)).

2.5.1 X-ray photoemission spectroscopy (XPS)

The XPS technique was first developed by Kai Siegbahn and his group in 1957 for which he was awarded the Noble prize in 1981 [92]. They referred to this technique as electron spectroscopy for chemical analysis (ESCA). The energy of X-ray photons is enough to remove the core electrons, so it is also referred as core-level PES or photoelectron spectroscopy for inner shells (PESIS). XPS can be performed using custom, commercially built

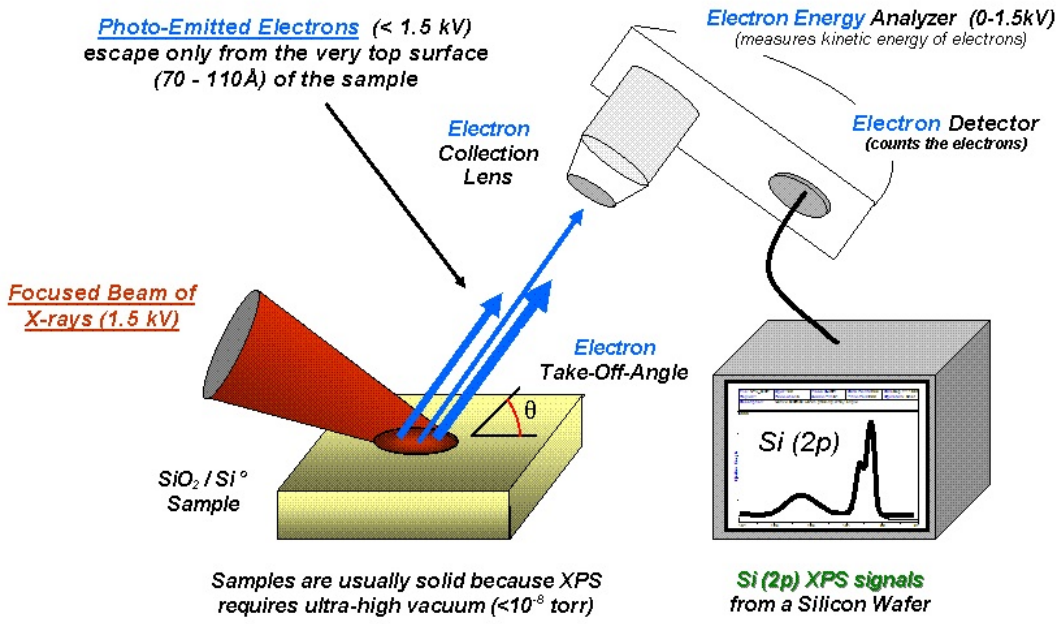

Figure 2.20: Schematic of commercial XPS system (source: www.wikipedia.org).

system or synchrotron-based light source. Our XPS instrument uses an Omicron Dar 400 X-ray source with photon beam of 10-30 mm beam diameter. The energy of emitted photoelectrons is determined by Phoibos 100/150 energy analyser. Figure 2.20 shows schematic of a commercial photoemission spectroscopy (PES) setup. It includes a photon source, electron energy analyser, electron detector, electron optics, sample manipulator with x/y/z motion and θ, ϕ rotation. Due to the size limitations of the vacuum chambers, the detec-

tor is almost one meter away from the sample under study. In order for electrons to travel this distance without any energy loss, these instruments have to be installed in an ultra-high vacuum chamber with 10^{-9} mbar or lower pressure. An XPS spectrum consists of intensity (number of photoelectrons) versus the binding energy or kinetic energy of photoelectrons. The electron analyser detects the kinetic energy of the ejected photoelectrons. If the ϕ is known, a measurement of the kinetic energy can be used to map out the binding energies of all core level electrons using conservation of enery, $E_B = h\nu - E_K - \phi$. The binding energy values for core electrons have distinctive values for each element, which can be used to identify each element present in the sample under study. Also, the intensity of these peaks is related to the amount of the element present in the sample. The intensity data can be analyzed to obtain the percentage of a particular element present in the sample. The XPS instruments can detect to typically less than 3% surface concentration of elements. Even smaller percentages require very long time for data acquisition but it is possible to determine elements present in parts per million (ppm), as will be explained later in this section with an example.

As an example, figure 2.21 shows the XPS spectrum taken for the Au(111) single crystal mounted on a Tantalum sample plate. Since every element has different number of electrons and protons, the binding energy for atomic orbitals is different. These binding energy values are characteristic of each element and can be used to distinguish between different elements in a sample. Comparison of binding energy from the spectra in figure 2.21 shows that binding energy for Au 4s orbital is larger compared to the binding energy in 4d and 4f orbitals, which means the Au 4s orbital closer to the nucleus. Also the spin-orbit splitting can be seen for Au 4p, 4d and 4f electrons, where single 4p, 4d amd 4f peaks are split into two peaks which is a result of spin-orbit interaction. The nuclear charge on Ta (atomic number 73) is smaller compared to the nuclear charge on Au (atomic number 79). Hence, the binding energies for Ta 4p and 4d orbital electrons is lower than the binding energy for

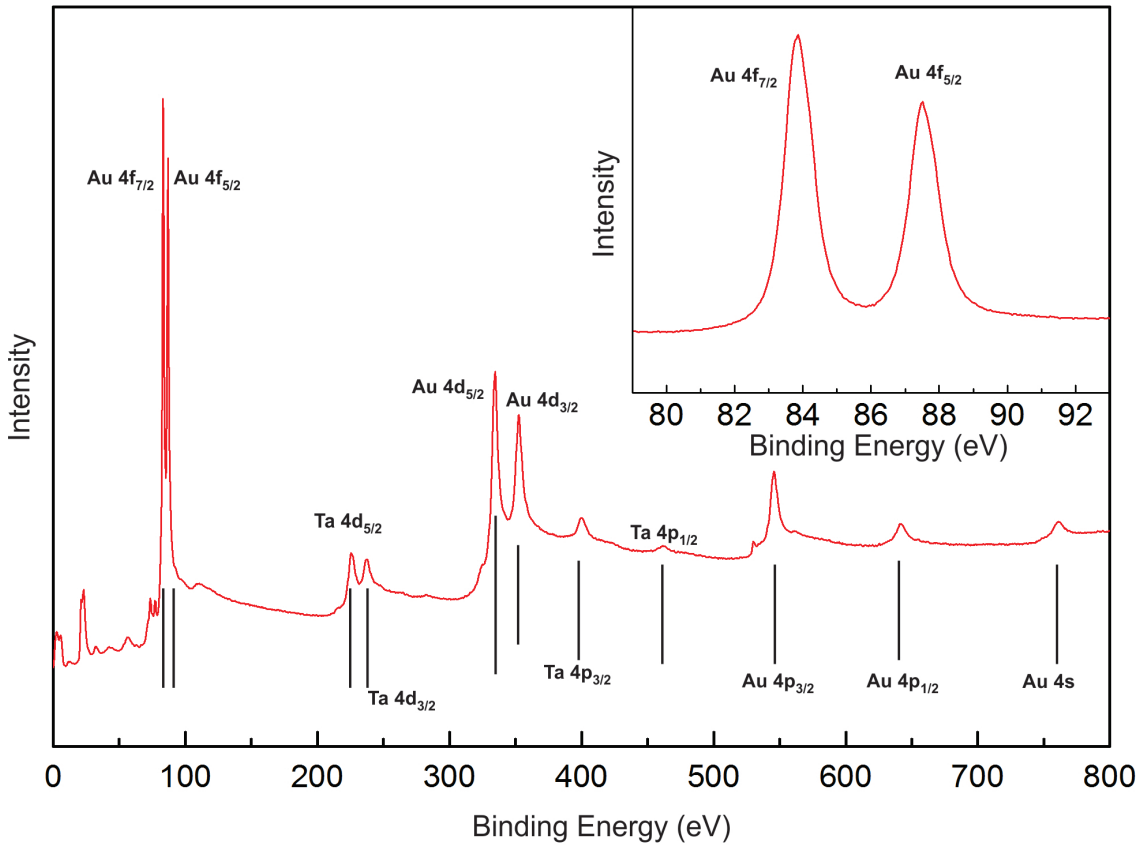

Figure 2.21: Example of Au(111) single crystal XPS. Inset shows the resolved $4f_{5/2}$ and $4f_{7/2}$ peaks for Au.

Au 4p and 4d orbital electrons due to weaker electrostatic interaction between the nucleus and electrons in Ta as compared to stronger interaction for Au.

It is clear that the XPS peaks are a chemical fingerprint of the elements. From the measurement of the exact energetic position of the core levels one can thus learn electronic properties of thin films on substrates. Figure 2.22 shows comparison of spectra obtained from clean Au(111) and multilayer spin-crossover film deposited on Au(111). Due to the presence of film, the electronic signal from the Au(111) substrate is suppressed, which is evident from the reduced intensity of Au(111) peaks. However, due to wide energy range and high intensity substrate peaks, the molecular peaks cannot be resolved due to strong

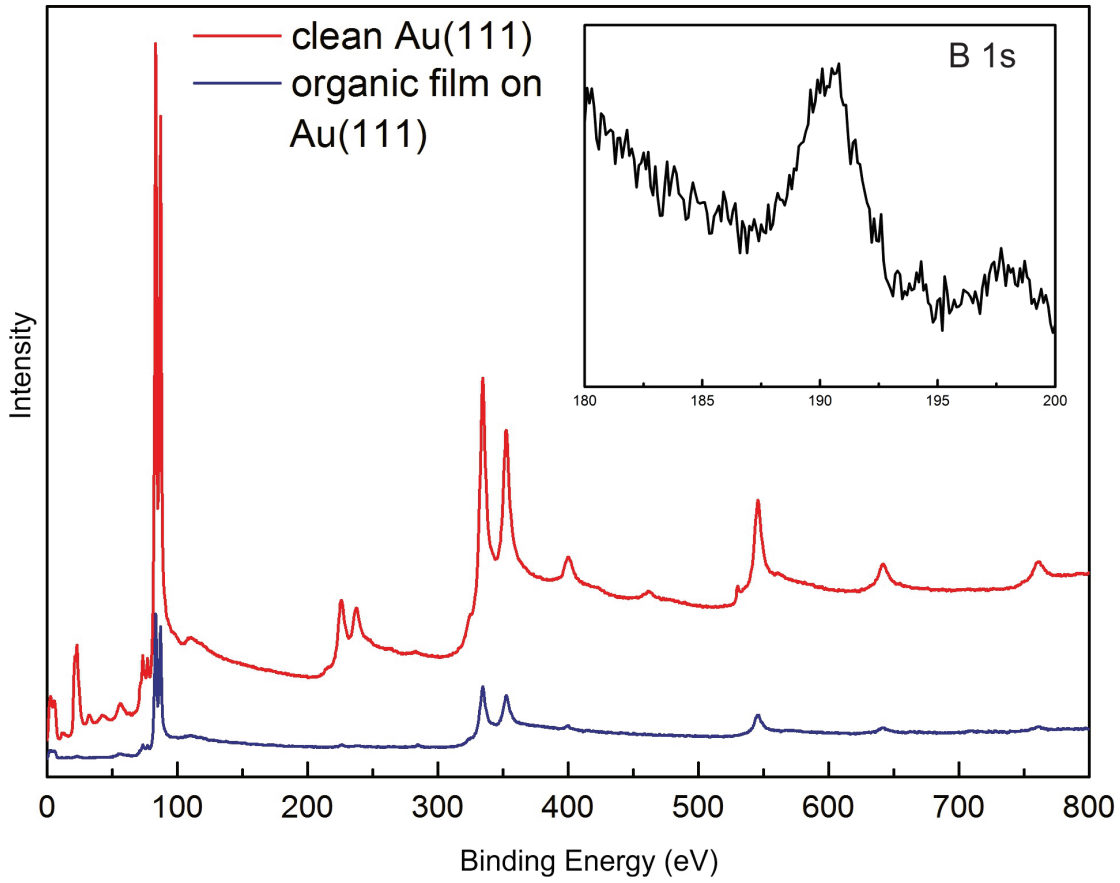

Figure 2.22: XPS spectra for single crystal Au(111) (red) and spectra with spin crossover film on top of Au(111) (blue). The inset shows the B 1s peak from the spin crossover molecule.

background signal from the substrate. As a result, the spectra from the elements in the molecule, such as Boron and Iron, was obtained after taking large number of scans. The Boron 1s peak from the molecule is shown in the inset obtained after taking over 150 scans. The substrate and molecular peaks can be used to estimate the thickness of the organic film as described in [93]. The simplest case can be envisaged as the overlayer of an element A on top of a substrate of element B. The intensity of electrons from overlayer, I_A, for an overlayer of thickness d as

$$I_A = I_A^{\infty}(1 - e^{\frac{-d}{\lambda_A}E_A cos\theta}) \tag{2.16}$$

where I_A^∞= is the intensity of the peak from pure element A and λ_A is the inelastic mean free path of electrons in element A, and E_A is the kinetic energy of the electrons from the overlayer.

The intensity of electrons from the substrate of element B is given by

$$I_B = I_B^\infty e^{\frac{-d}{\lambda_A} E_B cos\theta} \tag{2.17}$$

where E_B is kinetic energy of electrons from the substrate. I_B^∞ is the peak intensity from pure element B. Sometimes I_A^∞ and I_B^∞ are not available. The atomic sensitivity factors s_A and s_B which are proportional to I_A^∞ and I_B^∞ are used and the ratio of I_A and I_B can be written as

$$\frac{I_A/s_A}{I_B/s_B} = \frac{1 - e^{\frac{-d}{\lambda_A} E_A cos\theta}}{e^{\frac{-d}{\lambda_A} E_B cos\theta}} \tag{2.18}$$

To solve for d, one has to know the inelastic mean free path in overlayer and to maintain surface sensitivity of the measurements low energy peaks must be used in the equation. The equation 2.18 can be reduced to obtain the thickness of the overlayer film:

$$d = \lambda_A cos\theta \ln[1 + \frac{I_A/s_A}{I_B/s_B}] \tag{2.19}$$

Besides thickness determination, the XPS was used to study the electronic structure of Fe in the spin crossover films, which is discussed in detail in Chapter 5.

2.5.2 Ultraviolet Photoelectron Spectroscopy

Ultraviolet photoelectron spectroscopy (UPS) is a type of photoelectron spectroscopy technique that uses photons with wavelength in the ultraviolet region. The energy of these photons is lower (10-50 eV) compared to the energy of X-ray photons (1200-1500 eV). As a result, the UPS is able to probe the occupied energy levels below the Fermi level. The

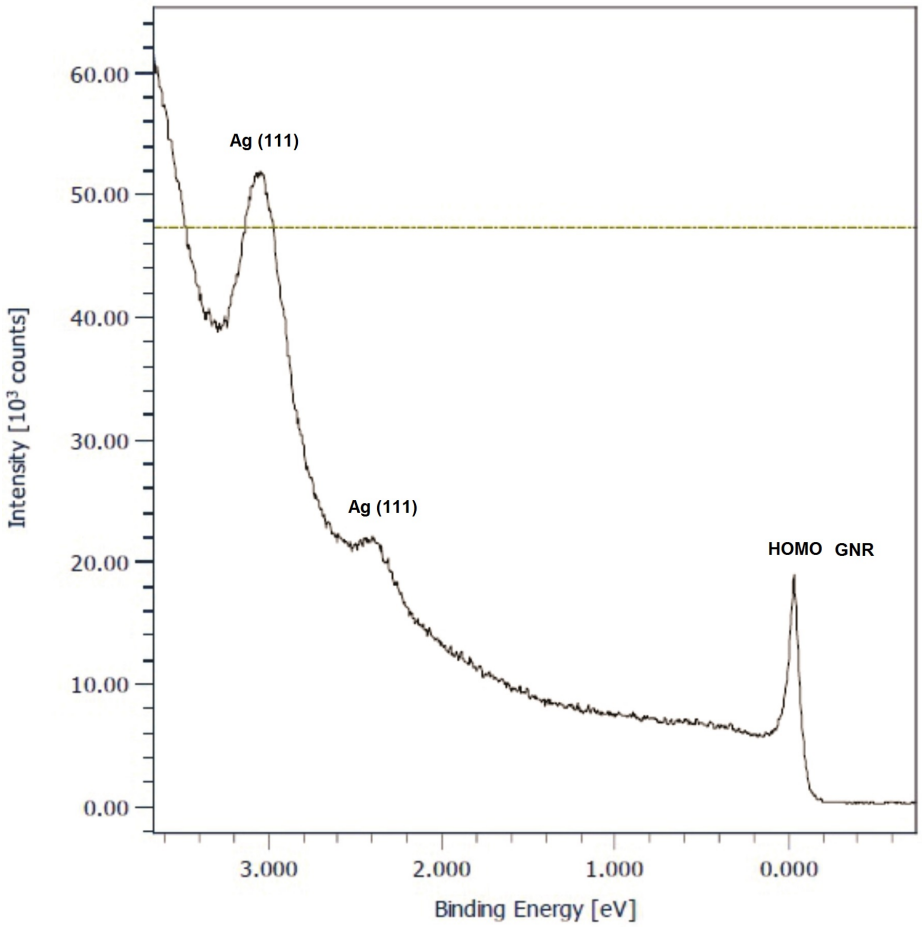

Figure 2.23: UPS spectra for graphene nanoribbons on Ag(111) substrate.

orbitals near the Fermi level take part in the bonding and electron transport in a material. Therefore, the UPS allows us to probe the valence band of a material. A useful application of the UPS technique is to experimentally measure the molecular orbital energies [94–96]. Compared to the solids, which have delocalized energy bands, the molecular orbitals are discrete. As a result, the UPS spectrum of a molecule contains a series of peaks each corresponding to one valence-region molecular orbital energy level.

Figure 2.23 shows the UPS spectra for a monolayer of graphene nanoribbons on Ag(111). The nanoribbons were synthesized by covalently linking anthracene molecules. The UPS signal consists of electrons coming from both the nanoribbons and Ag(111) substrate. The

energy states for Ag(111) can be identified by comparing the spectra with UPS spectra taken for clean Ag(111). The peak located right at the Fermi energy level (0 eV) is the highest occupied molecular orbital of graphene nanoribbons. This is one example of the application of UPS to identify the molecular orbitals.

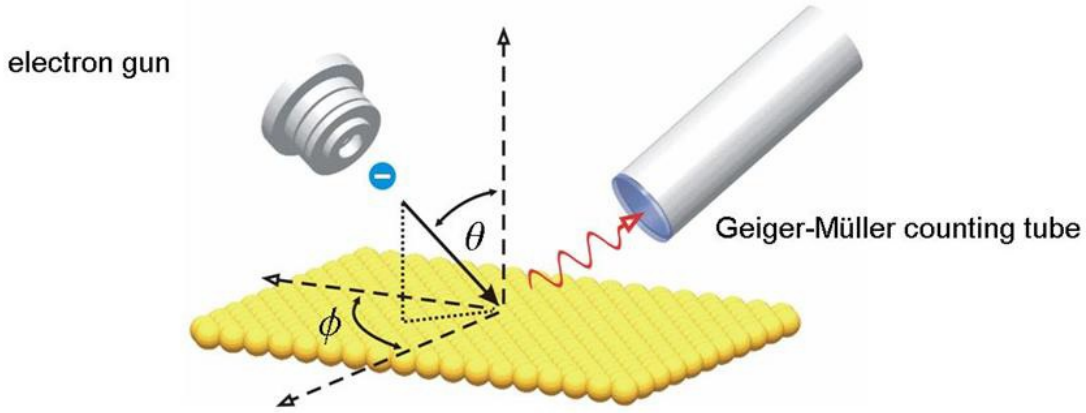

Figure 2.24: Schematic of IPES technique. [1]

2.5.3 Inverse Photoemission Spectroscopy

Inverse Photoemission Spectroscopy (IPES) is a technique which is based on the principle opposite of the photoemission spectroscopy. In the photoemission process "photons are absorbed by the atoms and the electrons are excited from bound state to unbound state". So, in inverse photoemission process "electrons are absorbed from the unbound state to bound state and photon is released by the absorbing atom" [1]. In IPES measurements a beam of electrons with energy $\leqslant$ 20 eV is directed at the sample. These electrons are absorbed by the high-lying unoccupied electronic energy states and then decay to low-lying unoccupied states. The photons are emitted when electrons decay to lower energy states. These photons are counted as a function of electron energy to obtain the IPES spectrum, which gives the unoccupied or the conduction band spectra for the sample under study. Since, the energy

of the incident electrons is very low, the penetration depth is limited to only a few atomic layers. This makes the IPES technique very surface sensitive. The IPES and UPS spectra can be combined to obtain the full band structure of a material [97, 98] and the difference between the highest occupied and unoccupied levels give the band gap for that material. Figure 2.24 shows the schematic for a typical IPES instrument.

All the techniques discussed above provide a comprehensive suite of surface science techniques to characterize molecular films. I have utilized these techniques to study three molecular systems on noble metal surfaces, as discussed in the next chapters. The STM was used to characterize topography of 2D and 3D molecular networks and STS was used to obtain LDOS and band gap of a molecular network. The photoemission spectroscopy was utilized to obtain the electronic structure and interface effects on electronic structure of the molecular thin films. Also, the position and shifts in XPS peaks were used to identify the chemical environment and hence bonding pattern in 2D molecular networks.

Chapter 3

Organic ferroelectric 3-hydroxyphenalenone

Molecular ferroelectrics (MFEs) are a special class of organic materials that exhibit a bistable electric polarization that can be reversed by applying an external electric field. Several of the popular FEs include polyvinylidene fluoride (VDF) based polymers [99] and oligomers [100], KH_2PO_4 (KDP) [101] and the recently discovered diisopropylammonium bromide (DIPA-B) [102]. However, in these FEs, the steric difficulty in reorienting dipoles gives rise to an exceptionally large coercive field compared with other inorganic ferroelectrics such as $BaTiO_3$ [100]. An alternative to polymer ferroelectrics is the proton transfer type systems. Interest in proton transfer type ferroelectrics is sparked by the recent discovery of ferroelectricity in croconic acid through switchable hydrogen bonds [103]. In spite of its small size, the corconic acid has spontaneous polarization of $20\mu C/cm^2$ as compared to $38\mu C/cm^2$ for $BaTiO_3$ [104]. The origin of the ferroelectricity in proton transfer type systems, such as croconic acid, is attributed to resonance assisted hydrogen bonds (RAHB), coupled with the π electron system. These systems can exist in two or more resonant structures and this resonance has two fold effect : shortening of hydrogen bond length

and π - electron delocalization. The RAHB is exhibited by molecules, such as carboxylic acid [105], cacodylic acid [106] and diketo enols [107]. Of particular interest to this thesis is proton transfer type ferroelectric 3-hydroxyphenalenone (3-HPLN) that exhibit RAHB due to ketone-enol moiety, shown in figure 3.1.

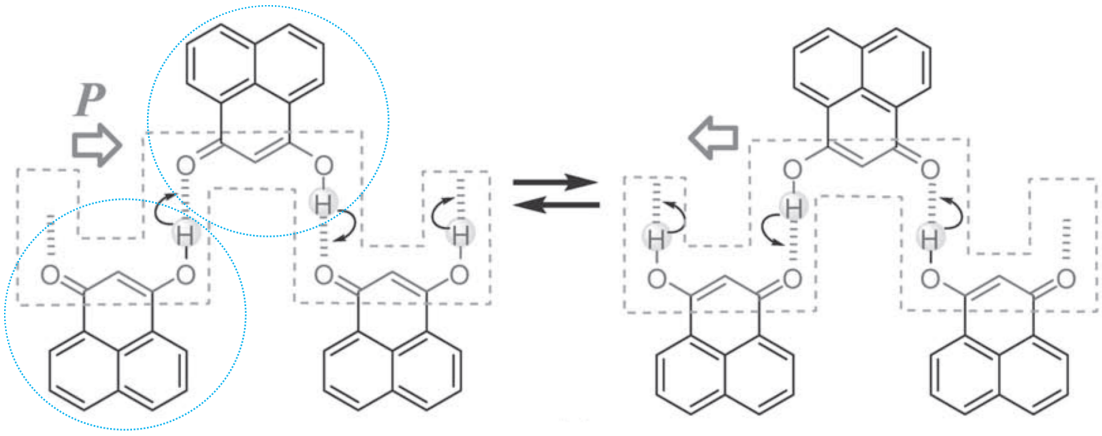

Figure 3.1: (a) Two resonant structures of 3-HPLN. The blue circle highlights one 3-HPLN molecule.

3-HPLN is one of the seven molecules recently found by Horiuchi et al. [108] after searching the cambridge structural database for possible ferroelectrics by looking for -diketone enol moities with polar crystal structures. Three of these molecules: croconic acid, rhodazonic acid and 3-HPLN are proved to be ferroelectric with polarization comparable to $BaTiO_3$ above room temperature, while other molecules exhibit very weak ferroelectricity. Croconic acid and rhodizonic acid has been studied in detail on various substrates [55, 109, 110]. The third molecule, 3-hydroxyphenalenone is the focus of this chapter. A remnant polarization in 3-HPLN originates from the unequal charges on the ketone and enol fragments. The 3-HPLN has remnant polarization of 3 $\mu C/cm^2$, coercive field of 6 kV/cm^2, Curie temperature of >450 K, and is commercially available. Figure 3.2(a) shows four unit cells of bulk 3-HPLN as seen along a-axis. The 3-HPLN molecules form infinite hydrogen bonded zig-zag chains along the a-direction as shown in figure 3.2(b) [108, 111].

These chains are perpendicular to O-H...O bonding direction and the remnant polarization of each zig-zag chain is along the [100] direction.

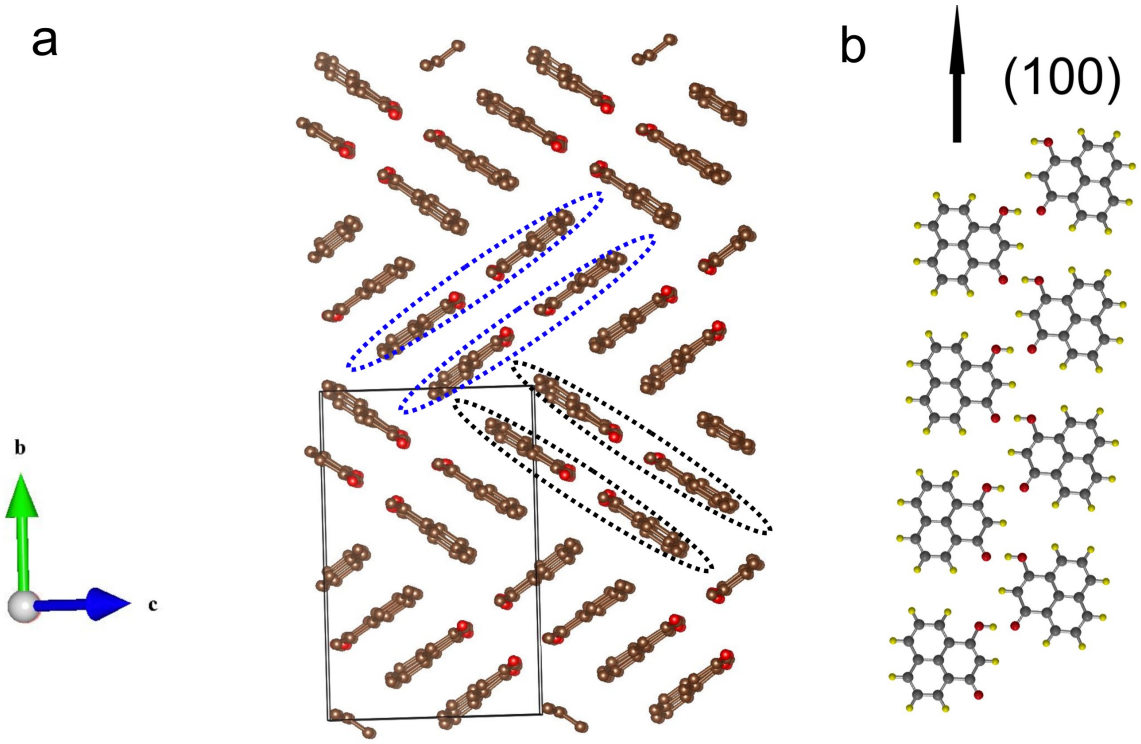

Figure 3.2: (a) Four unit cells of 3-HPLN crystal as seen along [100] direction. (b) Hydrogen bonded chains which lie along the electric polarization direction.

An external electric field applied to a crystal of 3-HPLN along the ferroelectric c-axis results in cooperative proton tautomerism, where the electric dipole is reversed via hydroxyl proton displacement with a concomittant change of the π electron system of each molecule. Since, the dipole and the H-bond are within the molecular plane, 3D structure is not required to observe ferroelectricity. Therefore, there is an interesting possibility that the surface supported two dimensional networks of 3-HPLN can have the similar H-bonded structural motifs similar to H-bonded chains seen in the bulk. Driven by this possibility, we investigated the self-assembly of 3-HPLN on Au(111), Ag(111) and Cu(111) substrates with the goal to stabilize and study single, H-bonded 1D chains of 3-HPLN using the ben-

efits of surface science. No other methods can do that. The 3-HPLN-Au(111) can be found in thesis by Kunkel [55].

3.1 Sample preparation

The Ag(111) and Cu(111) single crystal substrates were cleaned with repeated cycles of Ar^+ ion sputtering and subsequent annealing to approximately 650 °C. The substrate cleanliness was checked through STM imaging. 3-HPLN with 98% purity, was purchased from Acros Organics. 3-HPLN was thermally evaporated in a homebuilt Knudsen cell evaporator onto the cleaned Ag(111) and Cu(111) substrates. Post-deposition annealing procedures varied with the samples, and specific annealing temperatures are found in the next sections. All samples were cooled to liquid nitrogen temperature for imaging.

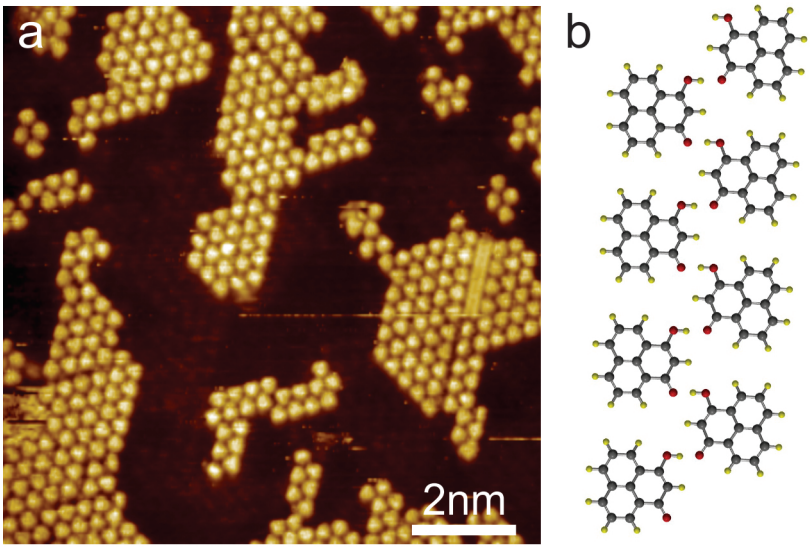

Figure 3.3: (a) STM image after room temperature deposition of 3-HPLN on Ag(111), 1 V, 400 pA (b) structure model of hydrogen bonded 3-HPLN chains.

3.2 2D structures of 3-HPLN on Ag(111)

As seen in the STM image in figure 3.3(a), when deposited onto Ag(111) at room temperature, 3-HPLN coalesces into short chains that are two molecules across, similar to the chain-like arrangements observed in the bulk 3-HPLN crystal structure [108, 111]. The zipper-like chains are packed on the surface to form small clusters. Due to the short length of the chains, of just a few nanometer (nm), there exists a high level of disorder in the networks. The chains are oriented along the <110> directions of the surface. These chains are H-bonded, with each molecule forming a single H-bond to two different molecules along the chain length as illustrated in figure 3.3(b), reminiscent of the bulk crystal structure. The chains must attract each other through van der Waals interactions since, within the model, the chemically active hydroxyl and carbonyl groups are already participating in hydrogen bonding so that no further H-bonds between the chains can be formed.

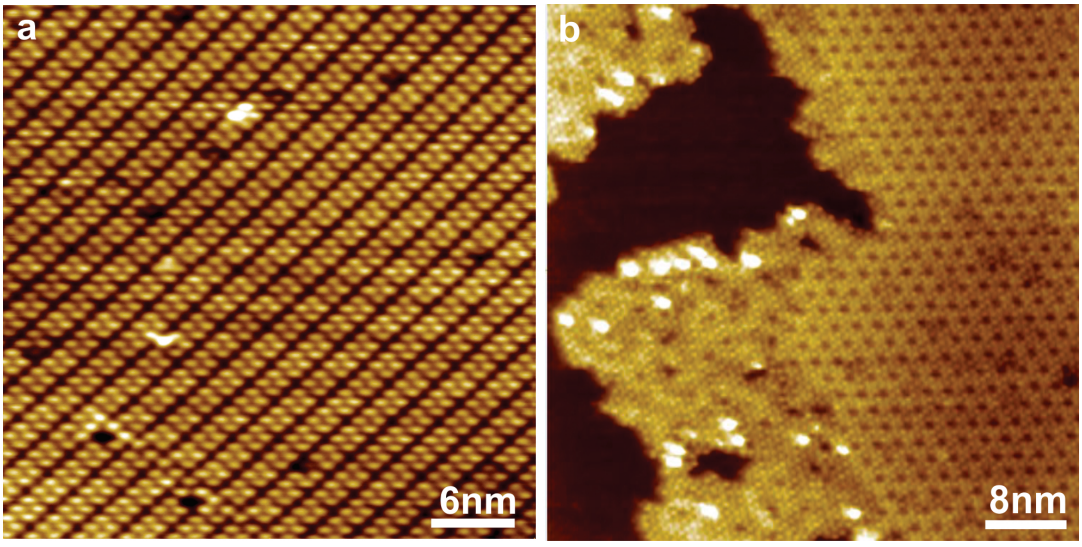

Figure 3.4: STM image after annealing to 400 K (a) dimer based molecular network (b) porous trimer based network.

Annealing the sample to approximately 100 °C drastically changes the structure of 3-HPLN on Ag(111), with the emergence of a new ordered network. Figure 3.4 shows

two molecular networks formed after annealing the sample grown at room temperature to 100 °C. We note that only one type of network is formed at once. Dimer based (figure 3.4(a))and trimer based (figure 3.4(b)) networks are not found to coexist, when utilizing the same sample preparation procedures. This shows that several structural configurations of similar energy coexist. However only the trimer based structural phase is discussed here.

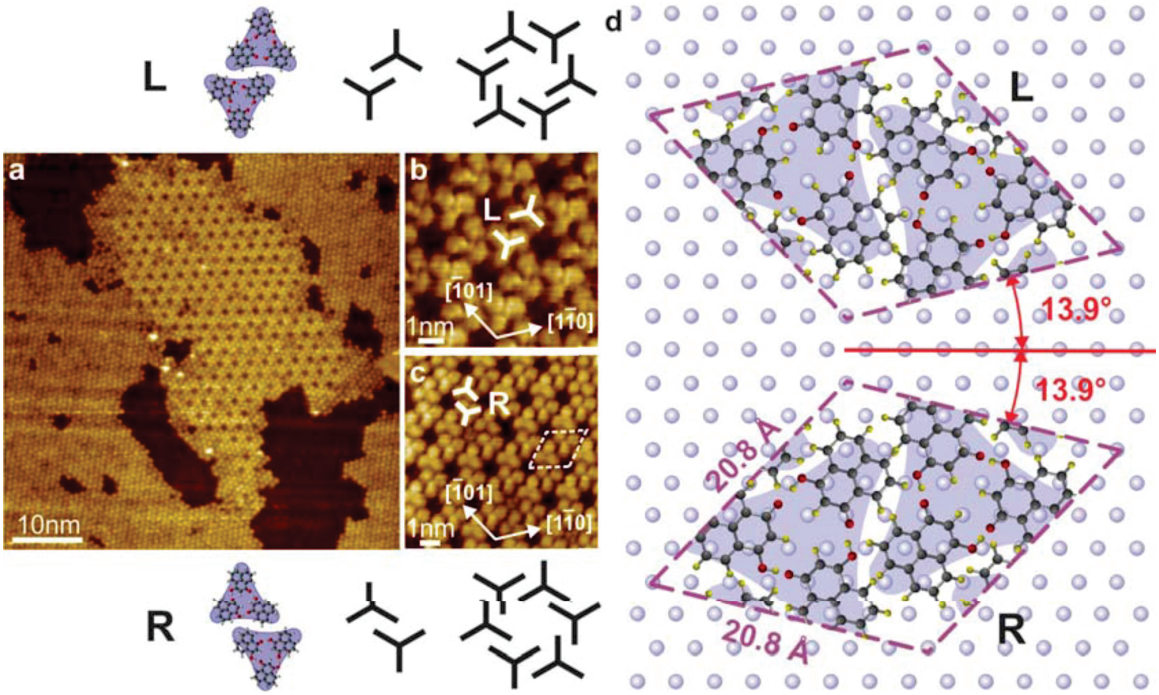

Figure 3.5: Networks of 3-HPLN on Ag(111) after annealing the sample to 100 °C, followed by cooling to 77 K for STM imaging. (a) STM image highlighting the coexistence of a close packed phase and trimer network phase of 3-HPLN on Ag(111). (b, c) Examples of STM images of left and right-handed networks (enantiomorphs). The structural unit cell is highlighted by dashed lines in (c). Tunneling parameters: (a) -0.2 V, 600 pA; (b) + 0.2 V, 600 pA; (c) -0.2 V, 500 pA. (d) Bonding schematic of two trimers in a unit cell and how this leads to L (lefthanded) and R (right-handed) chirality. The epitaxial orientation of the unit cell to the substrate is described as $(2\sqrt{13} \times 2\sqrt{13})R13.9^{\circ}$ in Woods notation. Also shown is how dimers of trimers assemble to form handed porous networks.

The basic building block of the ordered network shown in the STM image (Figure 3.5 (a)-(c)) is a trimer of 3-HPLN. Two trimers within a rhombus represent the unit cell of the

extended network, as highlighted in figure 3.5(b) and (c) with white dashed lines and illustrated in figure 3.5(d). From the STM images, the dimensions of unit cell were measured to be 21.5 Å. By measuring the uncovered Ag(111) surface with atomic resolution, it is found that the unit cell of 3-HPLN make an angle of 12.6° ± 2.2° with the underlying <110> direction of Ag(111) surface. These measurements correspond to a commensurate ($2\sqrt{13}$ x $2\sqrt{13}$)R 13.9° 3-HPLN/Ag(111) lattice.

Each 3-HPLN within the trimer has a single H-bond with each of its two nearest neighbors. Since each carbonyl and hydroxyl group participates in a hydrogen bond within the trimer, there are no carbonyl/hydroxyl groups left to form hydrogen bonds between trimers. It is therefore reasonable to presume that these networks must be held together by van der Waals forces only, similar to the chain-like room temperature phase. It is clear from the STM images that the trimer networks are porous. In some cases, 3-HPLN molecules were observed within the pores. We believe these to be kinetically hindered 3-HPLN molecules, or a lattice imperfection. Figure 3.5(d) shows a schematic of a 3-HPLN trimer coming together to link with an adjacent trimer via the presumably weak van der Waals interactions. From these dimers of trimers, models of left-handed (L) and right-handed (R) extended chiral networks in the STM images in (b) and (c) were constructed, and are also shown in Figure 3.5(d). The van der Waals attraction between adjacent trimers in the porous lattice works as an effective lock and key mechanism, giving the islands long range order.

The structure of the C_{3h}-symmetry, 3-HPLN trimer is reduced to C_3 symmetry upon adsorption to the Ag(111) surface (neglecting the atomic arrangement of the underlying surface atoms). As shown in figure 3.5(d), this allows a handedness (left or right) to be defined for the cluster, depending on whether the direction of the O-H..O hydrogen bonding contact point in a counterclockwise direction around the trimer's center of mass (like in the top of figure 3.5(d)) or in a clockwise direction (bottom of figure 3.5(d)). The lack of a mirror plane or glide plane of symmetry perpendicular to the surface gives the adsorbed

3-HPLN trimer local surface chirality at the point group level. Importantly, it is noted that while each pair of 3-HPLN trimers in figure 3.3(d) is shown with only one type of trimer, i.e. each trimer within the pair has the same handedness, there is no reason why this must be the case unless the mechanism by which they form induces it.

The STM images do not reveal the handedness of individual molecules or trimers, but it is reasonable to assume that each chiral network can be made up of a random mixture of right and left-thanded trimers, giving rise to an overall racemic mixture. However, the asymmetric (tilted) packing of the trimers with respect to the diagonals of the unit cell ensures that the extended model networks exhibit surface chirality at the space group level, regardless of the underlying molecular orientation. The extended network resembles others reported in the literature, for example those formed from melamine on Au(111) [112, 113], titanyl-phthalocyanine (TiOPc) on Ag(111) [114], perylene tetra-carboxylic diimide (PTCDI), melamine on a silver-terminated silicon surface, or self-assemblies of SubPc on Au(111) [115–118]. What is further striking here is that the epitaxial orientation of the porous 3-HPLN network adsorbed to Ag(111), described as (2 $\sqrt{13}$ x 2 $\sqrt{13}$) R13.9°, is identical to the epitaxial orientation of TiOPc on Ag(111). Considering the differences between 3-HPLN and TiOPc, namely their chemical constituents and intramolecular bonding, symmetries, and different attachments to the surface, we believe this epitaxial fit to be, at least in part, a coincidence. But, an interesting point to take away from the similarities between the two networks is that two qualitatively similar STM images can be obtained from completely different molecules, even molecular clusters,with different types of intermolecular bonding. This suggests that there might be a common principle guiding the chirality and porosity of networks comprised of very different building blocks. Several of the porous networks reported in the literature are mentioned alongside ones which are close-packed. For example, the energy of a porous network of melamine on Au(111) was lower than that of a close-packed alternative, since the strength of the hydrogen bonding

interaction was maximized within it [112].

3.3 3D networks on Cu(111)

The growth of molecular layers is dependent on the substrate, as I will show in this sec-

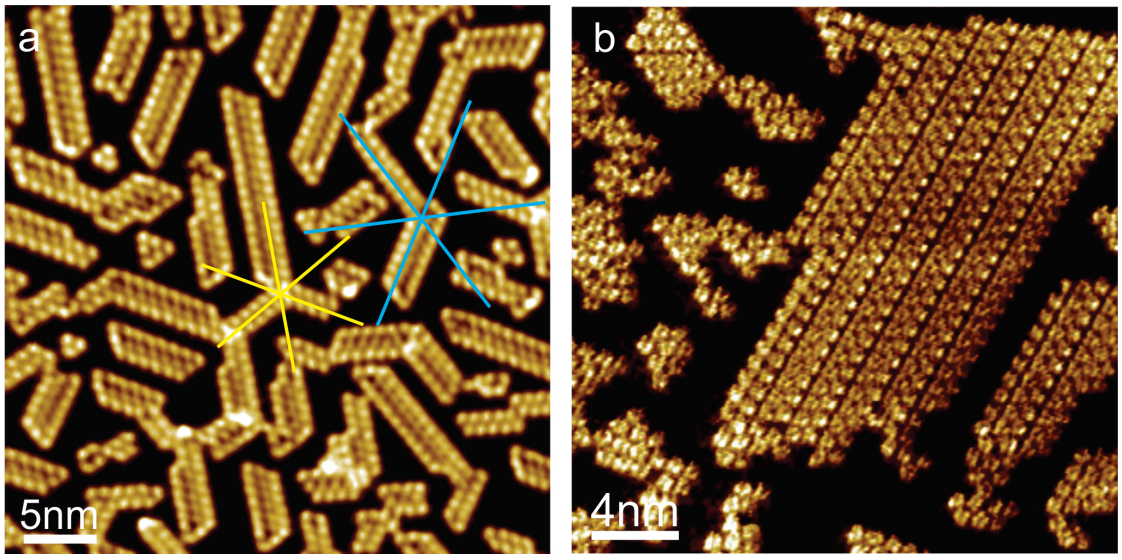

Figure 3.6: (a) Scanning tunneling microscopy image of a sub-monolayer of 3-HPLN deposited on Cu(111) at room temperature. Highlighted are 6 distinct direction of island orientation. 1 V, 500 pA (b) sub-ML coverage after annealing to 120 °C. -1 V, 500 pA.

tion. Deposition of 3-HPLN at room temperature results in elongated islands, two or three molecules wide and several nanometers long, as seen in the STM image, figure 3.6(a). These islands are formed by small double and triple molecular rows. These rows are oriented along 6 distinct directions, as indicated by yellow and blue lines in figure 3.6(a). While we were not able to simultaneously resolve 3-HPLN and the Cu substrate atoms to establish the epitaxial relation. We attribute such an alignment to the epitaxial orientation of the molecular rows with the substrates close-packed directions, under consideration of the chirality of the molecules. Double rows can be modeled by 3-HPLN zipper-like chains similar to bulk 3HPLN. The size of each molecule is 7 Å and molecular spacing across

a double row is 9 Å, which indicates hydrogen bonding between the molecules in double rows with hydrogen bond distance of 2 Å. The third row is slightly farther from the double rows, which suggests van der Waals interaction between double rows and individual 3-HPLN molecules. Post-annealing the sample to approximately 120 °C and higher results in the growth of the 2D islands due to Ostwald ripening. The arrangement of the molecules in those islands corresponds to hydrogen-bonded 1D chains as in the bulk, which form 2D islands likely through van der Waals attraction, as can be seen in figure 3.6(b).

Only if the coverage of 3-HPLN is sufficiently high, exceeding two nominal layers, then post-annealing of the room temperature-deposited molecules to 200 °C drastically changes the morphology of the film, as seen in figure 3.7(a). We observe double layers of 3-HPLN consisting of two competing structures, a linear one and a honeycomb structure. Important structural details can be obtained from high-resolution STM images such as those in figure 3.7(b)-(d). Molecules in the second layer appear as lines as compared to elliptical shape in the first layer. Center-to-center distance between two lines is about 3.5 Å and end-to-end distance is 6 Å. End-to-end distance between two pair of lines is 14 Å. As each 3-HPLN molecule is 7 Å wide and 7 Å long, a pair of lines cannot be one flat lying molecule as it would mean adjacent molecules are touching or slightly overlapping. Due to this, we have to consider the possibility that molecules in the second layer are standing upright on top of flat lying molecules in the first layer and each bright line in the second layer represents one molecule. While we were unable to fully resolve the molecular arrangement in the bottom layers, it is clear that it is different for the linear- and the honeycomb-like layers as seen in figure 3.7(c) and (d), and also distinctively different from the annealed single layers in figure 3.6(b). This leads us to conclude that the double layers have to be interpreted as a three-dimensional structure in which both layers form as one structure at the same time during the annealing, rather than merely being two layers added together.

Here we focus on the structure of the honeycomb-like layer, figure 3.7. The symmetry

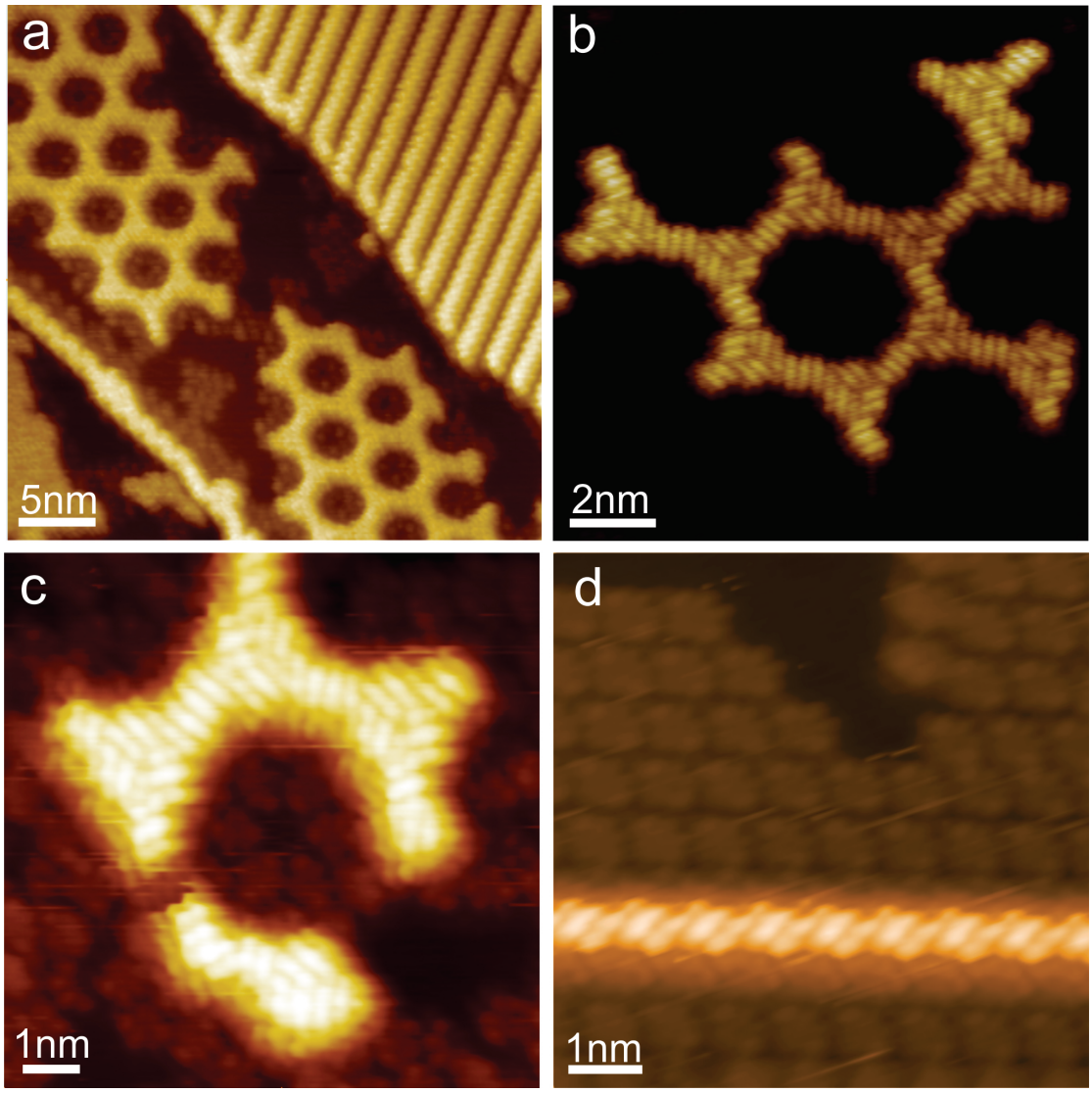

Figure 3.7: (a) Approx. 2 ML of 3-HPLN, after annealing to 200 °C, 1 V, 500 pA (b) images of honeycomb structure with contrast adjusted to show top layer (c) the contrast has been adjusted to enhance the visibility of the first ML (d) linear chain in the second layer with contrast adjusted to show the underlying layer.

of the lattice is reminiscent of a Kagome lattice, as is outlined by the interlacing triangles shown in figure 3.9(a). It is noted that Kagome lattices create two types of voids and in the present structure one type of those voids is extremely small. The hexagons and triangles are formed by the molecules in the top layer only. High-resolution STM images, including

those taken on incomplete layers revealed important structural details. The STM images of second layer suggest that molecules form π-π bonded dimers, which are then stacked into the honeycomb structure. Linear segments of two dimers are connected on both ends to chiral, pinwheel-like junctions consisting of three dimers. The chirality of the pinwheel junctions is the same for all junctions within a network, giving the symmetrized 2D network a six-fold rotation axis of symmetry (p6 wallpaper group) and overall space group chirality. Repeated film preparation has yielded both chiralities.

While the bottom layer of the bilayers is mostly hidden by the top layer, STM images of incompletely assembled top layer structures such as those in figure 3.7(c) provide clues about the make-up of the bottom layer. Bottom layer molecules are visible inside the hexagonal pores of the Kagome lattice, and they apparently arrange themselves in a circular fashion within the exposed area, leaving a pore in the center. The analysis of several images taken near defects in the top layer reveals a remarkable similarity of the bottom layer with the chiral porous monolayers observed for 3-HPLN on another substrate, Ag(111) [119]. As described in previous section, the fundamental building blocks of those networks on Ag(111) are planar trimers of 3-HPLN, which are arranged into a network with ($2\sqrt{13}$ x $2\sqrt{13}$)R13.9° epitaxial orientation to the substrate. The resulting pore-to-pore distance is 2.08 nm, which is considerably smaller than the 4.4 $\pm$ 0.2 nm measured for the present structures. Based on the structure information from this STM study and comparison to the networks of 3-HPLN on Ag(111), we developed the structure model of the bottom layer shown in figure 3.8(c). It is also based on the most stable trimer of 3-HPLN, but their relative orientation is different compared to their arrangement on Ag(111), creating a larger unit cell. The most stable trimer labeled α is shown in figure 3.8(c). The six of these trimers are fitted together to make a hexagon labeled Σ. The hexagon Σ has two shells, the inner shell labeled Γ has 6 molecules, when built to scale matches with the inner shell Γ shown in figure 3.8(b). When hexagons Σ are fitted together to build the first layer, the pore-

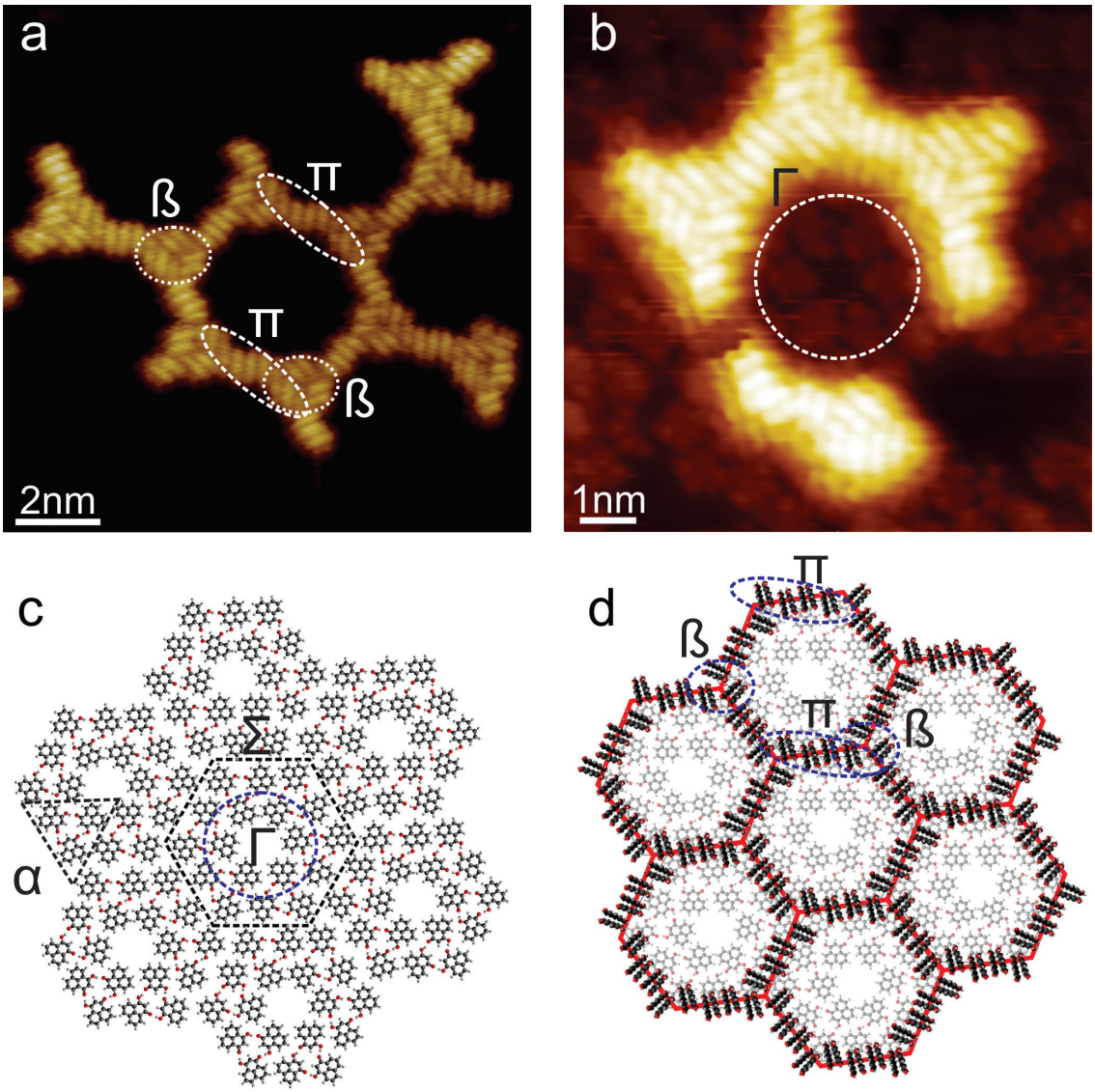

Figure 3.8: (a) Hexagon in the second layer, -0.6 V, 500 pA (b) partial hexagon with visible molecules in the first layer, -0.3 V, 600 pA (c) first layer molecular model by fitting the 3HPLN trimers (d) molecular model with standing second layer on top of flat lying first layer.

to-pore distance also matches with the 4.4± 0.2 nm. The second layer can be modeled on the basis of DFT calculated tetramer (π) and hexamer (β) as shown in figure 3.8(d). This model matches remarkably well with our experimental observations, resembling basic features and dimensions as shown in figure 3.8(a)-(d). However, it should be noted that

this structure has never been observed with STM in monolayers of 3-HPLN on Cu(111), for any annealing temperature up to 240 °C. It is thus concluded that this porous layer of 3-HPLN might only be stable in a bilayer arrangement on Cu(111), whereas single layers always seem to prefer linear chain formation.

It is not possible to determine the exact orientation of the molecules from STM images. I collaborated with computational chemists to explore the network achitechture in detail using geometry optimization based upon density functional theory (DFT), specifically the exact alignment of the molecules within the lattice. The computational models are described in the electronic supplementary information [120]. The study of a unit cell of the entire double layer was computationally too expensive, and further hampered by the uncertainty in the structures of both the bottom and the top layer. Therefore the analysis of the molecular network was limited to small free and supported model clusters, such as dimers, tetramers and hexamers, to investigate structural features of the top layer. The most stable clusters from the DFT calculations are summarized in figure 3.9(b)-(d), while other clusters considered and their relative energies are given in the supplementary information in reference [120]. First, it was established that the molecules in the most stable π-π stacked free dimer are aligned such that the carbonyl group of one molecule is in juxtaposition with the hydroxyl group of the other one. This alignment of the two 3-HPLN molecules results in tilted hydroxyl hydrogens towards the carbonyl oxygens, adding hydrogen bond character to the dominating intermolecular π-π stacking. The preferential stacking of two such dimers into a free 1D chain is such that the O- and OH-containing ends of neighboring dimers point in opposite direction (Figure 3.9(c)). Interestingly, the lowest energy pinwheel junctions consist of three dimers that are different from the lowest energy free dimer in that the two molecules within a dimer are identically aligned (Figure 3.8(b)). It appears that such an alignment enables a shared hydrogen bond between the two hydroxyl Hs in one dimer and one carbonyl O of a neighboring dimer. The DFT calculations further

showed that the alternating dimer arrangement is no longer preferred upon attachment of two 3-HPLN dimers to a flat-lying layer of 3-HPLN on a Cu slab in a fashion seen in the STM image in figure 3.8(c). Aligning all dimers with their functional groups towards the bottom layer (Figure 3.8(d)) lowers the energy by 0.4 eV per molecule, as compared to the alternating dimer arrangement (Figure S6 in supplementary information [120]).

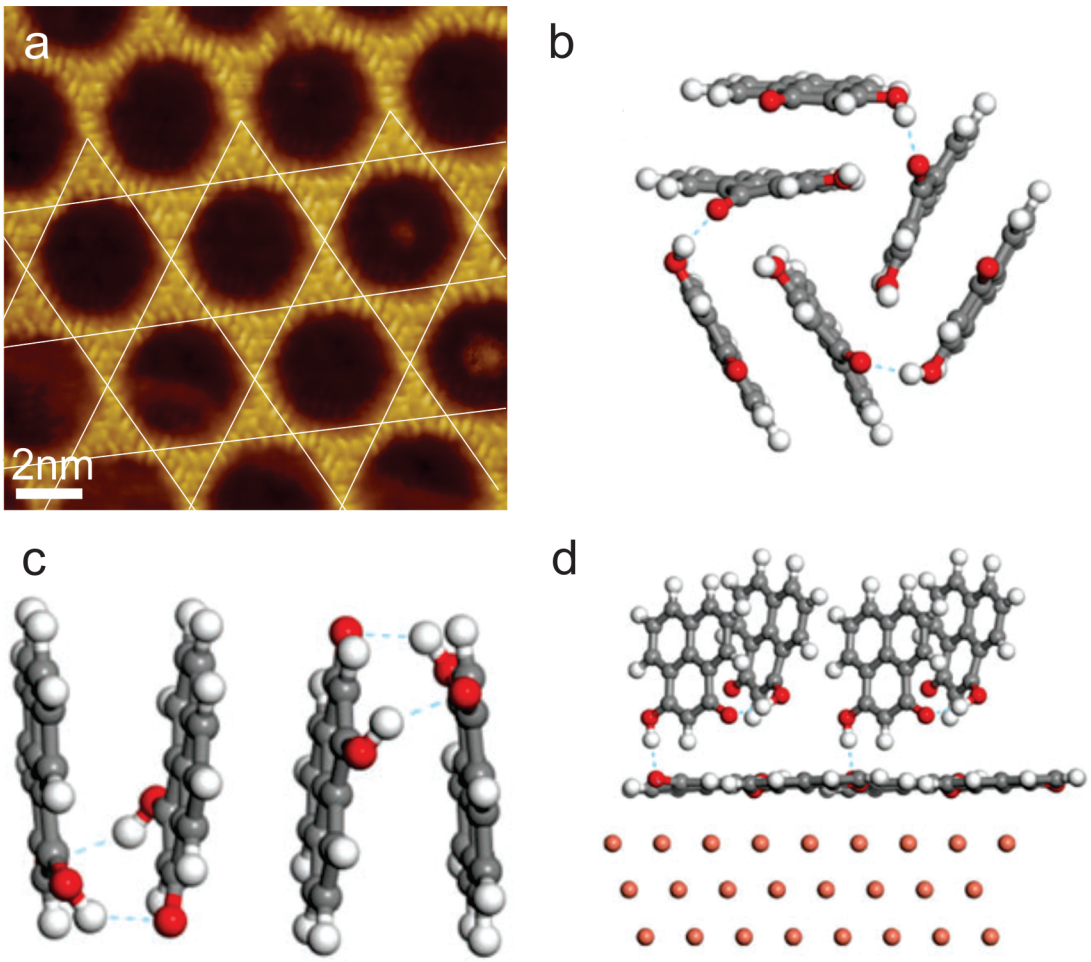

Figure 3.9: (a) Images of honeycomb structure with contrast adjusted to show top layer (b) lowest energy hexamer obtained from DFT (c) lowest energy free teramer obtained from DFT (d) two supported dimers on flat-lying molecules and Cu(111) slab (side view).

We did not consider metallation of the organics using substrate atoms or deprotonation of the 3-HPLN in our simulations. Metallation has been reported for several organic

species on Cu(111), since Cu atoms become readily available on the surface at sufficiently high temperature [121]. For instance, we reported the formation of a metalorganic coordination network of the structurally related rhodizonic acid on Cu(111) after moderate annealing to approx. 90 °C, [122] i.e. at lower annealing temperature than what we used in this study. An immediate indicator for metallation is the degradation of the substrate, i.e. jagged step edges and holes within the terraces, [122] which we never observed for the 3-HPLN-Cu(111) system. Deprotonation of organics is also frequently observed on Cu(111). Deprotonation typically increases the reactivity of the organics, and reports from the literature often show deprotonation occurring simultaneously with metallation, [121–123] in some instances catalyzed by the lattice gas of Cu atoms [124]. The absence of any structural degradation in the Cu surface is a hint against metallation and deprotonation, and we note that metallation and deprotonation, if present, would mainly affect the bottom layer.

In conclusion, the outstanding feature of the self-assembled 3-HPLN Kagome lattices on Cu(111) is the double-layer structure where the molecules in the top layer form pi-pi stacked dimeric building blocks, which are attached perpendicular to the bottom layer. The bottom layer most likely consists of planar trimers of 3-HPLN, which we reported earlier. Importantly, this structure only exists in a bilayer, whereas single layers of 3-HPLN exhibit entirely different molecular arrangement. This dependence of the structure of both layers on each other means that the film structure is in fact three-dimensional. This remarkable feature distinguishes the present system from other layer-by-layer grown systems with perpendicular molecule attachment, such as terephtalic acid on Cu(100) [125]. However, the combination of pi-pi stacking and perpendicular attachment is in striking analogy to the crystal structure of 3-HPLN in the bulk [111]. The discovered structure does not only represent a rare example of a three-dimensional arrangement of molecules on a two-dimensional surface, it involves molecules that exhibit ferroelectricity from hydrogen bond ordering in bulk crystals.

3.4 Conclusion

To conclude this chapter, for 3-HPLN molecule, the structure observed depends on the substrate. For Au(111), the 1D chains are observed that are reminiscent of the ferroelectric chains in the bulk. On Ag(111), two different networks are observed: dimer based islands and trimer based porous network. On Cu(111), the formation of the network depends on the molecular coverage as well as the annealing temperature. Hydrogen bonded islands are formed at submonolayer coverages after annealing the 120°, whereas as porous honeycomb networks are formed when coverage is increased above a monolayer and samples are annealed to 200°. The common feature of all the network is the hydrogen bonding between the neighboring molecules. Also, the addition of π - π stacking on Cu(111) results in the formation of 3D self assembled network.

Chapter 4

Structural and magnetic properties of Fe(II) spin-crossover complex

4.1 Background and current state of research

4.1.1 Ligand field effects in transition metals

The chemistry of transition metal cation complexes is driven by the valence d-orbital electrons. This chemistry can be utilized in the synthesis of metal-ligand complexes with switchable magnetic properties. These complexes, named spin-crossover complex, can exhibit different magnetic states. For a free transition metal atom, all five atomic d-orbitals are degenerate (d_{xy}, d_{yz}, d_{zx}, d_{z^2} and $d_{x^2-y^2}$) i.e., they have the same energy. In metal coordination complexes, the perturbation of the symmetry of local environment can lift the degeneracy of the five d-orbitals of a transition metal ion, such that the orbitals are split into a subset of three orbitals, namely d_{xy}, d_{yz} and d_{zx}, which are referred as t_{2g}. The term ”t” refers to triply degenerate orbitals and ”g” refers to the inversion symmetry of the wavefunction of these orbitals. These orbitals are of nonbonding nature so their energy is

lowered with respect to the energy of atomic orbitals. The second subset orbitals, namely d_{z^2} and $d_{x^2-y^2}$, which are referred as e_g, is of anti-bonding type and therefore have higher energy than the nonbonding orbitals t_{2g}. Here "e" refers to the doubly degenerate orbitals and "g" refers to the inversion symmetry of the wavefunction of these orbitals. The splitting between t_{2g} and e_g orbitals is due to ligand field effect and is described by a ligand field splitting parameter, Δ. The various factors that determine the magnitude of Δ, are discussed below:

(a) **Oxidation state of ion**

For a given metal, the Δ increases with the increase in the charge on the metal atom. The interaction between the metal ion and the ligand is partly electrostatic. The greater the charge on the metal, the closer the approach of the ligand and the stronger the overlap between the metal and ligand orbitals results in large splitting of orbitals.

(b) **Number and geometry of ligands**

The more ligands are bonded to the metal ion, the larger the d-orbital splitting. This splitting is greatest when the ligand geometry allows direct overlap between the ligand orbitals and a metal d-orbital. Such overlap occurs for linear, square planar, and octahedral geometries. Also, the size of a ligand is significant, because closer a ligand can approach the metal, the better the orbital overlap and consequently the larger Δ. Thus smaller ligands tend to have larger Δ than larger ligands. This trend can be seen in halide ligands, where Δ is inversely related to their size : $I^- < Br^- < Cl^- < F^-$

(c) **Chemistry of metal-ligand bonding**

The essential feature of a coordination compound is the donation of a pair of electrons by the ligand to form a coordinate covalent bond with the metal. A strong σ bonding interaction between the metal and the ligand results in a set of low energy,

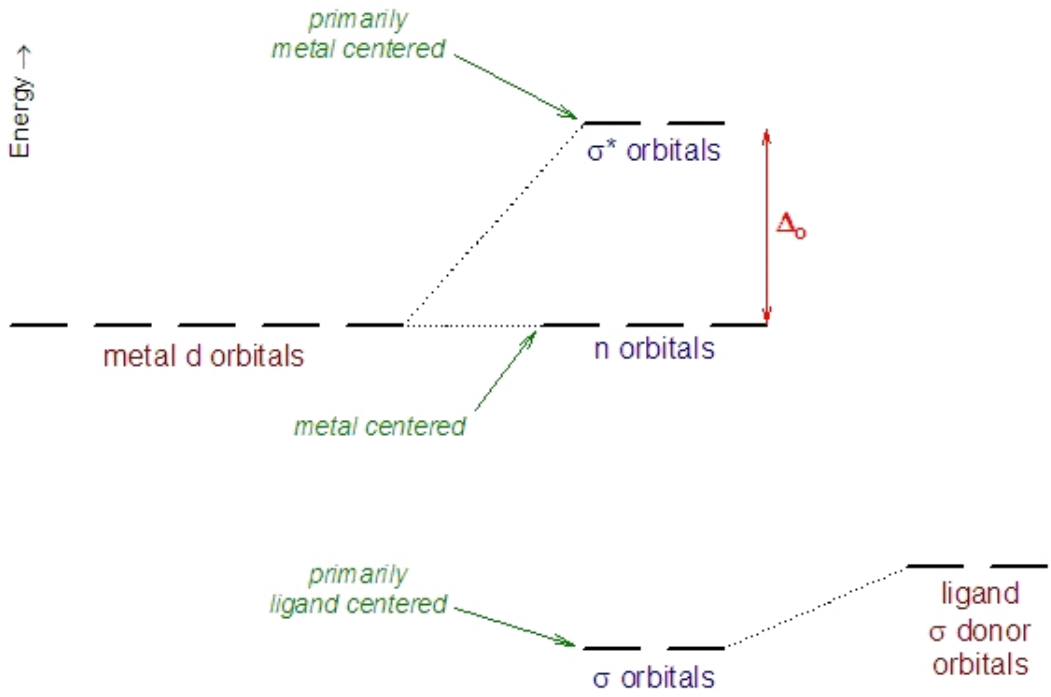

Figure 4.1: Molecular orbitals representing σ metal-ligand interaction (source: http://www.chm.davidson.edu/vce/coordchem/Ligands.html).

fully occupied σ bonding orbitals that are primarily localized on the ligand and a set of high energy σ* orbitals that are primarily localized on the metal. Three of the metal orbitals (d_{xy}, d_{xz}, and d_{yz}) do not interact with the ligand orbitals and remain as nonbonding orbitals completely centered on the metal, shown in figure 4.1. The d-orbital splitting arises from the increase in energy of the σ* orbitals relative to the nonbonding orbitals. The stronger the bonding interaction, the higher the σ* energy and the greater Δ. A strong σ bonding interaction requires a good energy match between the metal and the ligand. Empirically, there is a correlation between Δ and the basicity of the ligand. A ligand that is a good base tends to form strong σ bonds with metals and thus produces a relatively large Δ.

Some ligands are capable of π bonding interactions, either by acting as a π acceptor or a π donor. The energy diagram shown in figure 4.2(a) illustrates the behavior of a π donor ligand on Δ. The π bonding behavior is similar to that for the σ bonding. The occupied ligand orbitals are lower in energy than the metal orbitals. Thus the new π orbitals, like the σ orbitals, are of low energy and are fully occupied. In addition, these orbitals are localized primarily on the ligand. The metal d orbitals that had been nonbonding in the σ-only case now become π^* orbitals and are shifted to higher energy, which results in a decrease in the magnitude of Δ. By contrast, a ligand with π-acceptor properties has unoccupied orbitals at energies well above the metal d_{xy}, d_{xz}, and d_{yz} orbitals with which mixing occurs to form π and π^* orbitals shown in figure 4.2(b). In this case, the π^* orbitals are localized on the ligand. The former nonbonding d orbitals now become π orbitals and are shifted to lower energies, thus increasing Δ.

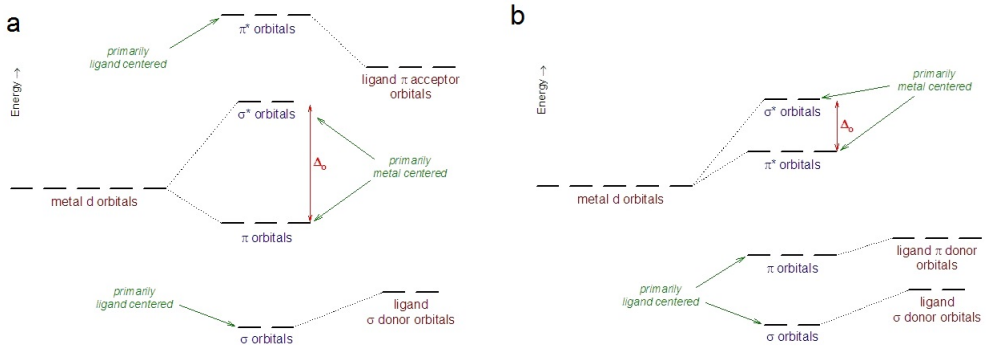

Figure 4.2: Molecular orbitals representing π metal ligand interaction (source: http://www.chm.davidson.edu/vce/coordchem/Ligands.html).

Based on σ and π interaction properties, the ligands can be arranged in a spectrochemical series in the order of increasing value of Δ, from π donor ligands on left to π acceptor ligands on the right: $I^- < Br^- < S^{2-} < SCN^- < Cl^- < NO_3^- < N_3^- < F^- < OH^- < C_2O_4{}^{2-} \leqslant H_2O < NCS^- < CH_3CN < py(pyridine) < NH_3 <$

$$en(ethylenediamine) < bipy(2,2' - bipyridine) < phen(1,10 - phenanthroline) < NO_2^- < PPh_3 < CN^- \leqslant CO.$$

These ligands described in the spectrochemical series can be utilized to synthesize the metal coordination complexes with interesting magnetic properties as described in the next section.

4.1.2 The physics of spin-crossover in organics

The splitting of d-orbitals can determine the occupation of those levels for cations with d^4 to d^7 electronic configuration. For example, for a metal cation with six d-electrons, two possibilities can be envisaged for placing electrons in t_{2g} and e_g orbitals. If the energy splitting between t_{2g} and e_g orbitals is less than the electron-electron repulsion energy , the electrons will occupy the five d orbitals according to Hund's rule, which results in 4 unpaired electrons. Such a metal complex will exhibit paramagnetic ground state, called high-spin state (HS). If the energy level splitting is larger compared to the electron-electron repulsion energy, six d-electron occupy the three t_{2g} orbitals in pairs such that there are no unpaired electrons. This diamagnetic state is called low-spin(LS) state with no net magnetic moment. Figure 4.3 shows the electronic configuration for high spin and low spin state for d^6 electronic configuration for $[Fe(H_2B(pz)_2)_2(bipy)_2$ complex.

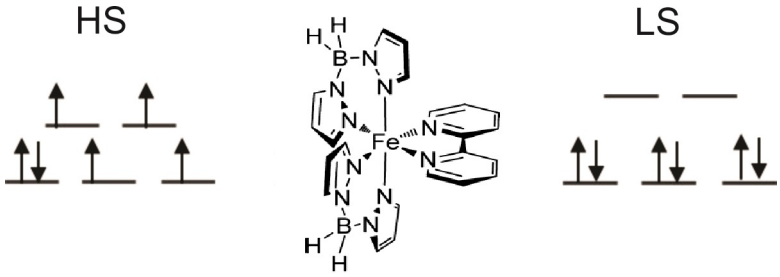

Figure 4.3: The electronic configuration for two possible ground state configurations for d^6 electrons in octahedral coordination for $[Fe(H_2B(pz)_2)_2(bipy)_2]$ complex.

It is possible for some metal complexes to switch between high spin state and low spin state under external perturbation. This phenomenon is termed as spin crossover or spin-state transition. The external perturbation to trigger the spin-state transition can be temperature, pressure, electric and magnetic field, light, x-ray or chemical stimuli as described in the next section.

4.1.3 Experimental studies of SCO complexes in bulk

Figure 4.4 shows four such complexes that have been experimentally demonstrated to

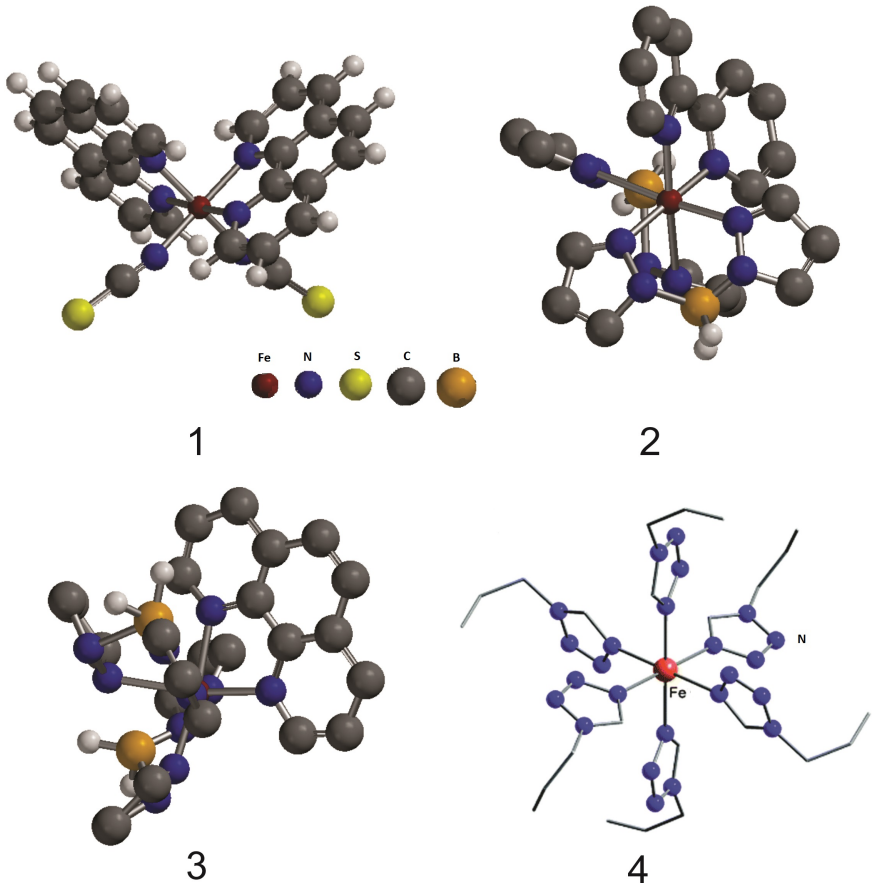

Figure 4.4: Four most commonly studied SCO complexes,
1:$[Fe(phen)_2(NCS)_2]$, 2:$[Fe(H_2B(pz)_2)_2(bipy)_2]$, 3:$[Fe(H_2B(pz)_2)_2phen]$,
4: $[Fe(ptz)_6(BF_4)_2]$.

exhibit spin crossover under external stimuli.

1. **[Fe(phen)$_2$(NCS)$_2$]**

   The experimental studies of [Fe(phen)$_2$(NCS)$_2$] complex has shown that it exhibits transition between high-spin(S=2) and low spin state (S=0) under temperature [126], pressure [34], light [36] and electric field [126]. The thermal spin transition for this complex can be directly observed with SQUID measurements, where this complex exhibits change in the magnetic moment as the temperature is varied [126]. Miyamachi et al. [126], have also demonstrated the thermal spin transition using XMCD measurements on the powder, shown in figure 4.5(a). They observed change in the line shape at Fe L_3 and L_2 edge and they argued that these lineshapes are characteristic of spin state of molecules.

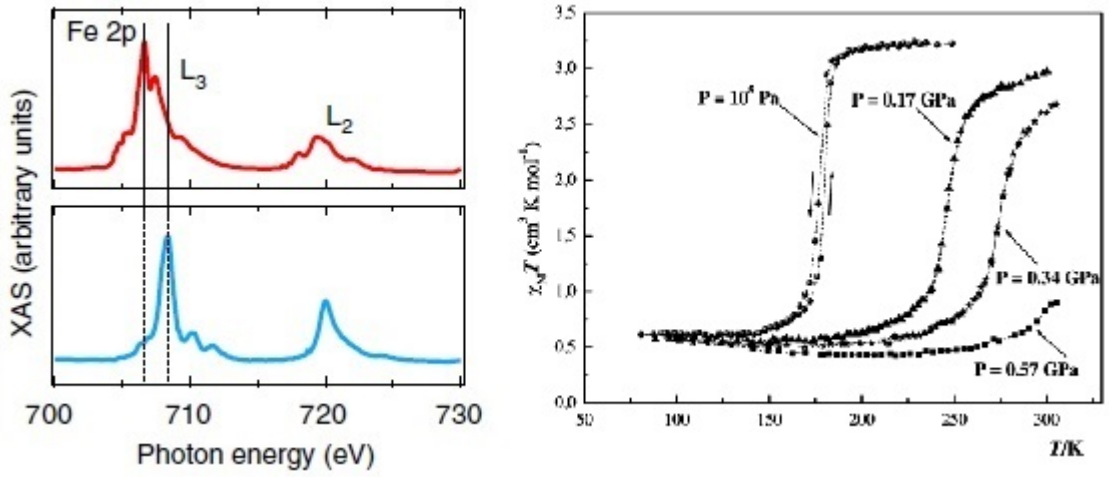

Figure 4.5: (a) The Fe 2p XAS spectra for powder [Fe(phen)$_2$(NCS)$_2$] sample at 200 K (HS state:top), 100K (LS state:bottom). [126] (b)Magnetic susceptibility of [Fe(phen)$_2$(NCS)$_2$] as a function of temperature and pressure [34].

In addition to temperature, Ksenofontov et al., [34] have used pressure to demonstrate spin transition in this complex, especially increase in the transition temperature. Pressure increase causes compression in the ligand-metal bond distance which

in turn increases the ligand field. This higher ligand field increases the energy gap between the t_{2g} and e_g energy levels as discussed earlier. This effect is illustrated in figure 4.6(b), in which the product of magnetic susceptibility with temperature of $[Fe(phen)_2(NCS)_2]$ is plotted against temperature for a range of pressures [34]. Clearly increasing the pressure increases the transition temperature of the SCO, which means that the molecules that are in HS state at 200 K and 10^5 Pa pressure switch to LS state at 200 K under 0.17 GPa pressure. Further increase in pressure shifts the transition temperature to higher values.

2. **$[Fe(H_2B(pz)_2)_2(bipy)_2]$**

The thermal spin transition for powder $[Fe(H_2B(pz)_2)_2(bipy)_2]$ complex has been demonstrated using the SQUID measurements [36, 127, 128]. This complex exhibits LS (S=0) state below 120 K, gradual thermal spin transition from LS to HS state from 120K to 180K and HS state above 180 K as seen in the SQUID [127, 128]. Also Warner et al., [127] observed change in line shape at Fe L_3 and L_2 edge XAS spectra for this complex across the spin-transition. Interestingly, Naggert et. al. [36], demonstrated the spin transition in this complex at 10 K using laser irradiation. This complex is in LS (S=0) state at 10 K, when the powder sample is irradiated by 525nm light, the SQUID measurement shows finite magnetization as shown in figure 4.6(a). This effect is called light induced excited spin state trapping (LIESST). The molecules that absorb, usually green, laser light are excited into a higher energy state, which then subsequently decays (with a certain probability) into the HS state [129]. At 10 K the HS molecules are essentially frozen and cannot relax back into the LS state, i.e. the energy barrier to get to the LS state is too high at such low temperatures. However, these molecules relax back to LS state when temperature is increased above 10 K.

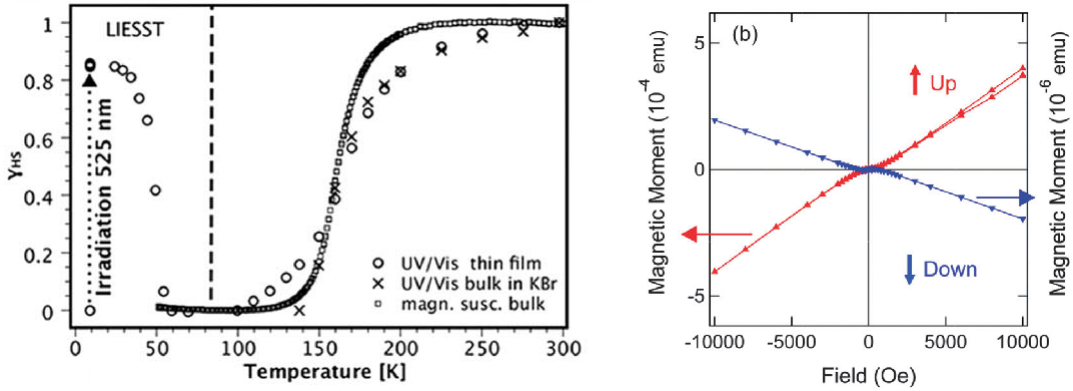

Figure 4.6: (a) The Squid data for laser irradiated $[Fe(H_2B(pz)_2)_2(bipy)_2]$ [36]. (b) Magnetic properties of 25 monolayer films of $[Fe(H_2B(pz)_2)_2(bipy)_2]$ on PVDF-TrFE substrate [35].

Another interesting study for this complex was done by Zhang et. al., [35]. Using inverse photoemission spectroscopy and SQUID measurements, they demonstrated that 10-25 monolayer thick films on ferroelectric substrate PVDF-TrFE exhibit spin states dependent on the direction of the ferroelectric polarization of the substrate. Figure 4.6(b) shows the magnetic moment as a function of magnetic field for 25 monolayer thick films of $[Fe(H_2B(pz)_2)_2(bipy)_2]$ on ferroelectric PVDF-TrFE. The films exhibit paramagnetic HS state(red curve, measured at 170 K) even down to 100 K, when the ferroelectric is polarized "up". Diamagnetic behavior is evident with PVDF-TrFE polarized down (blue curve, measured at 100 K).

3. **$[Fe(H_2B(pz)_2)_2phen]$**

The thermally induced transition for this molecule is demonstrated by Zhang et. al., using SQUID measurement and XAS spectra [130]. This complex shows sharp thermal spin transition at 165 K and the XAS spectra at Fe L_3 and L_2 exhibits similar change in the line shape as has been observed for the other two complexes, shown in figure 4.6(a). Interestingly, Naggert et. al. [36], demonstrated the spin transition in this complex at 10 K using laser irradiation. Naggert et al., [36], demonstrated the

spin transition in this complex at 10 K using laser irradiation similar to the LIESST effect observed for $[Fe(H_2B(pz)_2)_2(bipy)_2]$ complex. This complex is in LS (S=0) state at 10 K. When the powder sample is irradiated by 525 nm light, the SQUID measurement shows finite magnetization as shown in figure 4.7(b).

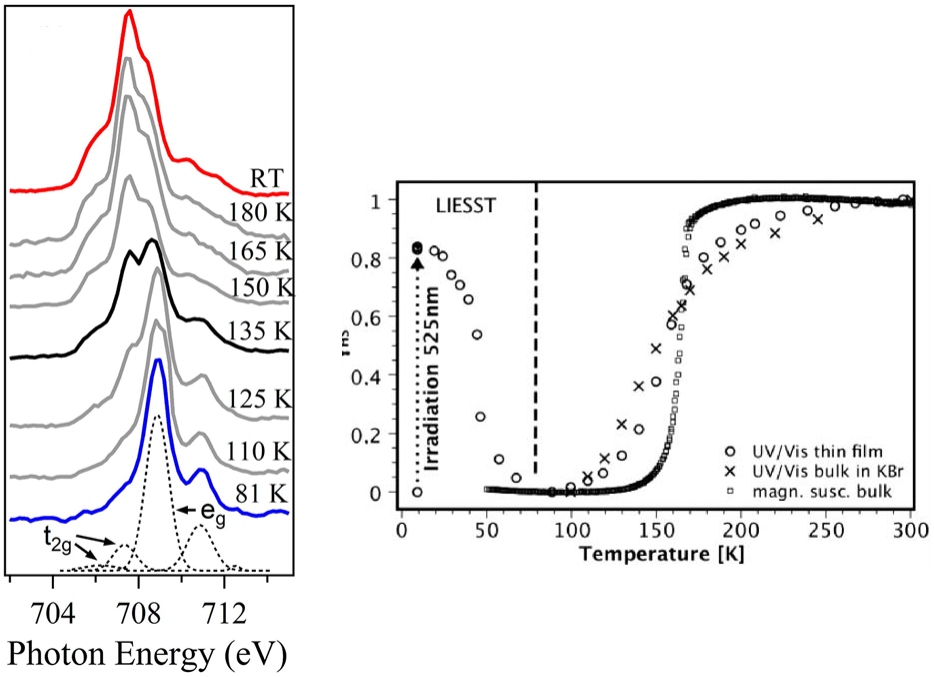

Figure 4.7: (a) The XAS spectra for powder $[Fe(H_2B(pz)_2)_2phen]$ sample. (b) The SQUID data for laser irradiated $[Fe(H_2B(pz)_2)_2phen$ [36].

4. **$[Fe(ptz)_6(BF_4)_2]$**

The XAS and Squid are the most common methods to observe spin transition in powdered samples. However, Son et al., [2] used the change in the electronic structure of Fe to demonstrate photoinduced and thermal spin transition in $[Fe(ptz)_6(BF_4)_2]$. They used photoemission spectroscopy to study the spin-crossover complex to identify the electronic changes in the XPS due to spin-state transition. They found that the Fe $2p_{3/2}$ spectrum in the HS state is accompanied by a charge-transfer satellite and this satellite feature is absent in the LS state as shown in figure 4.8.

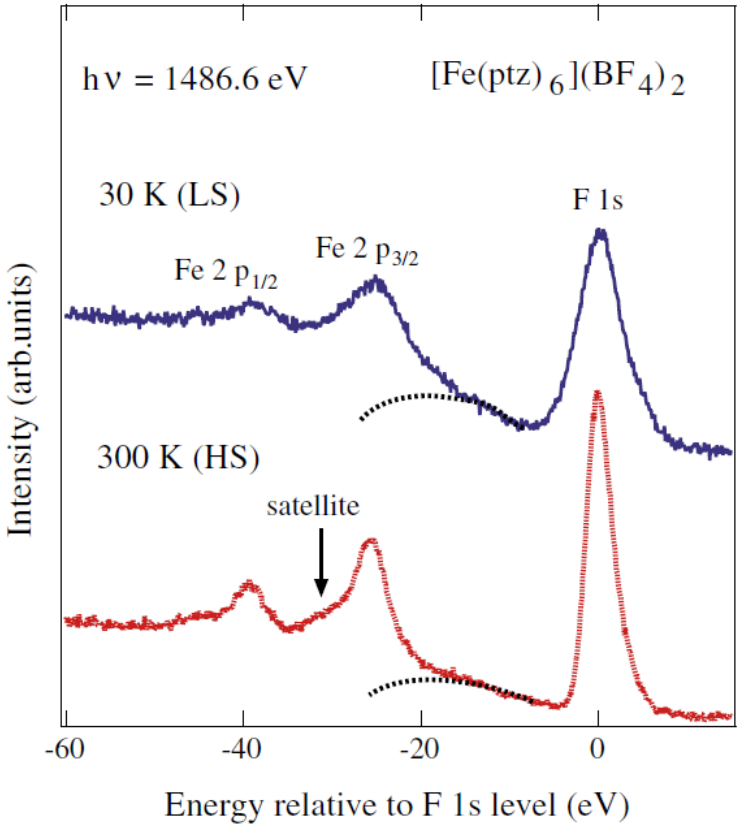

Figure 4.8: The XPS spectra for powder $[Fe(ptz)_6(BF_4)_2]$ [2].

4.1.4 Spin-crossover in surface supported Fe(II) complexes

The SCO complexes have been studied extensively in powdered samples and experimental methods for studying bulk samples are well established as described in the previous section. There are very limited studies for these complexes on substrates in thin film configuration. When considering these complexes deposited on top of a surface, the influence of the substrate has to be considered too. The effect of the substrate on spin-transition of SCO complexes has been compellingly demonstrated in a number of studies. It is shown that the SCO transition of modestly thick supported films can be similar to that of powders [128], studies done on various Fe(II) complexes do show that the HS-LS transition can change considerably with respect to the bulk behavior when prepared as a monolayer

or submonolayer thin film on a substrate surface [35, 126, 127, 131, 132]. The substrate thus becomes an important parameter to alter the SCO behavior by manipulating the transition temperature and the cooperativity between molecules. For instance, Miyamachi et al. [126, 132] showed that a HS-LS transition cannot be induced by a local electric field in $[Fe(phen)_2(NCS)_2]$ molecules on Cu(100) at 5 K, but that a reversible switching is possible on CuN/Cu(100). Similarly, Gopakumar et al. [131] found that the spin state of $[Fe(H_2B(pz)_2)_2phen]$ molecules ($H_2B(pz)_2$=bis(hydrido)-bis-(1H-pyrazol-1-yl)borate) in single monolayers on Au(111) appears to be locked in. The spin state of the molecules cannot be switched using the electric field from the STM tip. However, the molecules in a second layer can be reversibly switched between HS and LS states using the electric field from the tip of a scanning tunneling microscope (STM), as shown in figure 4.9(a)-(c).

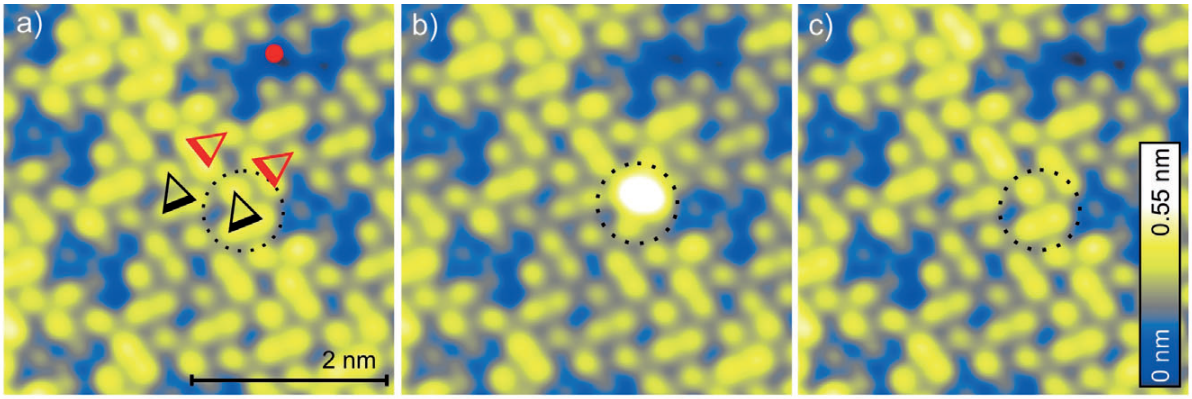

Figure 4.9: STM images of bilayer [Fe(H_2B(pz)$_2$)$_2$phen] on Au(111) at 5K (a) a 3V voltage pulse is applied over red dot. (b) The molecule in dotted circle in LS state is switched HS state indicated by increased conductivity and brightness of the molecules. (c) HS-LS switching was obtained by pulsing directly above the HS molecule in (b) [131].

For a similar complex [Fe(H_2B(pz)$_2$)$_2$(bipy)$_2$, Pronschinske et al., [133] showed that bilayer films have coexistance of HS and LS state across spin transition temperature. Their STM images show dark and bright areas, which they attributed to different conductivities of molecules in HS and LS state, shown in figure 4.10(a)-(d). They argue that the bright

and dark spots in the bilayer films do not change across the thermal spin transition temperature. Therefore, the bilayer film have mixture of molecules in HS and LS states across the thermal spin transition temperature, and the spin state is locked.

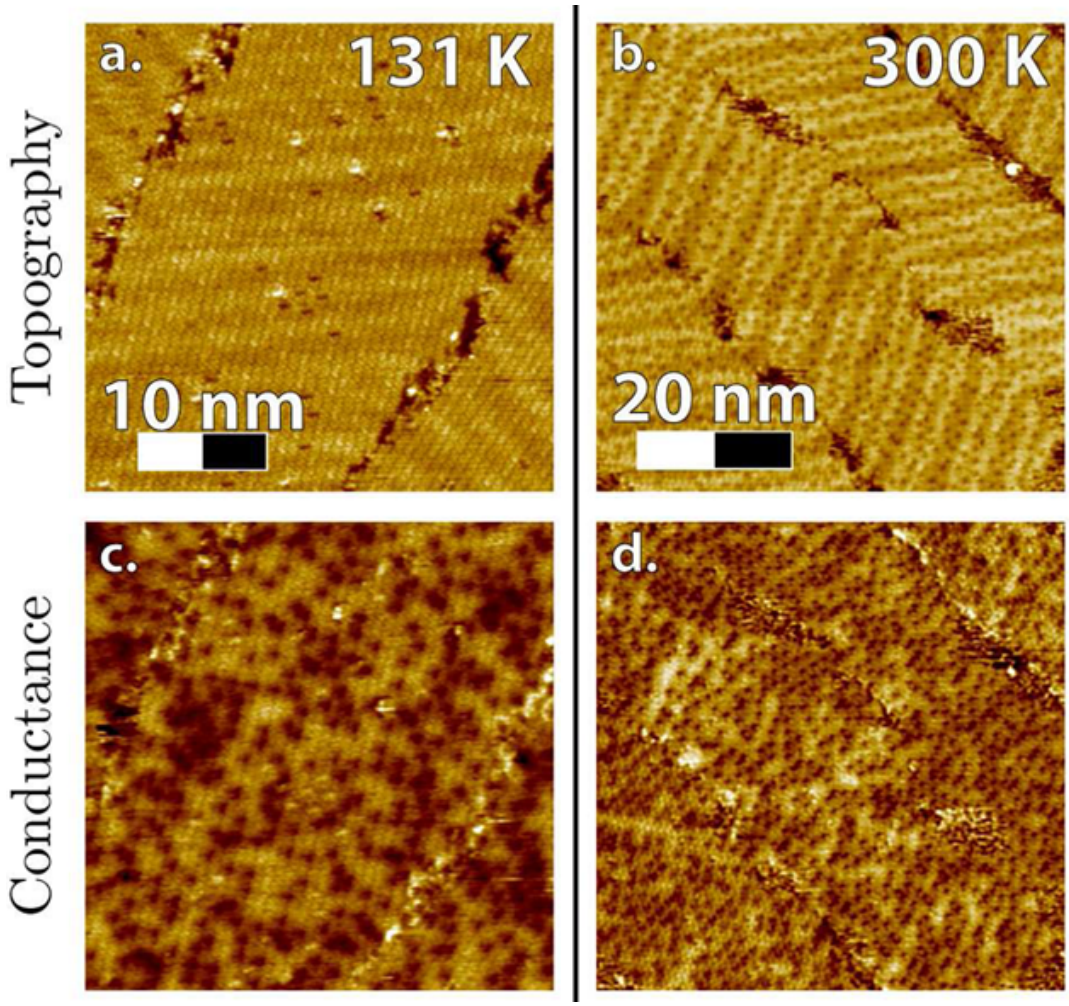

Figure 4.10: STM images of bilayer $Fe(H_2B(pz)_2)_2(bipy)_2$ on Au(111) at (a) 131K (b) 300K (c)-(d) corresponding conductivity maps at 131 K and 300 K. [133]

These studies evidenced that the coexistance of HS and LS across transition temperature for thin films. STM results for $[Fe(phen)_2(NCS)_2]$ suggest that the conducting substrate has a significant influence on the SCO transition [126], and there seems to be general consensus that a conducting substrate will tend to pin more than 50% of several SCO com-

plexes in the high spin state even well below the SCO transition temperature [127, 131]. While it is clear that coordination effects and cooperativity of SCO complexes are critically dependent on the substrate, detailed knowledge of fundamental interactions at the molecule-substrate interface and how they can be exploited to control the spin crossover effect, needs to be established through basic research before those materials can be considered for organic spintronics applications.

In this section, we demonstrate how the spin state of SCO molecules is affected by a supporting substrate. We will discuss the temperature and thickness dependence of the SCO complex $[Fe(H_2B(pz)_2)_2(bipy)]$ on Au(111) with a comprehensive suite of surface-sensitive spectroscopy and microscopy tools, which show that the substrate not only inhibits thermal transition of the molecular spin state, it preserves each spin state far beyond the transition temperature of free molecules [134].

4.2 Spin crossover in $[Fe(H_2B(pz)_2)_2(bipy)]$ on Au(111)

4.2.1 Experimental considerations

The $[Fe(H_2B(pz)_2)_2(bipy)]$ complex was synthesized as described previously [135]. The thermal SCO transition for the powder is determined to be in agreement with previous results [128, 135]. Molecular thin films were deposited for these studies with home built Knudsen-like molecular evaporator on a single crystal Au(111) substrate held at room temperature. Scanning tunneling microscopy was carried out in two different Omicron STM systems at 77 K and at room temperature. X-ray photoemission spectra (XPS) and angle-dependent XPS spectra were obtained using non-monochromatized Al Kα x-ray source, with a photo energy of 1486.6 eV, and a SPECS PHOIBOS 150 energy analyzer. The core level binding energies were calibrated to a gold reference, with the Au $4f_{7/2}$ core level

peak placed at 84 eV, all at room temperature. The CasaXPS software was used to analyze the x-ray photoemission core level spectra and a Shirley-type background was subtracted to obtain x-ray photoemission core level spectra peak areas. STM and XPS measurements were performed in situ immediately following the sample growth in UHV. X-ray absorption spectroscopy (XAS) measurements of $[Fe(H_2B(pz)_2)_2(bipy)]$ thin films and powder were performed at the U4B beamline at the national synchrotron light source of Brookhaven National Laboratory. The measurements were taken in the total electron yield mode of operation across the Fe $2p_{3/2}$ or L_3 edge and Fe $2p_{1/2}$ or L_2 edge. The collected spectra were normalized by the incident beam intensity, which was monitored by a Au mesh mounted upstream of the sample chamber. The Fe $L_{3,2}$ edge spectrum of an iron oxide (Fe_2O_3) film was measured as an accompaniment to the XAS data for each molecular complex sample as reference for alignment and calibration.

4.2.2 Theoretical modeling

For this complex computational work was done by the collaborators. First-principles calculations were carried out using projected augmented wave method (PAW) [136] and density functional theory (DFT) as implemented in the Vienna ab initio simulation package (VASP) [137, 138]. We used the plane-wave energy cutoff of 500 eV and the point for the Brillouin zone integration. We embedded a single $[Fe(H_2B(pz)_2)_2(bipy)]$ molecule, whose structure is taken from the experiment [139], into a 50 x 50 x 50 A^3cubic unit cell, and performed calculations for the electronic structure, particularly for the weights of unoccupied e_g and t_{2g} states. The positions of H atoms were optimized by DFT in the ground state. Gaussian smearing of 0.1 eV was adopted for the static calculations. Both HS state and LS state were obtained to confirm the ground state for the $[Fe(H_2B(pz)_2)_2(bipy)]$ molecules. To describe the electronic structure correctly, we used the rotationally invariant local den-

sity approximation (LDA) + U method [140] without LSDA exchange splitting. For the Fe based SCO complex under consideration, in the low spin state, the six 3d electrons are paired and occupy the three t_{2g}-like orbitals leaving the e_g-like orbitals empty, in the crystal field picture. In the high spin state, the e_g set is filled with two unpaired electrons while four electrons occupy the three orbitals of the t_{2g}. The usually degenerate t_{2g} and e_g subset can be split into multiple levels by deviations of molecular geometry from perfectly octahedral. Since the orbital dependent potential relies on the choice of Hubbard correlation U, the orbital occupation values are U-dependent as well. Therefore, it is of some importance to consider the Hubbard correlation U dependence of the e_g/t_{2g} ratios in both LS and HS states.

4.2.3 Structure and morphology of SCO complex layers

STM images of $[Fe(H_2B(pz)_2)_2(bipy)]$ on Au(111) are shown in figure 4.11. The molecules are very mobile across the Au surface at room temperature for sub-monolayer coverage, and move considerably faster than the typical line capture time of our STM. As a result, the well-known herringbone reconstruction of the Au(111) surface is visible, superimposed by streaks caused by diffusing adsorbate molecules (Figure 4.11(a)). The presence of molecules on this sample is, nonetheless, evident from XPS Fe 2p core level spectra. The $[Fe(H_2B(pz)_2)_2(bipy)]$ molecules condense partly into ordered double-layer islands upon cooling the sample to 77 K, as seen in figure 4.11(b), but a significant portion of the molecules remain as a surface gas or dilute fluid between the condensed islands. Higher magnification STM images, showing structural details of the condensed islands, are presented in figure 4.11(c) and 4.11(d). A structural model of this $[Fe(H_2B(pz)_2)_2(bipy)]$ double layer has been established in earlier work by Pronschinske et al. [133], based on a model proposed in a previous work by Gopakumar et al. [141] for the closely related

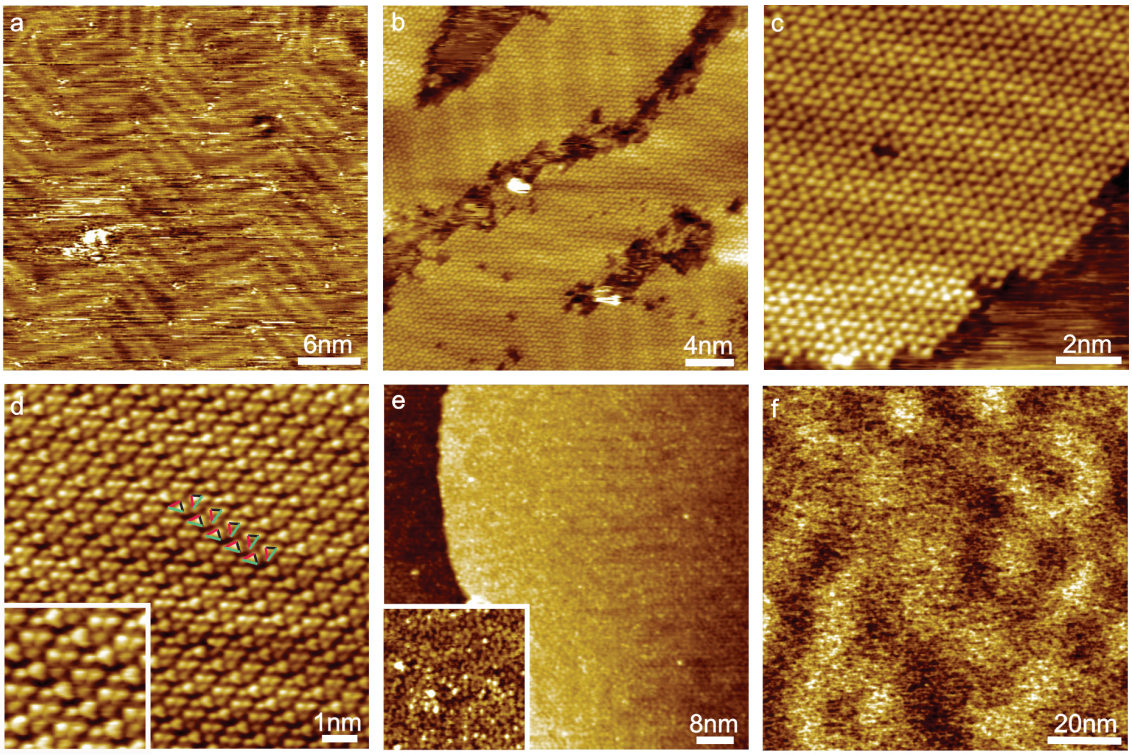

Figure 4.11: Scanning tunneling microscopy images of different $[Fe(H_2B(pz)_2)_2(bipy)]$ film thicknesses on Au(111) (a) sub-monolayer coverage at room temperature, -0.5 V, 300 pA (b) bilayer islands of $[Fe(H_2B(pz)_2)_2(bipy)]$ at 77 K, -1 V, 1 nA (c) sub-molecular resolution of bilayer islands at 77 K, -1 V, 500 pA (d) alternate rows appear different at different bias voltage, -0.2 V, 1 nA (e) 7 ± 3 monolayer thick film of $[Fe(H_2B(pz)_2)_2(bipy)]$ at room temperature, -0.8 V, 400 pA (f) non-contact AFM images of 25 ± 5 monolayer thick film of $[Fe(H_2B(pz)_2)_2(bipy)]$ at room temperature.

$[Fe(H_2B(pz)_2)_2(phen)]$ complex. Not considered in those models is that these related SCO complexes are actually noncentrosymmetric, and exist in right- and left-handed configurations, depicted in figure 4.12 for $[Fe(H_2B(pz)_2)_2(bipy)]$. Those models should lead to structural domains that are mirror images in the plane of the surface, which would be symptomatic of some chiral segregation effected by the surface acting as chiral discriminant, but such segregation was not observed in this and previous works.

This leads us to conclude that the two configurations are present in the crystal structure as a racemic mix. Each $[Fe(H_2B(pz)_2)_2(bipy)]$ molecule in the top layer appears as

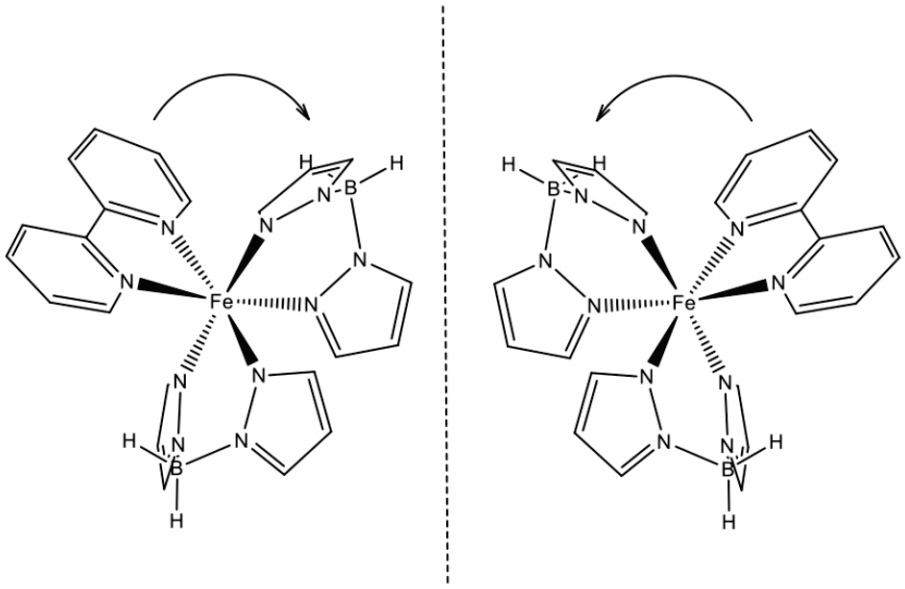

Figure 4.12: Right-handed and left-handed configurations of the non-centrosymmetric $[Fe(H_2B(pz)_2)_2(bipy)]$ complex.

a three-lobe structure, as is seen in the magnified area in figure 4.11(d). Two lobes were identified in the previous models [141, 142] as pyrazole ligands, and the third lobe is the pyridine ligand, which appears slightly darker than the pyrazole lobes in the STM images. The $[Fe(H_2B(pz)_2)_2(bipy)]$ molecules appear to be arranged along rows, where molecules in adjacent rows are seemingly rotated by 70° with respect to one another (as shown by the colored triangles in figure 4.11(d)), as the result of their stacking on top of the molecular layer underneath. Since this simple rotation leads to the same handedness and an overall isochiral domain, the possibility that adjacent rows correspond to opposite handedness should be considered, leading thus to a racemic paving of the surface. Increasing the $[Fe(H_2B(pz)_2)_2(bipy)]$ molecular coverage results in a molecular film which appears to be disordered, as seen in figure 4.11(e). This disorder builds into the condensed film for surprisingly thin films of just a few monolayers, so the exact film thickness is obscured by the degree of disorder. Yet the visibility of the Au(111) reconstruction, through the disordered

films, somewhat thicker than the molecular bilayer, suggests strongly that the film is not thicker than a few monolayers (7±3).

$[Fe(H_2B(pz)_2)_2(bipy)]$ is a dielectric [128], as is evident in the increase of binding energy for the Fe $2p_{3/2}$ core level from 706.5+0.3 eV to 710 eV [128] and to 711.5 eV [142] for thicker films as a result of either decreased substrate screening or final state charging. Conductance measurements performed on small single crystals evidence a resistivity consistently higher than 10 GΩ in the temperature range between 4 and 300 K. Consistent with this picture of $[Fe(H_2B(pz)_2)_2(bipy)]$ as a dielectric, thicker films of several nanometers thickness, could not be imaged with STM. Atomic force microscopy (AFM) does provide indications that the thicker $[Fe(H_2B(pz)_2)_2(bipy)]$ film morphology remains fairly flat so that for a nominally 25±5 nm thick films of $[Fe(H_2B(pz)_2)_2(bipy)]$, we find an RMS roughness of 0.7 nm, or about the diameter of a molecule (Figure 4.11(f)).

4.2.4 Electronic configuration

The electronic structure of the $[Fe(H_2B(pz)_2)_2(bipy)]$ films as function of their thicknesses were studied using XPS, inverse photoemission spectroscopy (IPES), and XAS. The thickness of all films can only be estimated from the intensity ratio of substrate and adsorbate XPS peak intensities, as the films appear disordered in STM and AFM (as discussed above). The XPS Fe 2p core level spectra obtained from three films of different thickness at room temperature are shown in figure 4.13. For a film of bilayer thickness, the XPS spectra exhibit broad Fe $2p_{3/2}$ and Fe $2p_{1/2}$ peaks. The broad Fe $2p_{3/2}$ and Fe $2p_{1/2}$ core level features are the result of peak splitting and the appearance of one or more shake-up satellites. The splitting of the $2p_{3/2}$ core level feature disappears with increasing $[Fe(H_2B(pz)_2)_2(bipy)]$ film thickness. Peak fitting that considers a split $2p_{3/2}$ peak and two shake-up satellites have been performed with a pre-peak, as demonstrated on the ex-

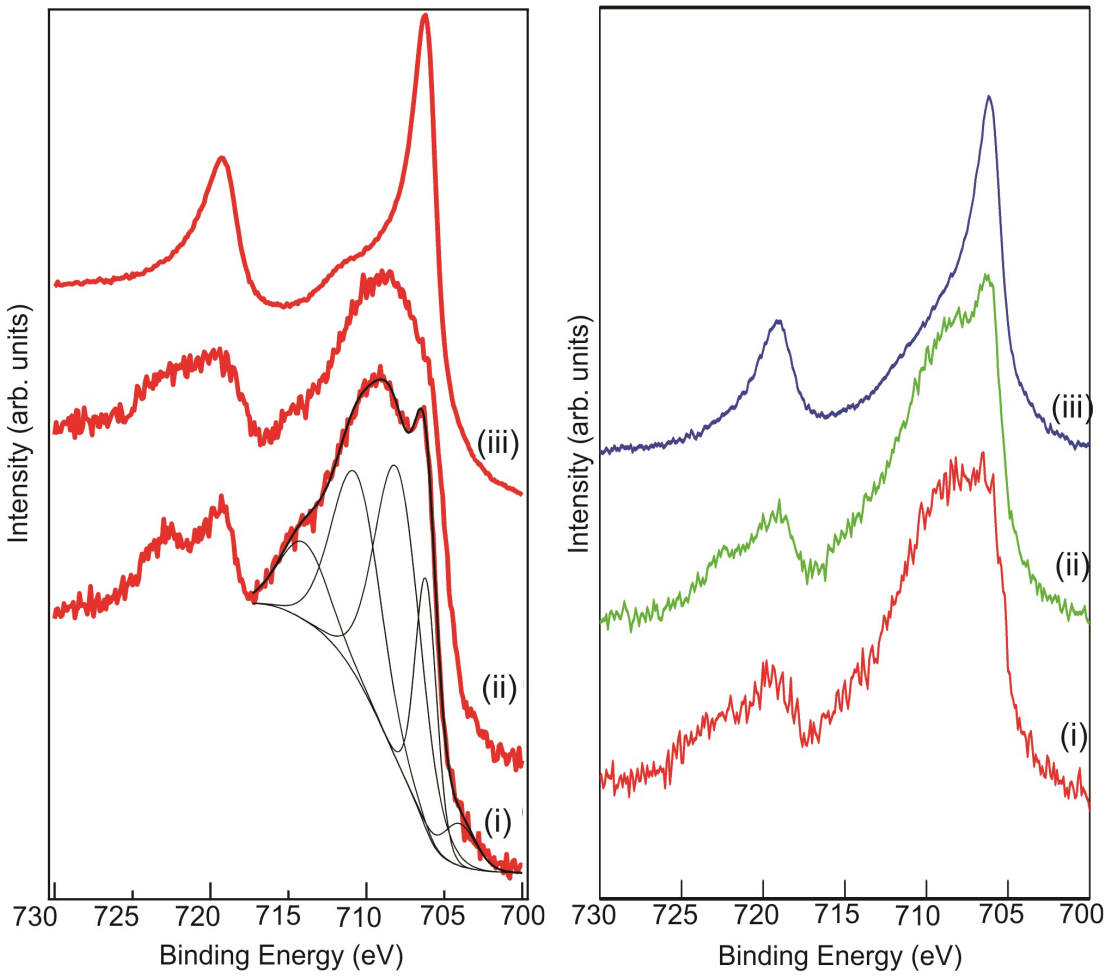

Figure 4.13: X-ray photoemission of the Fe 2p core level for increasing $[Fe(H_2B(pz)_2)_2(bipy)]$ film thicknesses on Au(111) (a)(i) a bilayer coverage at room temperature, corresponding to figure 2.5(d) (ii) 3-5 monolayer film at room temperature corresponding to Figure 2.5(e) (iii) a thicker film of 10-20 nm or more (b)angle dependent XPS for 3-5 monolayer thin film (i) 0° (ii) 30° (iii) 60°.

ample of the thin film spectra in figure 4.13(a)(i) [143–146]. Although not of high intensity for thicker 7±3 monolayers films (Figure 4.13(a)(ii)), the principal satellite features persists over a considerable range of film thickness. At even higher coverage, approximately 25±5 nm (Figure 4.13(a)(iii)), the XPS spectra are similar to those obtained from powder and thicker films, exhibiting sharp $2p_{3/2}$ and $2p_{1/2}$ peaks and comparably small shoulder features or shake-up satellites, except that the binding energy for the Fe $2p_{3/2}$ core level

remains at 706.5±0.3 eV as opposed to earlier published energies of 710 eV [128] and 711.5 eV [142]. For comparison with powder XPS spectra, powder was stamped in-situ on Au(111) substrate and the core level XPS spectra is shown in figure 4.14. The powder XPS spetcra shows the binding energy for Fe $2p_{3/2}$ at 710 eV, which indicates the dielectric nature of the molecules. Figure 4.13(b) shows angle dependent XPS spectra obtained for a film of 7±3 monolayer thickness. There is a clear increase in the intensity of peak located at 706.5 eV as compared to peak located at 708 eV, with the increasing angle between the sample and the XPS detector. Combined with the thickness dependent XPS data from figure 4.13(a), we can clearly see the substrate affecting the electronic structure of molecules at the interface.

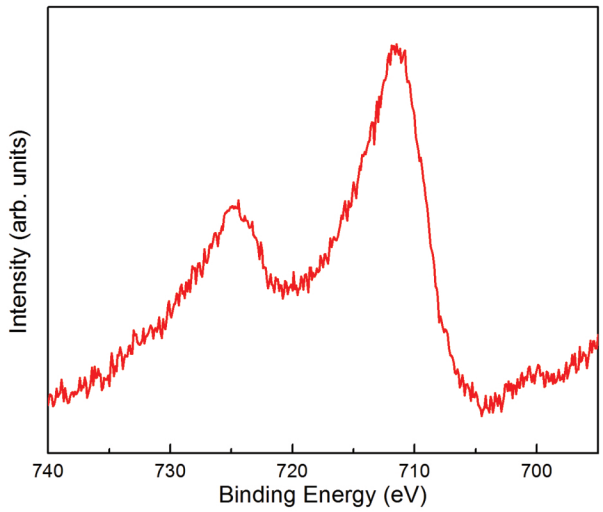

Figure 4.14: Fe 2p XPS spectra for powder stamped on Au(111).

On the other hand, the shake-up satellite peaks at higher binding energies can be due to a number of effects, such as multiplet splitting or ligand metal charge transfer. They can also be expected for iron species with unpaired spins [142,147–149]. The increase in satellite intensities was certainly seen in the high spin XPS spectra of thicker $[Fe(H_2B(pz)_2)_2(bipy)]$ films [142], but the satellite intensities here are far larger than previously reported [2,

Table 4.1: Fe 3d partial occupancy for $[Fe(H_2B(pz)_2)_2(bipy)]$, extracted from DFT (courtesy of Sai Mu).

	spin	HS State		LS State	
Correlation energy		U=4eV	U=6eV	U=4 eV	U=6eV
$d_{x^2-y^2}$	down	0.15	0.13	0.26	0.23
$d_{x^2-y^2}$	up	1	1	0.26	0.22
d_{xy}	down	0.04	0.03	0.91	0.93
d_{xy}	up	0.97	0.98	0.91	0.93
d_{yz}-d_{xz}	down	0.023	0.016	0.85	0.89
d_{yz}-d_{xz}	up	0.96	0.97	0.85	0.89
d_{z^2}	down	0.14	0.11	0.27	0.23
d_{z^2}	up	1	1	0.27	0.23
d_{yz}+d_{xz}	down	0.89	0.91	0.90	0.92
d_{yz}+d_{xz}	up	0.94	0.95	0.90	0.92
Totals		6.11	6.11	6.37	6.40

35, 142, 147, 150]. So is it possible that the strong satellite features are the result of a mixture of Fe^{3+} and Fe^{2+}, as there is some resemblance to the Fe 2p spectra in prior work [146, 151–153]? This is very unlikely: A mixture of Fe^{3+} and Fe^{2+} would require a significant change in Fe 3d occupancy, but there is no major change in total occupancy expected with the molecular spin state. We investigated the Fe 3d occupancy for all the 3d orbitals of $[Fe(H_2B(pz)_2)_2(bipy)]$ for two correlation energies, U = 4 eV and U = 6 eV, see Table 1, and find small changes in total Fe 3d occupancy with a change in spin state. The spin-resolved 3d orbital partial occupancy is sensitive to the spin state, but only

slightly sensitive to the correlation energy. However, the combined total 3d occupancy is only weakly sensitive to the spin state, and generally insensitive to the correlation energy, as summarized in Table 1.

If the Fe 2p core level satellite features are representative of unpaired spins within $[Fe(H_2B(pz)_2)_2(bipy)]$ then obviously thinner films would have a significantly greater percentage of as-deposited molecules in the high spin state than thicker films. On the other hand, the closer the proximity to the gold substrate for a molecule within the film, the greater the numbers of unpaired spin multiplets that are accessed in the photoemission final state. To bring some clarity, we have investigated the temperature dependence of the electronic structure of the films, as discussed in the following.

4.2.5 The irreversible locking of the spin state

Figure 4.15(a) shows the change in the Fe 2p XPS spectra of a bilayer thin film with temperature. Again, as in figure 4.13(a), the Fe 2p core level XPS spectra, taken immediately following molecular film growth at room temperature, show strong satellite contributions, characteristic of unpaired spins in the $[Fe(H_2B(pz)_2)_2(bipy)]$ thin film. These satellite features are suppressed in the spectra of a bilayer thin film when the film is cooled to 100 K (Figure 4.15(b)), and do not reappear if the temperature of the sample is increased back to room temperature (Figure 4.15(c)). This irreversible change of the Fe 2p peak, together with the STM images in figures 4.11(a) and (b), suggest that the disappearance of peak splitting is associated with a temperature-induced change in the stacking and possibly the conformation of the interfacial molecules during cooling. It is clearly seen from the STM images at RT and at 77 K that there is a change of the films architecture with cooling, in the form of condensation of an apparently disordered and gaseous molecular layer into a bilayer at this coverage. Likely, not only the stacking of the molecule changes at lower

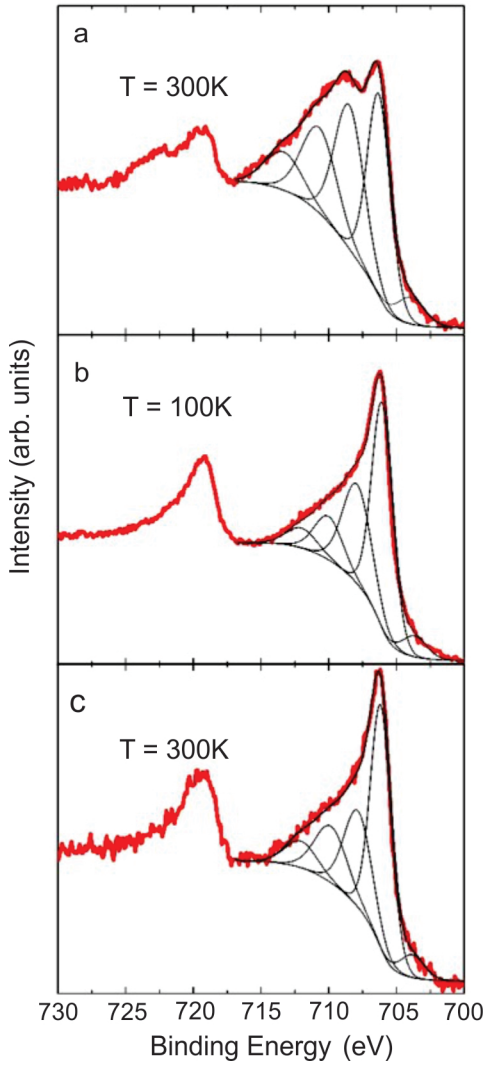

Figure 4.15: Temperature dependent XPS of a bilayer $[Fe(H_2B(pz)_2)_2(bipy)]$ thin film on Au(111) (a) Fe 2p core level spectra at room temperature for as grown film (b) Fe 2p core level spectra at 100 K (c) Fe 2p core level spectra after heating the sample back to room temperature. Temperature dependent IPES for a thin film room temperature (red) and low temperature (blue).

temperature, other more subtle changes, not visible in STM images, might occur during cooling as a result of this rearrangement of the molecules as well. This could include a distortion of the molecular ligands, and an overall change in molecule-molecule distances. It is thus to be expected that the spin state of the molecules would be affected as well.

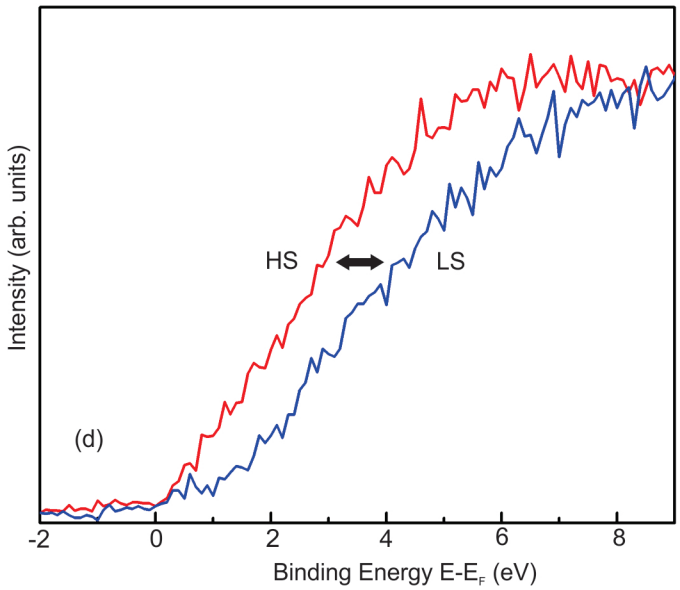

Figure 4.16: Temperature dependent IPES for a thin film room temperature (red) and low temperature (blue).

Importantly, the inverse photoemission spectra of thin SCO films show characteristic shifts in the location of the conduction band minimum away from the Fermi level upon changing from high spin to low spin states, as seen in figure 4.16, and noted already elsewhere [35, 128]. The shift in the conduction band minimum for these very thin films is less than 1 eV, which is small compared to a several eV shift as was seen for 10-25 monolayers thick $[Fe(H_2B(pz)_2)_2(bipy)]$ films on dielectric substrates [35, 128]. Does this mean coexistence of spin states in spite of the very significant reduction of the satellite feature intensities in the Fe 2p core level XPS spectra, as seen in figure 4.15? As noted above, prior work [127, 131], suggests that a conducting substrate, like Au(111), tends to pin more than 50% of several SCO complexes in the high spin state even well below the SCO transition temperature. To bring more clarity to these questions, we have utilized X-ray absorption spectroscopy.

The Fe L-edge X-ray absorption (XAS) spectra are representative of resonant state-to-state transitions of electrons from the occupied Fe 2p orbital to unoccupied 3d or-

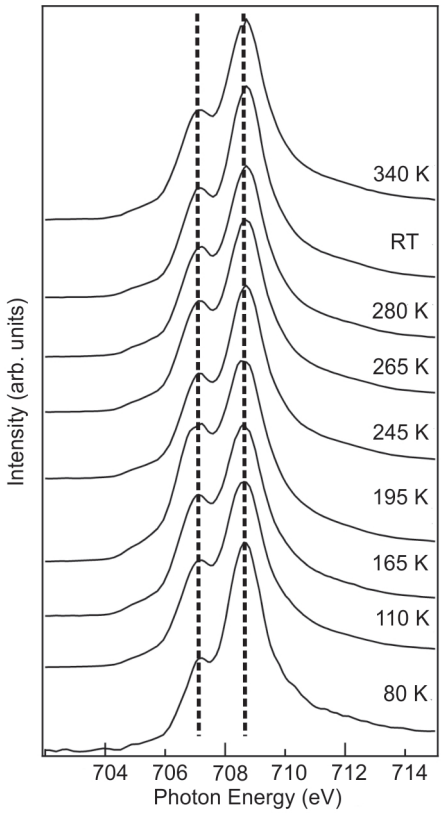

Figure 4.17: Temperature dependent X-ray absorption spectra of a bilayer $[Fe(H_2B(pz)_2)_2(bipy)]$ thin film on Au(111).

bitals. Other intra-atomic Fe transitions from 2p to 4s are of low probability, while excitations to 4p are dipole forbidden. Thus, while strong similarities between the inverse photoemission and X-ray absorption spectra are expected [35, 128] and some significant differences are expected as well. Figure 4.17 illustrates temperature-induced changes in the XAS features across the spin crossover transition temperature of 80 K to 340 K for $[Fe(H_2B(pz)_2)_2(bipy)]$. Like in prior studies [127], also the XAS spectra of the bilayer film are characteristic of a mixed spin state with significant contributions from both e_g and t_{2g} Fe weighted unoccupied molecular orbitals. The analysis of the XAS data for the $[Fe(H_2B(pz)_2)_2(bipy)]$ powder, following a procedure described in Ref. [130], provides experimental values of the e_g/t_{2g} ratios of 0.7 ± 0.2 for the high spin state and 5 to 5.9

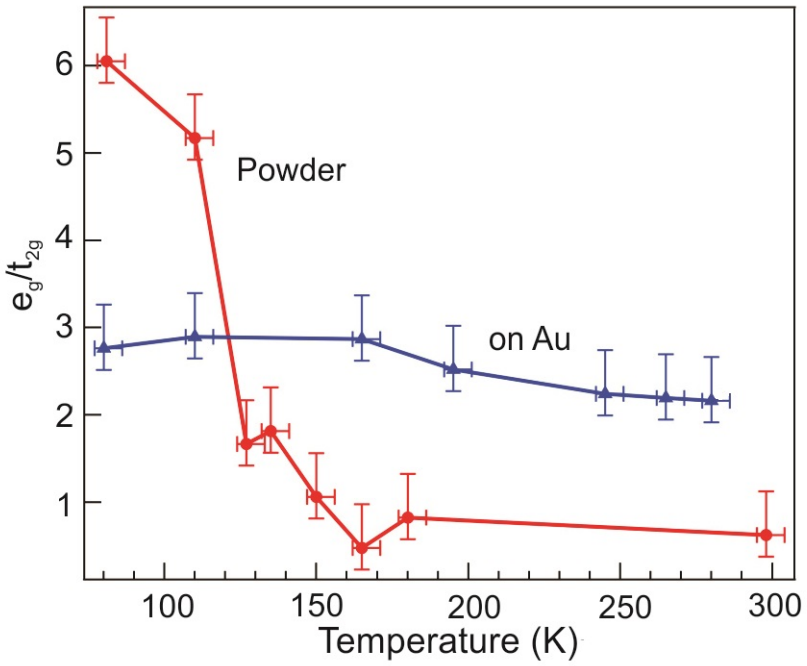

Figure 4.18: The temperature dependence of the relative empirical unoccupied e_g/t_{2g} state ratio extracted from XAS for $[Fe(H_2B(pz)_2)_2(bipy)]$ powder (red circles) and bilayer molecular films on Au(111) (blue triangles). In both cases the data is taken after cooling to below 100 K, then increasing the temperature to the value indicated.

for the low spin state, as seen in Figure 4.18. These values are consistent with expectations from theory [130]. The increased sensitivity of the e_g/t_{2g} ratios to the choice of U in the low spin state, lies in the fact that t_{2g}-like orbitals remain mostly occupied in the low spin state whereas e_g is unoccupied. The empirical e_g/t_{2g} ratio extracted from the XAS spectra, is particularly sensitive to a modest variation of t_{2g} occupation. By stark contrast, the e_g/t_{2g} ratios of the same molecules as a few monolayers thin film on Au(111) clearly shows that the ratio of high spin to low spin state varies only slightly with temperature. On this basis, using the XAS powder derived empirical values and applying these values to the XAS thin films, our data suggest that the proportion of molecules in the high spin state, at low temperatures, is 59$\pm$6% compared to 71$\pm$6% in the high spin state at elevated

temperatures. This is nearly identical to the results obtained for submonolayer films on Au(111) [127]. Nonetheless, this seems to contradict the results of figure 4.15 where the absence of strong contributions from satellite features suggests that the ultrathin molecular film is characteristic of $[Fe(H_2B(pz)_2)_2(bipy)]$ with paired, not unpaired, spins once cooled to low temperatures.

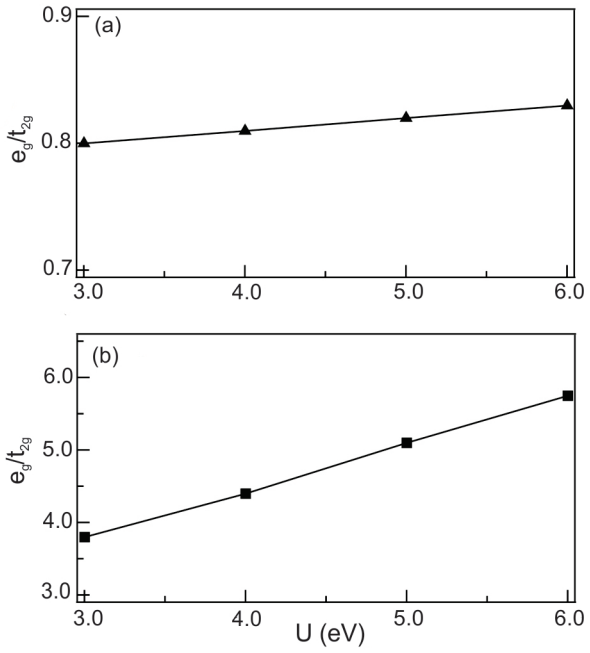

Figure 4.19: The e_g/t_{2g} ratios in both HS (a) and LS (b) states were evaluated at different values of the correlation energy U, using density functional theory (see text) (courtesy of Sai Mu).

An important consideration in this discussion is that the e_g/t_{2g} ratio in the high spin state is quite insensitive to the choice of the Hubbard U parameter, but in the low spin state the $e_g/t_{2}g$ ratio varies from 3.8 to 5.8 for 3 eV $\leq$ U $\leq$ 6 eV, as summarized in figure 4.19. This allows for only two possible conclusions: either the gold substrate stabilizes the molecular SCO thin films in a mixed spin state, which is dominated by the high spin state (59$\pm$6% to 71$\pm$6%), or the gold substrate alters the applicable correlation energy. But if the presence

of a Au substrate indeed changes the correlation energy U, say reducing it by a factor of 2 from U=6 eV to U=3 eV, then the XAS spectra of our bilayer thin $[Fe(H_2B(pz)_2)_2(bipy)]$ films on Au(111) should be representative of a lower fraction of molecules in the high spin state at low temperatures, as little as $32 \pm 6\%$. Meanwhile the fraction of molecules in the high spin state at higher temperatures would have to be reduced to $51 \pm 6\%$, much lower than if the correlation energy were higher ($71 \pm 6\%$ if U=6 eV).

4.3 Conclusion

To conclude, the interaction of the $[Fe(H_2B(pz)_2)_2(bipy)]$ spin crossover complex with Au(111) substrates inhibits the spin crossover transition of the molecules so that there is a relatively fixed ensemble of molecules in both high spin and low spin states preserved over a wide temperature range, including the temperature range across the spin crossover transition temperature of powdered samples. This locking of the spin states does not occur upon adsorption, but rather after cooling to low temperature. It is most likely the result of a conformational change of the interfacial molecules, whereas the Hubbard correlation energy between the molecules is not affected by the substrate. Molecules in thicker films, above a film thickness > 20 molecular layers, can however reversibly undergo spin crossover and are not impeded by interfacial effects, and this change in spin state gives rise to a characteristic shift of the conduction band edge. This study contributes to the current discussion of spin crossover complexes as emerging candidate material for organic spintronics applications by helping establish the role of interfaces in 2D layers of $[Fe(H_2B(pz)_2)_2(bipy)]$ on Au(111) substrate.

4.4 Future trends

Combined with the studies of Zhang et. al. [35] where it was demonstrated that the electric field from the polar substrate can be used to manipulate the spin state of these molecules, we have synthesized solution mixture of [Fe(H_2B(pz)$_2$)$_2$(bipy)] and parent zwitterion molecules. The zwitterion molecules have a dipole moment of 10 D. Our preliminary studies show that in the mixture most of the spin crossover molecules have low spin state in the temperature range of 50 K to 300 K (Figure 4.20). These results provide a direction for future where electric field from a dipolar molecule can be used to manipulate the magnetic properties of spin crossover complexes in thin films.

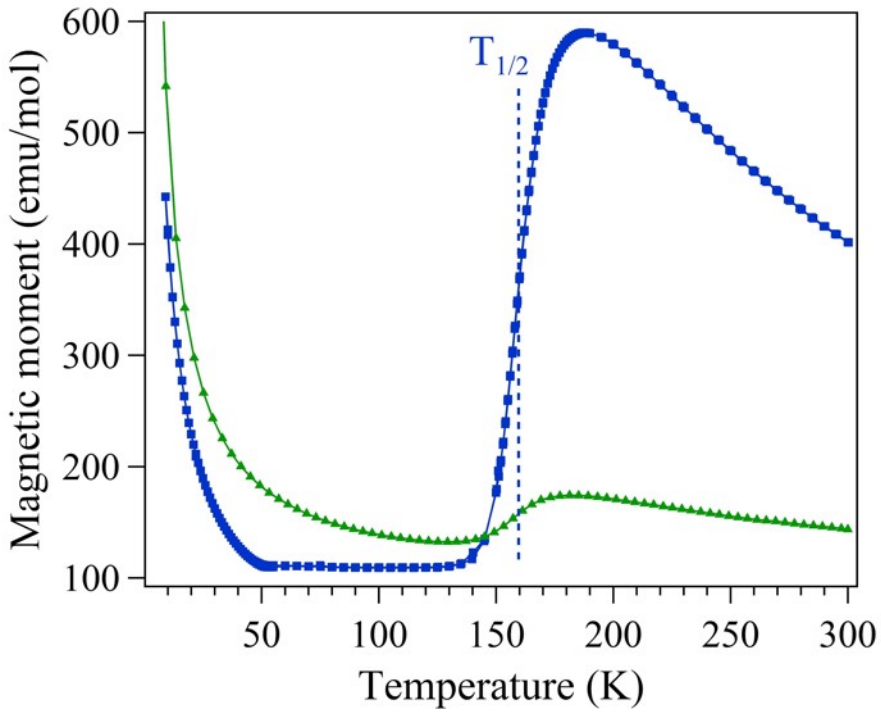

Figure 4.20: The SQUID data for pure [Fe(H_2B(pz)$_2$)$_2$(bipy)] powder (blue) and mixture of parent zwitterion and [Fe(H_2B(pz)$_2$)$_2$(bipy)].

Chapter 5

Self-assembled boron based semiconductors

Two dimensional materials, such as graphene, hexagonal boron (h-BN) nitride, with sp^2 hybridization exhibit unique electronic and mechanical properties compared to bulk materials. Graphene is a zero band gap semiconductor, while h-BN is a wide band gap insulator. The question arises whether a 2D material can be designed that has a band gap intermediate between graphene and h-BN, and consisting of B, N and C. The BCN ternary phase diagram shows indeed the possibility to form layered compounds such as, stable BCN, BC_2N and BC_4N [154]. Theoretical studies have also predicted the possibility of two dimensional ternary BCN compounds with properties that depend on the stoichiometry as well as the arrangement of B, C and N atoms [155–159]. Various BCN compounds have been synthesized, for instance by templated growth of h-BN from graphene [160], chemical of doping of graphene/carbon nanotubes [161–163] with B and N, stacking graphene and h-BN [164] or co-deposition of precursors containing carbon, boron and nitrogen [165–173]. However, these experimental studies have either resulted in the formation of BCN materials with inhomogeneous stoichiometry [166–173], or phase segregated graphene and h-BN [165,174].

Herein, we discuss the synthesis of the first 2D hexagonal-BCN structure on Ir(111). The key to success is a cyclic precursor molecule Bis-BN cyclohexane ($B_2N_2C_2H_{12}$) which was synthesizd for this study [175]. Using such a precursor molecule inhibits the phase segregation of C and BN, and maintain the homogenous stoichiometry in our two dimensional material. Chen et al., show that in the presence of Pd/C and Ru catalysts held at elevated temperatures, these molecules release hydrogen and bond covalently to form two cage compounds [175]. Therefore, it is reasonable to expect that the same dehydrogenation will occur upon deposition of these molecules on a transition metal surface so that a 2D h-BCN network can form. Our STM images show evidence of extended 2D BCN monolayers network on Ir(111) substrate. The formation of BCN type structure is also confirmed by core level X-ray photoemission spectroscopy. These experimental results are supported by DFT calculations, which show formation of corrugated h-BCN on Ir(111) and resultant Moire superstructure.

5.1 Sample preparation

To investigate the self-assembly of bis-BN cyclohexane, sub-monolayer films were were synthesized on Au(111), Cu(111) and Ir(111). The BCN molecules are stable upto 150 °C in ambient conditions [175]. Under UHV conditions molecules sublimate at room temperature. Molecular powder was evaporated from a quartz crucible inside a Knudsen-like homebuilt evaporator. At UHV pressures molecules started to sublime already with the crucible at room temperature, whereas increased time increased the flux. Exposure of the substrate to the molecules was thus controlled with a gate valve that separated the evaporator and UHV chamber. Au(111), Cu(111) and Ir(111) substrates were cleaned using repeated cycles of Ar+ ion sputtering. After sputtering, the Au(111) and Cu(111) were annealed to 650 °C and Ir(111) substrate was annealed to 1400 °C using e-beam heating.

Various samples were prepared by varying the temperature of the substrates using e-beam heating during molecular deposition. The procedure for XPS data acquisition and analysis is described in previous chapter. The LEED was performed on as grown samples using Omicron Spectaleed.

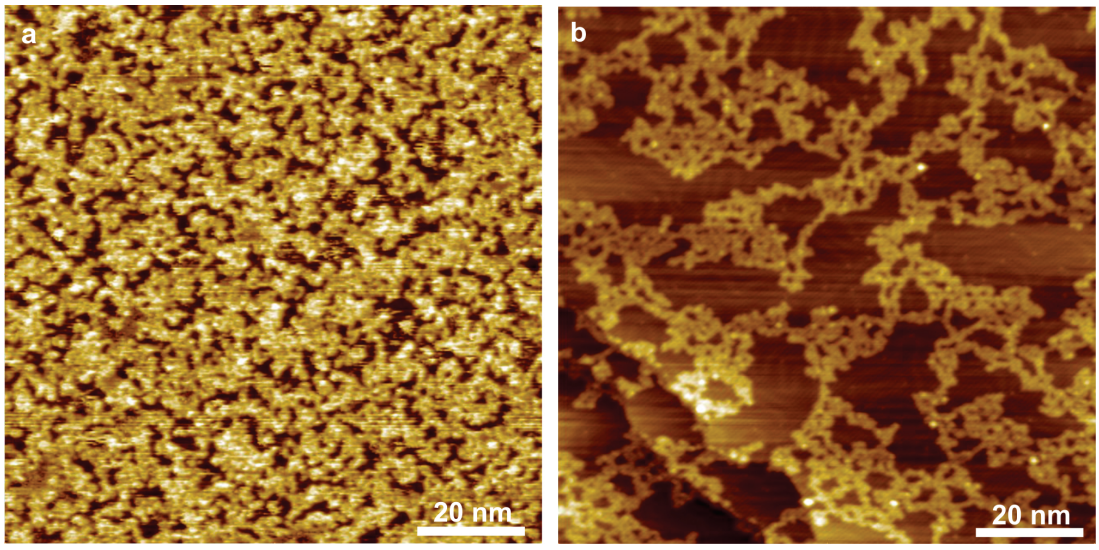

Figure 5.1: STM images for bis-BN cyclohexane on Au(111) (a) monolayer film deposited at room temperature (b) molecular network after annealing to 300 °C.

5.2 Bis-BN cyclohexane on Au(111) and Cu(111)

Figure 5.1(a) shows the STM image of monolayer film deposited at Au(111) substrate held at room temperature. The film does not show any ordering of the molecules. Also, the subsequent annealing to 300 °C does not promote any ordering of the molecules. The STM images taken after annealing to 300 °C (Figure 5.1b), shows that a large fraction of molecules desorb and remaining molecules on the surface form disordered network where they appear to be linked. The deterioration of the atomic steps of the substrate suggest that Au atoms are reacting with the molecules to form this disordered network. The reaction

between the molecules and substrate atoms is confirmed when molecules are deposited on Au(111) substrate held at elevated temperatures.

Since molecules appear to link together after annealing to 300 °C, the next sample was synthesized by depositing molecules at Au(111) substrate held at elevated temperature. Figure 5.2(a)-(b) show the STM image of samples grown at Au(111) held at 350 °C and 650 °C respectively. It is clear that the molecules accumulate near the substrate atomic step edges. The jagged step edges confirm that the substrate atoms react with the molecules.

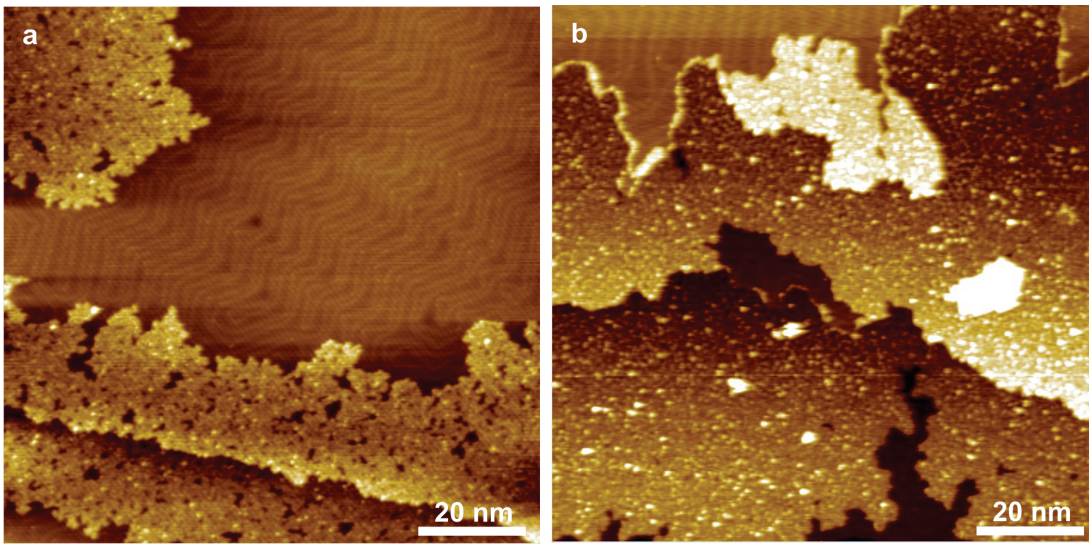

Figure 5.2: STM images for bis-BN cyclohexane deposited on Au(111) (a) at 350 ° (b) at 650 °C.

Similar results are obtained when the molecules are deposited on Cu(111) substrate. The molecules form disordered film when the substrate is held at room temperature during deposition (Figure 5.3(a)). However, very small fraction of the molecules stick to the substrate held at 650 °C during deposition and these molecules react with the surface adatoms (Figure 5.3(b)). The holes in the substrate surface and jagged step edges indicate that the molecules react with the substrate.

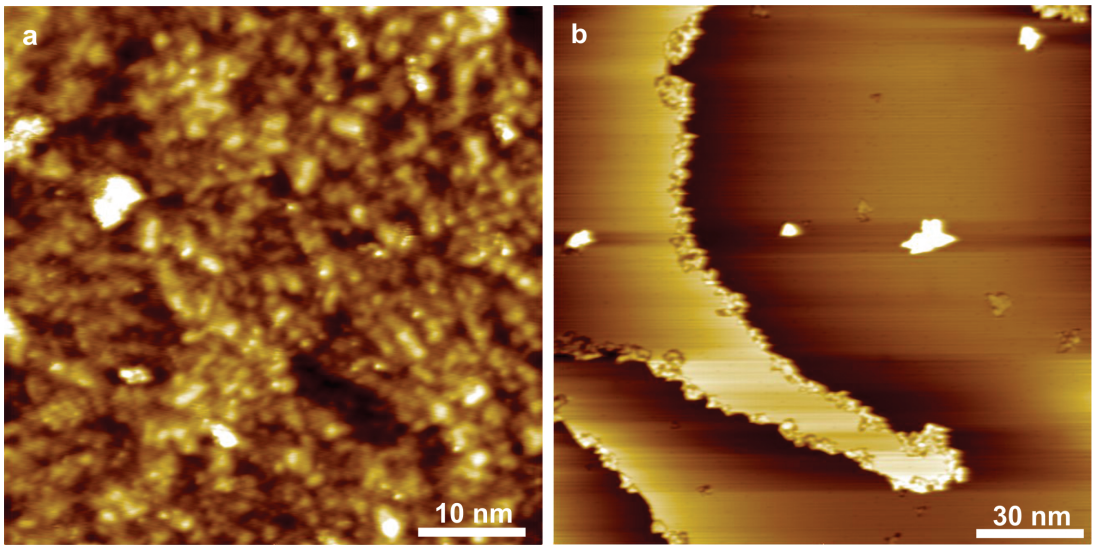

Figure 5.3: Bis-BN cyclohexane samples grown on Cu(111) substrate held at (a) room temperature (b) 650 °C

5.3 h-BCN Network on Ir(111)

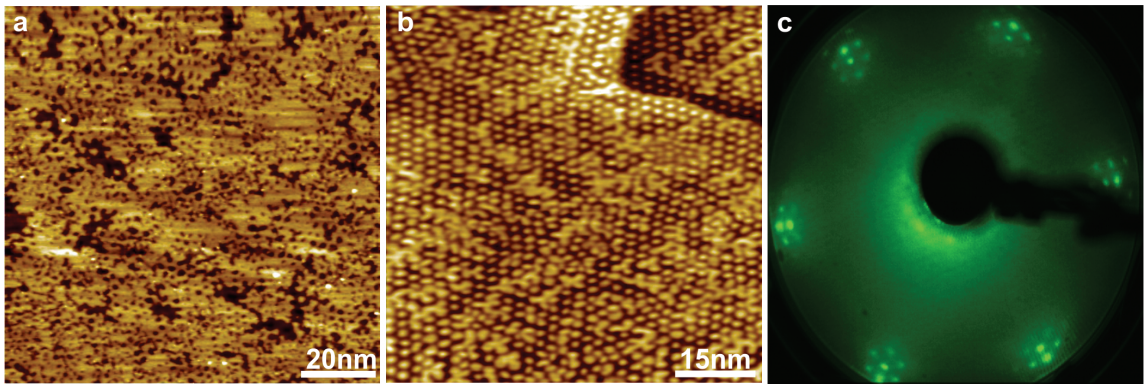

Figure 5.4: Scanning tunneling microscopy images of single layer BCN on Ir(111), grown at substrate temperatures of 25 °C (a) and at 980 °C (b). The bias voltages were -1 and + 4 V in (a) and (b), respectively. (c) Low energy electron diffraction image of the sample in (b) with E_{beam} = 71.1 eV.

Scanning tunneling microscopy (STM) images of two samples, one grown at a substrate temperature of 25 °C and the other at 980 °C, are shown in figures 5.4(a) and 5.4(b). When

grown at room temperature, the layer is discontinuous, exhibiting coexisting areas of what appears to be a porous honeycomb-like phase, and a second phase that cannot be resolved. The contrast in this STM image is dependent on the bias voltage used, which will be discussed later and which can be used to identify the structural phase of the films. Increasing the substrate temperature during exposure to the precursor molecules improved the ordering in the layer, meaning that large areas of regular and periodic corrugation patterns begin to dominate and structural disruptions become less common. We found the highest-quality films when grown at a substrate temperature of 980 °C, as shown in figure 5.4(b), wherein the observed bright lobes arrange into an ordered, hexagonal pattern. This is seen most clearly in the higher magnification images in figure 5.5. The center-to-center distance between the bright lobes was measured to be 2.6 $\pm$ 0.1 nm, and the apparent height of the lobes in this image is 0.13 $\pm$ 0.01 nm (see the line profile in Figure 5.5(d)). However, this apparent height, in the STM imaging, is voltage-dependent, as evident from figure 5.5, and discussed further below. A low-energy electron diffraction (LEED) pattern is shown in figure 5.4(c). The diffraction image exhibits a characteristic superstructure pattern, which is analogous to earlier reported LEED results obtained on epitaxial h-BN as well as graphene monolayers [176, 177]. The main spots arise from the Ir(111) surface layer, whereas the satellite spots reflect the periodicity of the moire pattern formed by the BCN layer with the Ir(111).

The bias voltage dependence of the appearance of the layers is evident from figure 5.5. The same sample areas are shown, imaged with select positive and negative bias voltages applied to the sample. Clearly, the contrast of the images is inverted when going from large positive to small positive and negative bias voltages. At +2 V bias voltage, the boundaries between dark and bright contrast areas become particularly visible, resulting in ring-like features in the images.

It is very reasonable to conclude from the STM images, with support from the LEED

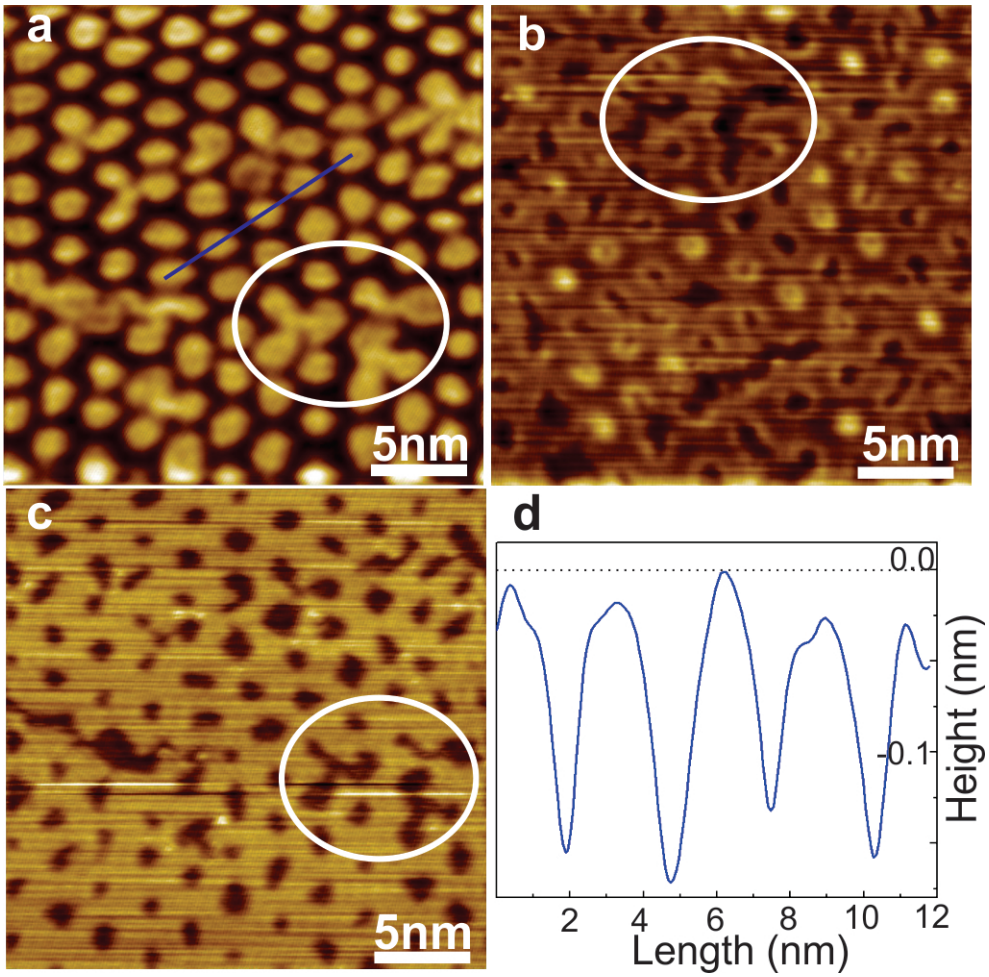

Figure 5.5: Scanning tunneling microscopy images for the network in Figure 5.4(b) as function of bias voltage (a) +4 V (b) +2 V (c) -1 V (d) a line profile along the blue line in (a).

results, that a continuous, epitaxial BCN monolayer has formed from the precursor bis-BN cyclohexane, where the lattice mismatch between the film and the substrate give rise to a moire pattern and buckling that is visible as a long-range film corrugation in the STM images. As seen in figure 5.4(a), the fact that these layers begin to form, at least partially at or near room temperature, lends strong support to the conclusion that the cyclic $B_2C_2N_2$ ring of the precursor molecules remains intact on the surface, and that dehydrogenation, thermally activated or catalytically activated by the surface, allows for covalent bond for-

mation between those rings. A plausible network, where the molecular models illustrated in figure 5.6(a) come together to form the BCN_v1 network in figure 5.6(b), leaves the B, N, and C constituents of the network in one of the configurations B_2NC, BN_2C, or BNC_2. This is, of course, testable by measuring chemical shifts of binding energies of B, C and N core electrons by X-ray photoelectron spectroscopy (XPS).

The B 1s and N 1s core level XPS spectra, obtained on a BCN sheet imaged in the STM (Figure 5.4(b)), are shown in figure 5.7. Due to the overlap between the Ir substrate 3d peak with the C 1s peak of the BCN layer, we are unable to evaluate the chemical state of C in this layer. For reference, the core level spectra for C 1s measured on this sample is shown in the figure 5.8. The B 1s and N 1s FWHM peak widths are determined to be 2.5 eV, which is considerably larger than reported values of the FWHM for h-BN that range between 1.1 eV to 1.7 eV, [178] and far beyond our instrumental energy induced feature width of 0.5 eV. As is commonly found, such peak broadening can be the result of the superposition of multiple peaks or lifetime broadening. As h-BCN is a band gap material, photoemission lifetime broadening will be suppressed, so multiple core levels due to different chemical environments must be invoked. Multiple core level photoemission features have been observed due to the moire rumpling of graphene [179] and while different core level photoemissions are possible due to differences in the screening from the substrate, this would only occur if the interaction with the substrate is very strong (as in the case of graphene grown on Rh(111) and Ru(0001), but not when the interaction is weak, as in the case of graphene on Ir(111) [179]. While rumpling of the h-BCN layer occurs, this is not the cause of the multiple core level features seen here. The rumpling explanation would mean only 2 such components for each core level, and components with similar line shapes and a fairly small separation [179]. This is not the case here.

With this in mind, the multiple XPS core level components are expected as B has two different chemical environments, BNC_2 or BN_2C, whereas the N is in the BNC_2 or B_2NC

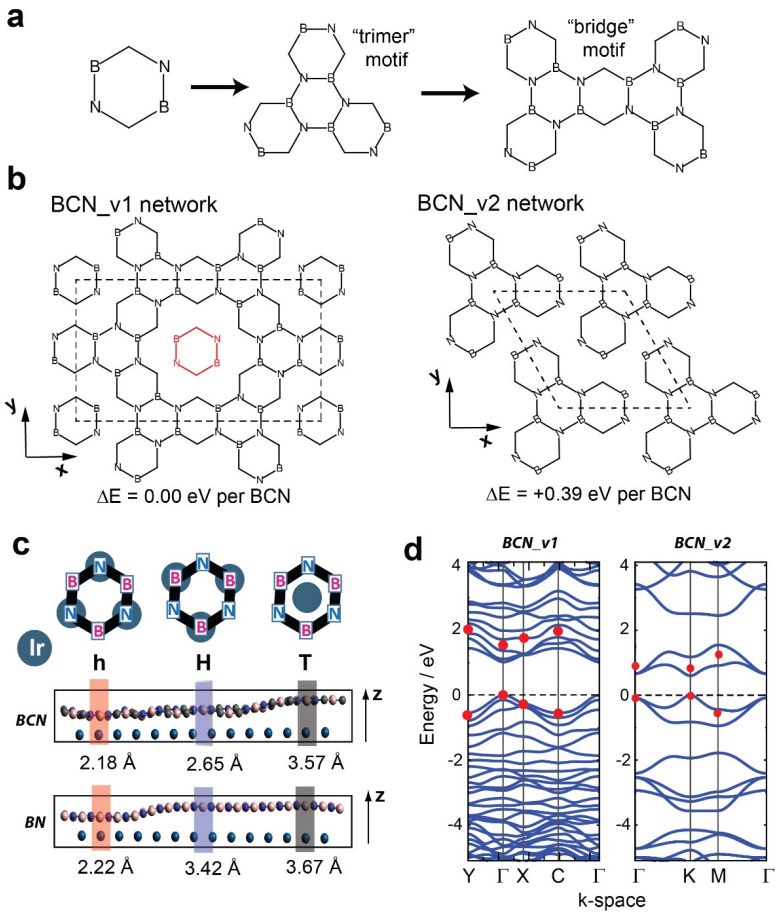

Figure 5.6: (a) A schematic representation of how the precursor molecule comes together to form borazine-like fragments, the most stable building blocks of extended BCN sheets. BCN models which preserve the B-C, B-N, and C-N connectivity in the precursor molecules are shown in (b); the latter structure, BCN_v2, is the more stable one. (c) The corrugation of BCN_v2 and BN when each system is modelled over a two-layer Ir(111) slab. The corrugation follows a strip where the B3N3 fragments align as shown over the h, H, and T sites; the number below each site shows the elevation of B_3N_3 with respect to the top layer of the surface. (d) The electronic band structures of flat BCN sheets in the gas phase, computed with the PBE-D3 functional; the Fermi energy is set to zero in each plot. The red dots show the computed band energies of the valence and conduction bands with the hybrid HSE06 functional.

environment. A multi-peak fit was performed on the B 1s peak in figure 5.7(a), which considers two main peaks, along with one shoulder peak at a lower binding energy. The two main peaks reflect the coexistence of B in two different chemical environments. The

best fit to the experimental data yields the two main peaks at binding energies of 188.9 eV and 189.6 eV, respectively. A comparison with published peak positions for the B in h-BN and in $BC_{3.4}$ [180] allows us to assign the higher binding energy peak to B in the BN_2C binding configuration, and the lower binding energy peak to B in the BNC_2 configuration. The rationale is that C is less electronegative than N so that a shift of the B 1s peak to lower binding energies is expected if the C concentration in the local environment of B is increased. The shoulder peak at lower energy is included in the fit to address the observed feature in the experimental data. While this additional peak at 187.4 eV binding energy could be the result of interaction of the adlayer of B atoms with the Ir substrate, analogous to what has been reported for other related systems, [181, 182] this additional B 1s component in x-ray core level photoemission could also be the result of imperfections where the coordination with nitrogen is reduced [183, 184], and thus explain why no corresponding additional core level component is seen in the N 1s spectra.

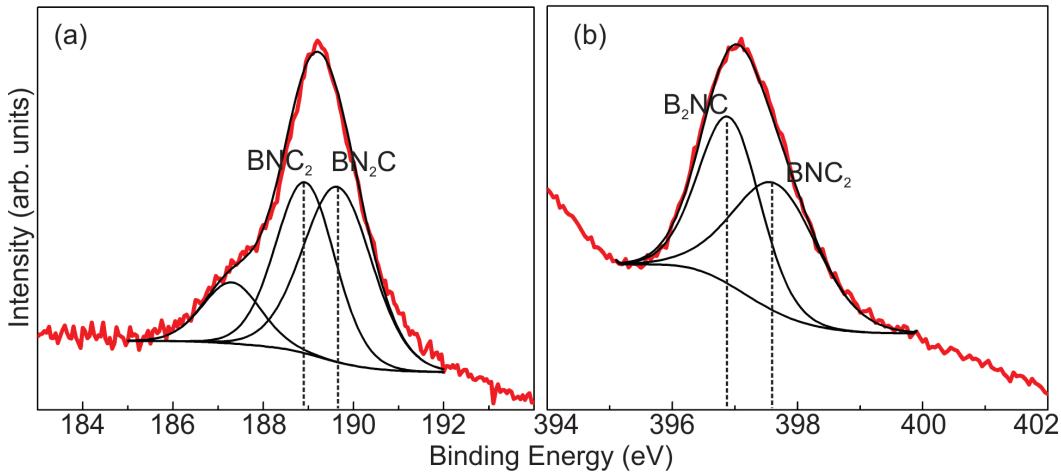

Figure 5.7: Core level XPS for sample grown at 980 °C (a) boron 1s (b) nitrogen 1s.

Likewise, the N 1s XPS spectra has also been fitted with two peaks, and a best fit to the data was obtained with main peak positions at energies of 396.9eV and 397.7 eV. Again, the peak at the lower binding energy is assigned to N in the B_2NC configuration and the

peak at higher binding energy is assigned to N in the BNC_2 bonding configuration. This assignment is based on the same rationale from above that an increase of C in a BNC local environment will increase the N 1s binding energy, since C is more electronegative than B. Moreover, the differences in binding energy for the components contributing to the N 1s core level and the B 1s core level are much larger than expected from simple rumpling of the h-CBN layer [180], so they must have their origin in local bond order.

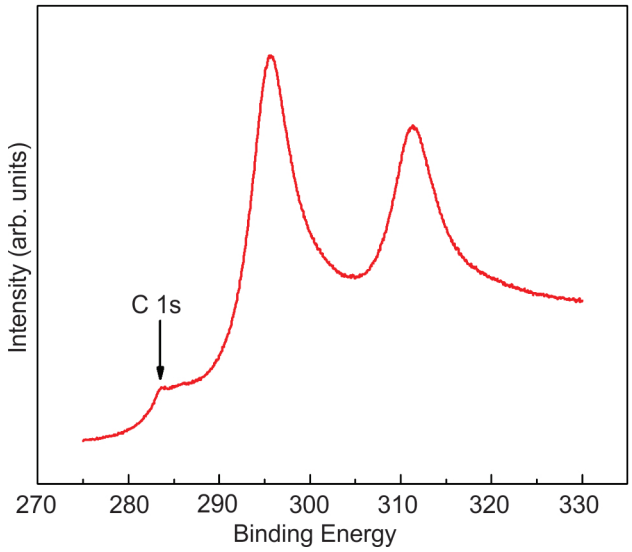

Figure 5.8: Core level XPS for carbon 1s for sample grown at 980 °C.

The XPS data unambiguously confirm that the B, C and N atoms in the film are in chemical environments consistent with our proposed BCN network. Additional insight in the film structure and morphology was achieved through first-principles calculations. Our proposed models for a homogeneous BCN film are shown in figure 5.6. The models are interesting because they both represent an extended sheet into which the molecular building blocks could easily assemble after de-hydrogenation. In other words, in both cases the extended structures can form from the precursor molecule without breaking any of the X-X bonds where X=B, C, or N. The models are built by focusing on the propensity of the precursor molecules to form intermolecular B-N bonds. The lowest-energy de-hydrogenated

trimer that we were able to find of the precursor molecule, forms a borazine-like fragment in the center, as illustrated in figure 5.6(a); in fact, it is the only trimer that was computed to be exothermic with respect to dehydrogenation of the precursor molecules in the gas-phase. The P2/m-symmetry BCN_v1 model, as illustrated in figure 5.6(b), forms a porous network where the $C_2B_2N_2$ rings from the precursor molecules are stitched together with favorable B_3N_3 contacts; each pore is then filled with another $C_2B_2N_2$ ring. The D3-symmetry BCN_v2 model, also illustrated in figure 5.6(b), is built instead from a direct tiling of the most stable $C_2B_2N_2$ trimers. Although the higher-symmetry BCN_v2 model allows for every heterocycle from the precursor molecules to participate in an intermolecular B-N bond, it is 0.4 eV per BCN unit less stable than BCN_v1 in the gas phase, largely because it forms fewer B-N bonds. We therefore consider the most likely model, based on its lower electronic energy and larger number of B-N bonds, to be BCN_v1.

We find that the BCN sheet itself is substantially less stable than isolated BN and graphite; we compute the energy of reaction for BN+graphite $->$ BCN_v1 to be +1.28 eV per BCN unit. The BCN sheet models are metastable on the B/C/N gas phase potential energy surface. It has been show that the synthesis of 2D materials whose formation energies are larger than 200 meV/atom typically require a stabilizing substrate [185]. However, because the intermolecular bonds between the B, C and N atoms are strong and the barriers to break them are typically large, it may be possible that the BCN sheets discussed herein can be obtained as free-standing or suspended structures.

Simple models of single BN and BCN_v2 sheets were also optimized over two-layer Ir(111) simulation slabs, an overhead view of the BCN model is shown in figure 5.6(c). The reason why the BCN_v2 sheet was considered instead of the BCN_v1 model is that the unit cell of the latter is substantially larger than that of the former, so it would be prohibitively computationally expensive to optimize its geometry on the Ir(111) surface. Like BN, the BCN_v2 sheet is found to corrugate by roughly 1.5 A over the slab, this is

similar to what has been in found in other computational studies of BN adsorbed over an Ir(111) slab [186]. The lowest-energy site we considered of the BCN sheet places some of the borazine (B_6N_6) fragments within the sheet directly over the T, H, and h sites which are labelled in figure 5.6(c). These sites correspond either to where the N or B atoms in the B_6N_6 fragment lie directly over one of the surface Ir atoms, like at H and h, or where the center of the B_6N_6 fragment lies directly above a surface Ir atom, the T site. The B_6N_6 fragments which lie over each site have different elevations over the surface for both BN and BCN, but the h site is held closer to the surface on BCN. This correlates with a slightly stronger binding energy for the BCN sheet than for the BN sheet, we compute the binding energy of the BN sheet to be -0.24 eV per $(BN)^{1.5}$ unit and that of the BCN sheet to be -0.46 eV per BCN unit.

Before extensive measurements of the band structure of the h-BCN networks become available it is worth using our computational model to make some predictions. In figure 5.6(d), we show the computed band structure of pristine (flat) sheets of both BCN models in the gas phase. The computed band gaps with the HSE06 density functional, 1.50 eV for BCN_v1 and 0.85 eV for BCN_v2, are much smaller than for BN, which we compute to be 5.75 eV. We note that, shown in figure 5.9, the band gap of BCN_v1 is dependent on the orientation of the molecule in the pores; orientations that differ from that shown in figure 5.6(b) were found to be only slightly less stable and have band gaps as low as 0.60 eV. This is not unexpected: first-principles calculations on $(BN)_n(C_2)_m$ (n,m = 1,2,...) have shown that band gaps for various nearly isoenergetic networks can vary by up to 1.0 eV [158]. Scrutiny of the atomic contributions to the electronic structure confirms that the valence and conduction bands in both h-BCN models correspond with π-symmetry electronic states spread out over the simulation cell. The band structures thus confirm that a single-layer BCN sheet has a direct band gap between the valence and conduction bands that have p-character, which may make it a useful material for many electronic applications.

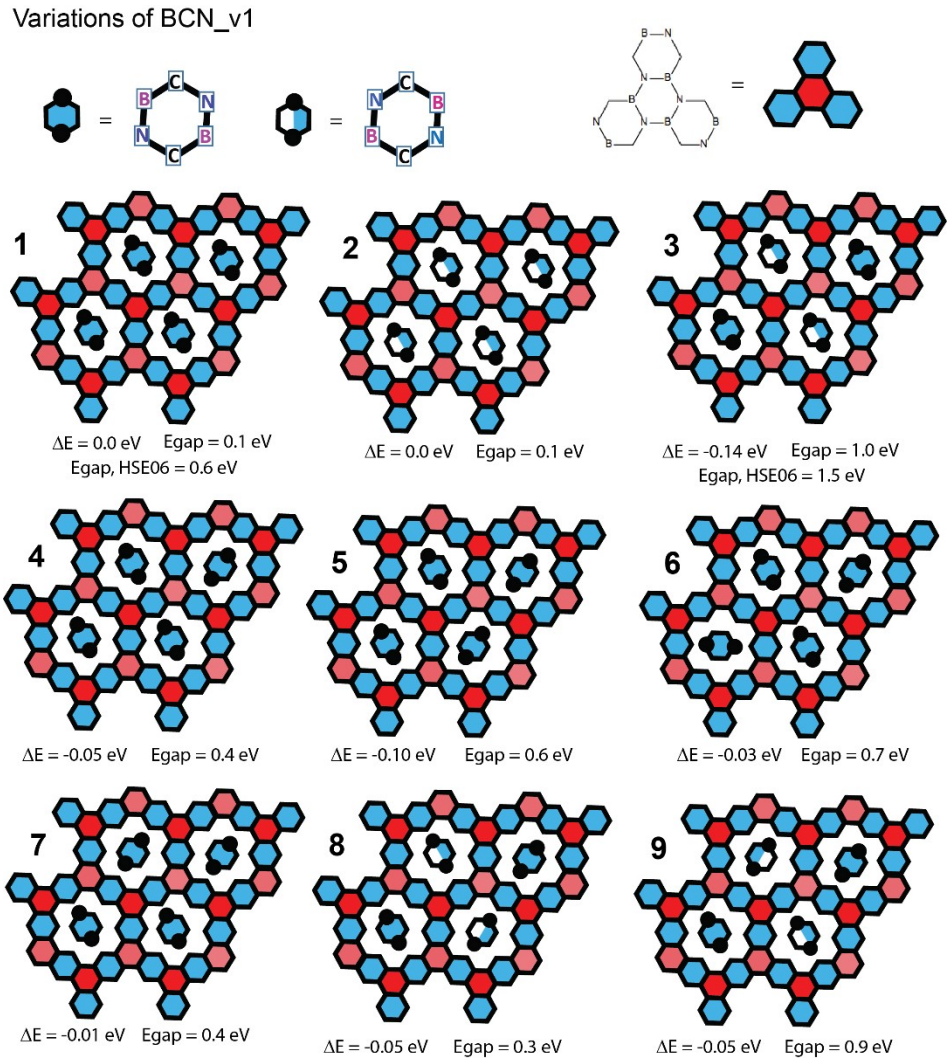

Figure 5.9: Relative electronic energies and computed band gaps of different versions of the BCN_v1 network. The networks differ in how the $B_2C_2N_2$ cycles in the center of the pores are arranged.

Our experimental results show remarkable similarities between BCN, h-BN, [160, 187, 188] and graphene monolayers deposited on various transition metal substrates [176].[34] For example, the layer corrugation is analogous to reported corrugations for graphene and h-BN,citeAlpha2008, PhysRevB.89.235429, Andrii2007 and the LEED superstructure as well as the observed voltage-dependent contrast were also observed for both graphene and h-BN, respectively. Combined with our experimental evidence, especially the XPS data,

the computational proof of structural stability, and the emergence of the experimentally observed corrugation upon structure optimization on an Ir(111) slab, we conclude with reasonable certainty that the present system is the first reported 2D graphenic BCN sheet with homogenous stoichiometry. The key to success was appropriately designed precursor molecules. The significance of this study is in the identification of a third single layer material that is composed of boron, nitrogen and carbon. Based on the predicted electronic band structure, especially a direct electronic band gap that is intermediate to those of the zero-band gap semiconductor graphene and the insulating h-BN, it can be expected that the h-BCN layers are potentially exciting new candidates for 2D electronic materials.

5.4 Electron induced crosslinking in m-carborane-9-thiol

Boron carbide represents a new class of materials [189–196] and specifically, boron carbide thin film diodes and devices have begun to attract attention as potentially highly efficient solid state neutron detectors [196]. This interest has been spurred on because ^{10}B has a high cross section (approximately 3800 barns) for neutrons at lower energies (25 meV), thus enabling ultrasensitive ultracompact neutron detectors, but also neutron-absorbing coatings for sensitive equipment in harsh environments, such as satellites. Of practical importance for any device application is the fact that boron carbides can be n- and p-type semiconductors, as well as insulators, if doped appropriately with hetero atoms.

Researchers at UNL have had considerable success in developing semiconducting boron carbide for solid state neutron detectors [197–201]. Highlights that demonstrate the huge potential of materials synthesis from carborane precursor molecules include the demonstration of the first boron carbide heterojunction diode [202, 203], the first boron carbide transistor, the first boron carbide homojunction [197, 201], the first boron carbide Esaki tunnel diode [204], the first heteroisomeric diode [189], and the first all boron carbide het-

erojunction diode [197] and even the first neutron voltaic, as highlighted in Europhysics News. A currently successful strategy to synthesize boron carbide semiconductors is the cross-linking of icosahedral carboranes of type $C_2B_{10}H_x$ in plasma-enhanced chemical vapor deposition (PECVD). In a related study by Kelber et. al., it has been shown that semiconducting boron carbide can be formed by electron-induced cross-linking of the orthocarboranes [205]. Their claim is that the o-carboranes cross-link though covalent bonding when thin films of o-carborances are exposed to electron beam of 200 eV energy.

Kelber's approach has inspired the study presented in this chapter, as it is a suitable example to illustrate the power of manipulation at the molecular level to build new materials with desired properties. Specifically here my research question was: How does electron bombardment on a thin film of ortho carboranes change the molecular structure of the film and what concomitant changes of the electronic properties arise from this manipulation?

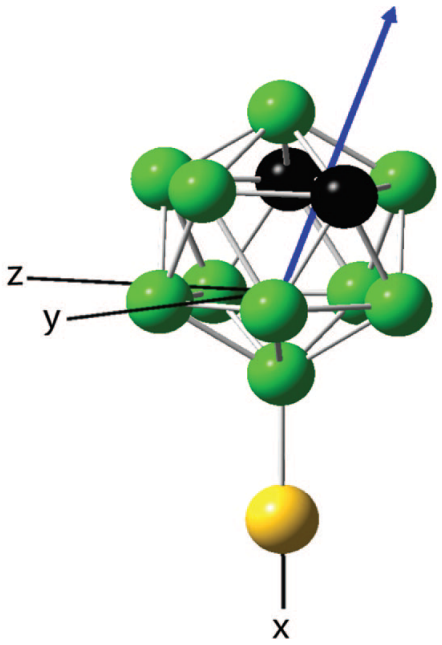

Figure 5.10: Schematic of m-carborane-9-thiol molecule. Boron atoms are shown in green, carbon atoms in black and sulphur in yellow. The arrow shows the direction of electric dipole vector with magnitude of 4.08D [3].

5.4.1 Results and discussion

I selected m-9-carboranthiol ($C_2B_{10}SH_{12}$) for this study shown in figure 5.9. The thiol derivatives were chosen for this study as sulphur atoms bind strongly with the Au substrate [206]. This allowed for the experiments to be performed at room temperature. By contrast, the o-carborane molecules that do not have the thiol group, do not stick to the substrate at room temperature. Therefore, to fabricate films of o-carboranes requires cooling of the substrate to 100 K or below as demonstrated by Pasquale et al [207]. The m-carborane-9-thiol powder, with 97% purity, was purchased from Sigma-Aldrich. The powder was thermally evaporated in a homebuilt Knudsen cell evaporator onto the cleaned Au(111) substrates.

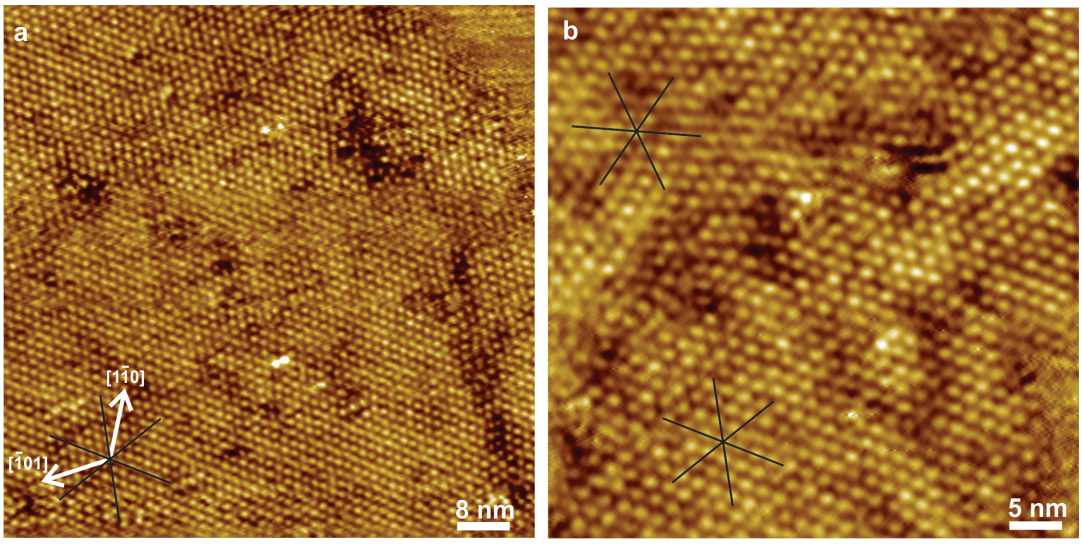

Figure 5.11: STM images for m-carborane-9-thiol on Au(111).

STM images of room temperature grown monolayer film on Au(111) are shown in figure 5.11. Each bright lobe in the STM image can be identified as one molecule as is evident from the size of the lobe of 1.0 nm. The molecules are arranged in rows orientied along three directions, indicated by black lines, such that the network has hexagonal symmetry where each molecule has six nearest nearest neighbors. The nearest neighbor distance is

found to be 1.6 nm from the STM images. The orientation of the molecules on the surface is determined by the thiol group: the sulphur binds strongly with the Au substrate, it is thus expected that the thiol group of the molecule is pointing downwards such that the molecules are standing upright on the substrate (Figure 5.12). The molecular model for carborance-thiol modified gold substrate was proposed by Hohman [3]. The direction of the molecular rows was compared to crystallographic directions obtained from LEED images of clean Au(111), shown in figure 5.11. It is found that the direction of the molecular rows 20.4° rotated with respect to the the substrate's densely packed (110) directions. Also. the domains with other orientations are observed as well. As shown in the figure 5.11(b), two domains with different orientation with respect to the substrate are visible and their orientations with respect to the (110) directions are 20.4° and 24°. It can be concluded from the STM images that the molecules are intact, with their thiol groups sticking to the surface and form a densely packed structure as is expected for weakly interacting spherical objects.

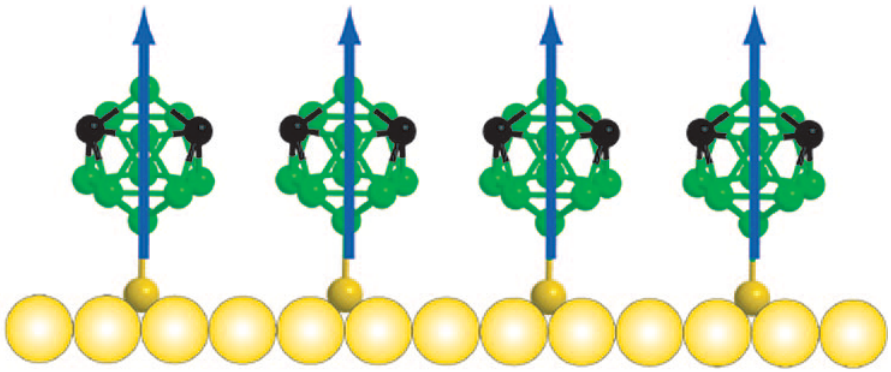

Figure 5.12: Theoretically calculated schematic of m-carborane-9-thiol on Au(111) [3].

The monolayer films were exposed to electron-beam following the strategy used by Kelber et. al, [207]. The energy of the beam was fixed at 200 eV to maintain 4μA of beam current and the films were exposed to this beam for 10 minutes. The beam diameter was

estimated to be 1 mm, which is much smaller than the Au(111) substrate with a diameter of 6 mm. Therefore, only a fraction of the film was exposed to the electron. Figure 5.13 show the STM images of the molecular network obtained after exposing the sample to the electron beam.

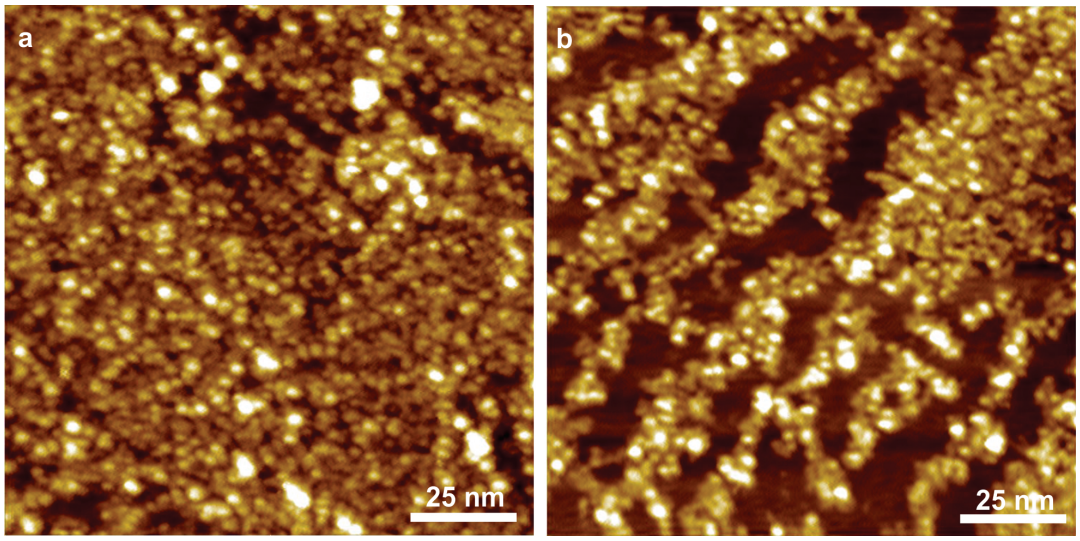

Figure 5.13: STM images for m-craborane-9-thiol on Au(111) after electron bombardment.

As seen from the STM images, there is a clear change in the topography of molecular film after exposure to the beam of electrons. The molecular network is highly disordered and it is difficult to identify individual molecules from the STM images. Also, the exposure to the e-beam resulted in the desorption of molecules as the underlying substrate was visible in few STM images as shown in figure 5.13(b). To find that this change in the morphology of the film is a result of crosslinking between the molecules, as suggested by Kelber et al., we utilized X-ray photoemission spectroscopy. In the simplest case, the crosslinking of these molecules implies H detachment and covalent bond formation between the molecules. The covalent bonding would result in the chemical shift of the core levels of B, C atoms, as explained in the previous section for bis-BN cyclohexane.

The core level spectra for Boron 1s and Carbon 1s are shown in figure 5.14. The spectra

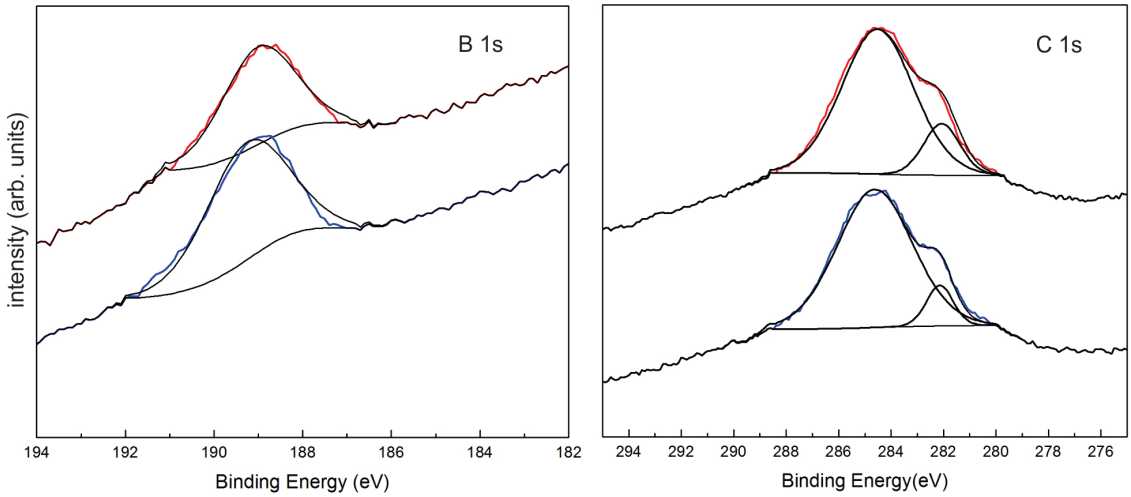

Figure 5.14: Core level XPS for as grown (blue) and e-beam exposed m-carborane-9-thiol film on Au(111) (red).

for the condensed film prior to electron bombardment indicate a B 1s feature centered at 189.3 eV, and two C 1s peaks centered at 285 eV and 283 eV. The comparison with the XPS spectra taken after electron bombardment shows that the B 1s peak is shifted to the lower binding energy by 0.3 eV. However, no shift was observed in the positions two C 1s peaks. Similar shift in the B 1s binding energy was already described by Pasquale et al. for o-carborane films [207]. The detailed analysis showed there that the crosslinking occurs at boron sites whereas carbon atoms do not participate in the crosslinking.

If the molecules are indeed crosslinking due to electron bombardment, the electronic properties of the molecular film are thus expected to change as well. This can result in the change of LDOS and hence the conductivity of the films. To test this, I have used the scanning tunneling spectroscopy to measure the change in the LDOS, which is proportional to the conductance of the molecular film, as discussed in chapter 2. Figure 5.15 shows the LDOS of as grown film and e-beam exposed film. A lock-in technique, as explained in chapter 2, was used to obtain the dI/dV vs V spectra for the film before and after the electron bombardment. The spectra was obtained by averaging over 400 point spectra taken

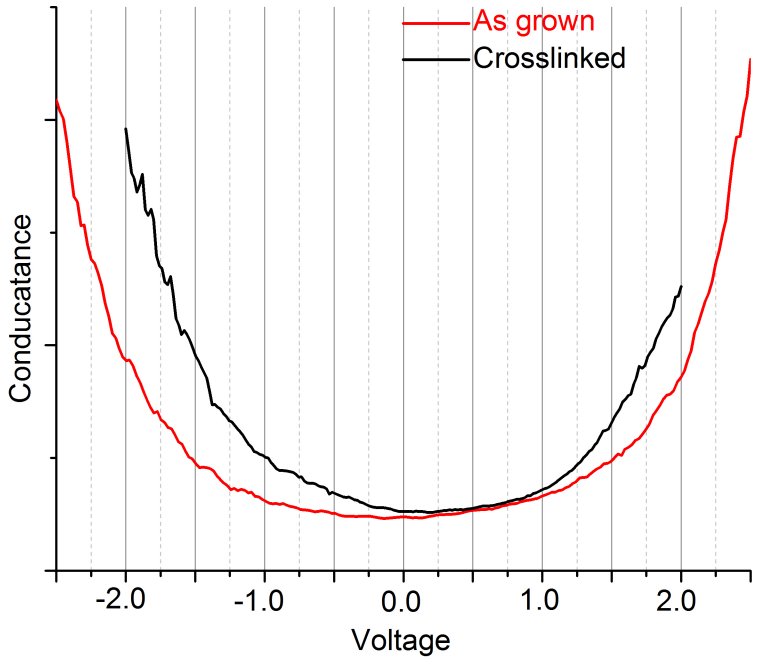

Figure 5.15: The LDOS for as grown and crosslinked film obtained from STS.

on different parts of the sample. As seen from the red curve in the figure 5.15, the conductance of the as grown film had a region of $\pm$1.5 eV on each side of the Fermi level (V=0), which implies that the there are no molecular energy levels in that region. The conductance increases to finite value in the voltage region $\pm$ 1.5 to 2.5 volts on either side of the Fermi level. Therefore, the HOMO and LUMO can be assigned the values -1.5 eV and 1.5 eV respectively, with respect to the Fermi level. This implies that the molecules in the as grown m-carborane film have electronic band gap of 3 eV. The conductance curve obtained for the film after e-bombardment shows that the region of zero conductance is significantly decreased as seen in the black curve. The HOMO level is approximately -0.6 eV below the Fermi level and LUMO is approximately 1 eV above the Fermi level. Therefore, the electronic band gap in crosslinked molecules is about 1.6 eV. This is an evidence of

electron-bombardment induced change in the electronic properties of m-carboranes.

It is thus reasonable to conclude here that the electron bombardment affects both the morphology of the film as well as its electronic properties such that the band gap after the electron bombardment is significantly reduced. The shift of the core level XPS of B 1s to the lower binding energy suggests that the e-bombardment has induced bond formation between the neighboring molecules.

5.5 Conclusion

To conclude this chapter, I have synthesized boron, carbon and nitrogen containing two dimensional nanostructures that are potential semiconductors due to their small band gap. In the first case, the dehydrogenation, thermally activated or catalytically activated by the surface, of a precursor molecules allows for covalent bond formation between the molecular ring. This bottom-up approach is crucial for the synthesis of two dimensional materials with desired structures whose properties can be manipulated by using different monomers. Second, technique developed by Kelber et. al., [207], allows for the site specific covalent bonding by dehydrogenation of carborane molecules using the momentum from incident electrons.

Chapter 6

Concluding Remarks

In this study, I have used a powerful combination of surface science techniques to fabricate and investigate nanostructures from functional molecules. Starting from a carefully selected choice of functional molecules, I wanted to explore how these molecules pack on substrate surfaces, and how they can be stabilized into structures that do not exist in the bulk. And, indeed I found that 3-HPLN molecule arrange into low-dimensional nanostructures in many ways, very different from their bulk structure. Interestingly, I was able to stabilize these into one dimensional chains that were over 100 nm long, wherein the structural motif that leads to their ferroelectric behavior in the bulk, H-bond to π-system is preserved. Other notable structures, such as the three dimensional Kagome-like lattice and porous chiral networks, can be observed at different coverage and annealing temperatures. These structures preserve the hydrogen bonding from the bulk, but the formation of these new structures suggests that the preparation method and the substrates play a role in determining the self-assembly of 3-HPLN.

Another exciting result is the newly discovered h-BCN network. After the impactful discovery of h-BN and graphene, I was able to discover a new, graphene-like structure that contain B, C and N on the graphenic lattice sites. These results are very new and many

other questions regarding precise atomic structure, band structure, and transport properties remain. Yet, it is expected that my findings will trigger considerable work by the community.

An important parameter for self-assembly and properties is the supporting substrate. The BCN was formed in the presence of a substrate. The structures of 3-HPLN were also influenced by the substrate. Impressively, the magnetic properties of SCO were drastically influenced by the substrate as well. My experiments showed that those SCO molecules that are in direct contact with the substrate have a drastically different SCO transition than those who are not in contact with the substrate. This effect is attributed to the substrate induced change in the conformation as well as the electronic structure of these molecules. What make this study so powerful is the comprehensiveness of the data obtained. For the SCO complex, we got microscopic structural imaging, core level spectroscopy data, unoccupied energy states, and magnetic information from resonant X-ray absorption spectroscopy. My studies are thus well-suited to establish a structure-properties relationship by uniquely connecting precise molecular bonding pattern, substrate adsorption sites and band structure data.

I believe I just opened a new door towards designed functional 1D and 2D nanostructures. The basic science established in this study will accelerate the development of functional organic materials that can potentially replace traditional inorganic semiconductors because of the designed, additional functionality they have to offer. Further studies must allow to increase the complexity and functionality further by co-crystallization or building hetero structures.

Bibliography

[1] Juan A. Colon Santana. The role of rare earth dopants in semiconducting host system for spin electronic devices, 2012.

[2] Jin-Young Son, Kou Takubo, Daisuke Asakura, James W. Quilty, Takashi Mizokawa, Akio Nakamoto, and Norimichi Kojima. Photoemission Study of Temperature-Induced and Photoinduced Spin-State Transitions in Spin-Crossover Complex $[Fe(ptz)_6](BF_4)_2$. *J. Phys. Soc. Jpn.*, 76:084703, 2007.

[3] J Nathan Hohman, Pengpeng Zhang, Elizabeth I Morin, Patrick Han, Moonhee Kim, Adam R Kurland, Patrick D McClanahan, Viktor P Balema, and Paul S Weiss. Self-Assembly of Carboranethiol Isomers on Au111: Intermolecular Interactions Determined by Molecular Dipole Orientations. *ACS Nano*, 3:527–536, 2009.

[4] Hylke B Akkerman, Paul W M Blom, Dago M de Leeuw, and Bert de Boer. Towards molecular electronics with large-area molecular junctions. *Nature*, 441:69–72, 2006.

[5] Amar H. Flood, J. Fraser Stoddart, David W. Steuerman, and James R. Heath. Whence molecular electronics? *Science*, 306(5704):2055–2056, 2004.

[6] James R. Heath. Molecular Electronics. *Annual Review of Materials Research*, 39:1–23, 2009.

[7] Adam Johan Bergren and Richard L. McCreery. Analytical Chemistry in Molecular Electronics. *Annual Review of Analytical Chemistry*, 4:173–195, 2011.

[8] S Yasuda, T Nakamura, M Matsumoto, and H Shigekawa. Phase Switching of a Single Isomeric Molecule and Associated Characteristic Rectification. *J. Am. Chem. Soc.*, 125:1643016433, 2003.

[9] A J Kronemeijer, H B Akkerman, T Kudernac, B J van Wees, B L Feringa, P W M Blom, and B de Boer. Reversible Conductance Switching in Molecular Devices. *Adv. Mat.*, 8:1467–1473, 2008.

[10] L Venkataraman, J E Klare, C Nuckolls, M S Hybertsen, and M L Steigerwald. Dependence of Single Molecule Junction Conductance on Molecular Conformation. *Nature*, 442:904–907, 2006.

[11] I Díez-Pérez, J Hihath, Y Lee, L Yu, L Adamska, M A Kozhushner, I I Oleynik, and N Tao. Rectification and stability of a single molecular diode with controlled orientation. *Nat. Chem.*, 1:635 – 641, 2009.

[12] S Pan, Q Fu, T Huang, A Zhao, B Wang, Y Luo, J Yang, and J Hou. Design and control of electron transport properties of single molecules. *PNAS*, 106:5259 15263, 2009.

[13] N Nerngchamnong, L Yuan, D-C Qi, J Li, D Thompson, and C A Nijhuis. The role of van der Waals forces in the performance of molecular diodes. *Nat. Nano.*, 8:113118, 2013.

[14] J Park, A N Pasupathy, J I Goldsmith, C Chang, Y Yaish, J R Petta, M Rinkoski, J P Sethna, H D Abruña, P L McEuen, and D C Ralph. Coulomb blockade and the Kondo effect in single-atom transistors. *Nature*, 417:722–725, 2002.

[15] Bingqian Xu, Xiaoyin Xiao, Xiaomei Yang, Ling Zang, and Nongjian Tao. Large Gate Modulation in the Current of a Room Temperature Single Molecule Transistor. *J. Am. Chem. Soc.*, 127:23862387, 2005.

[16] F Jäckel, M D Watson, K Müllen, and J P Rabe. Prototypical Single-Molecule Chemical-Field-Effect Transistor with Nanometer-Sized Gates. *Phys. Rev. lett.*, 92:188303, 2004.

[17] Ismael Diez-Perez, Zhihai Li, Joshua Hihath, Jinghong Li, Chengyi Zhang, Xiaomei Yang, Ling Zang, Yijun Dai, Xinliang Feng, Klaus Muellen, and Nongjian Tao. Gate-controlled electron transport in coronenes as a bottom-up approach towards graphene transistors. *Nat. Comm.*, 1, 2010.

[18] D. Tyler McQuade, Anthony E. Pullen, , and Timothy M. Swager. Conjugated Polymer-Based Chemical Sensors. *Chemical Reviews*, 100:2537–2574, 2000.

[19] Jesse D. Fowler, Matthew J. Allen, Vincent C. Tung, Yang Yang, Richard B. Kaner, and Bruce H. Weiller. Practical Chemical Sensors from Chemically Derived Graphene. *ACS Nano*, 3(2):301–306, 2009.

[20] Pramod Reddy, Sung-Yeon Jang, Rachel A Segalman, and Arun Majumdar. Thermoelectricity in Molecular Junctions. *Science*, 315:1568–1571, 2007.

[21] David J. Gundlach. Organic electronics: Low power, high impact. *Nat Mater*, 6:173–174, 2007.

[22] S R Forrest. The path to ubiquitous and low-cost organic electronic appliances on plastic. *Nature*, pages 911–918, 2004.

[23] J-S Park, H Chae, H K Chung, and S I Lee. Thin film encapsulation for flexible AM-OLED: a review. *Semi. Sci. Tech.*, 26:034001, 2011.

[24] Gang Li, Rui Zhu, and Yang Yang. Polymer solar cells. *Nat. Photon.*, 6:153161, 2012.

[25] H Zhang, S Jenatsch, J De Jonghe, F Nüesch, R Steim, A C Véron, and R Hany. Transparent Organic Photodetector using a Near-Infrared Absorbing Cyanine Dye. *Sci. Rep.*, 5, 2015.

[26] Emanuel Lortscher. Wiring molecules into circuits. *Nat Nano*, 8:381–384, 2013.

[27] Mark Ratner. A brief history of molecular electronics. *Nat Nano*, 8:378–380, 2013.

[28] Richard L. McCreery. Analytical Challenges in Molecular Electronics. *Analytical Chemistry*, 78(11):3490–3497, 2006.

[29] K M Mertes, Y Suzuki, M P Sarachik, Y Myasoedov, H Shtrikman, E Zeldov, E M Rumberger, D N Hendrickson, and G Christou. Mn12-acetate: a prototypical single molecule magnet. *Solid State Comm.*, 127:131139, 2003.

[30] Azzedine Bousseksou, Gabor Molnar, Lionel Salmona, and William Nicolazzia. Molecular spin crossover phenomenon: recent achievements and prospects. *Chem. Soc. Rev.*, 40:3313–3335, 2011.

[31] Pierrick Durand, Sebastien Pillet, El-Eulmi Bendeif, Cedric Carteret, Mohamed Bouazaoui, Hicham El Hamzaoui, Bruno Capoen, Lionel Salmon, Sylvie Hebert, Jaafar Ghanbaja, Lionel Arandah, and Dominik Schanielab. Room temperature bistability with wide thermal hysteresis in a spin crossover silica nanocomposite. *J. Mat. Chem. C*, 1:933–1942, 2013.

[32] T Q Hung, F Terki, S Kamara, M Dehbaoui, S Charar, B Sinha, C Kim, P Gandit, I A Guralskiy, G Molnár, L Salmon, H J Shepherd, and A Bousseksou. Room Temperature Magnetic Detection of Spin Switching in Nanosized Spin-Crossover Materials. *Angew. Chem. Int. Ed.*, 2012.

[33] Ferry Prins, Maraa Monrabal-Capilla, Edgar A Osorio, and Herre S J van der Zant Eugenio Coronado. Room-Temperature Electrical Addressing of a Bistable Spin-Crossover Molecular System. *Adv. Mat.*, 23:1545–1549, 2011.

[34] V Ksenofontov, A B Gaspar, G Levchenko, B Fitzsimmons, and P Gütlich. Pressure Effect on Spin Crossover in $[Fe(phen)_2(NCS)_2]$ and $[CrI_2(depe)_2]$. *J. Phys. Chem. B*, 108:77237727, 2004.

[35] X Zhang, T Palamarciuc, J-F Létard, P Rosa, E V Lozada, F Torres, L G Rosa, B Doudin, and P A Dowben. The spin state of a molecular adsorbate driven by the ferroelectric substrate polarization. *Chem. Comm.*, 50:2255, 2014.

[36] Holger Naggert, Alexander Bannwarth, Steffen Chemnitz, Thomas von Hofe, Eckhard Quandt, and Felix Tuczek. First observation of light-induced spin change in vacuum deposited thin films of iron spin crossover complexes. *Dalton Trans.*, 40:6364–6366, 2011.

[37] Y Li Huang, Y Lu, T C Niu, H Huang, S Kera, N Ueno, A T S Wee, and W Chen. Reversible Single-Molecule Switching in an Ordered Monolayer Molecular Dipole Array. *Small*, 8:1423–1428, 2012.

[38] K. S. Novoselov, D. Jiang, F. Schedin, T. J. Booth, V. V. Khotkevich, S. V. Morozov, and A. K. Geim. Two-dimensional atomic crystals. *PNAS*, 102(30):10451–10453, 2005.

[39] Ruben Mas-Balleste, Cristina Gomez-Navarro, Julio Gomez-Herrero, and Felix Zamora. 2d materials: to graphene and beyond. *Nanoscale*, 3:20–30, 2011.

[40] K.I. Bolotin, K.J. Sikes, Z. Jiang, M. Klima, G. Fudenberg, J. Hone, P. Kim, and H.L. Stormer. Ultrahigh electron mobility in suspended graphene. *Solid State Communications*, 146:351 – 355, 2008.

[41] Qing Hua Wang, Kourosh Kalantar-Zadeh, Andras Kis, Jonathan N. Coleman, and Michael S. Strano. Electronics and optoelectronics of two-dimensional transition metal dichalcogenides. *Nat Nano*, 7:699–712, 2012.

[42] K D Gronwald and M Henzler. Epitaxy of Si(111) as studied with a new high resolving LEED system. *Surf. Sci.*, 117:180 – 187, 1982.

[43] T-M Lu and M G Lagally. The resolving power of a low-energy electron diffractometer and the analysis of surface defects. *Surf. Sci.*, 99:695 – 713, 1980.

[44] M Kammler and M Horn von Hoegen. Low energy electron diffraction of epitaxial growth of bismuth on Si(111). *Surf. Sci.*, 576:56–60, 2005.

[45] L H Dubois, D G Castner, and G A Somorjai. The chemisorption of acetylene and ethylene on Rh(111): A low energy electron diffraction (LEED), high resolution electron energy loss (ELS), and thermal desorption mass spectrometry (TDS) study. *J. Chem. Phys.*, 72:5234–5240, 1980.

[46] G Binnig, H Rohrer, C Gerber, and E Weibel. Surface Studies by Scanning Tunneling Microscopy. *Phys. Rev. Lett.*, 49:57–61, 1982.

[47] G Binnig, H Rohrer, C Gerber, and E Weibel. Tunneling through a controllable vacuum gap. *Appl. Phys. Lett.*, 40:178–180, 1982.

[48] L A Nagahara, T Thundat, and S M Lindsay. Preparation and characterization of STM tips for electrochemical studies. *Rev. Sci. Inst.*, 60:3128–3130, 1989.

[49] L A Hockett and S E Creager. A convenient method for removing surface oxides from tungsten STM tips. *Rev. Sci. Inst.*, 64:263–264, 1993.

[50] C J Chen. Origin of atomic resolution on metal surfaces in scanning tunneling microscopy. *Phys. Rev. Lett.*, 65:448–451, 1990.

[51] T Maroutian, S Degen, C Becker, K Wandelt, and R Berndt. Superstructures and coincidences of a thin oxide film on a metallic substrate: A STM study. *Phys. Rev. B*, 68:155414, 2003.

[52] Xumin Chen. *Ultrathin Oxide Films as Templates for Magnetic Nanostructures*. PhD thesis, University of Nebraska, Lincoln, 2012.

[53] F Matino, L Persano, V Arima, D Pisignano, R I R Blyth, R Cingolani, and R Rinaldi. Electronic structure of indium-tin-oxide films fabricated by reactive electron-beam deposition. *Phys. Rev. B*, 72:085437, 2005.

[54] L Giordano, G Pacchioni, J Goniakowski, N Nilius, E D L Rienks, and H-J Freund. Charging of Metal Adatoms on Ultrathin Oxide Films: Au and Pd on FeO/Pt(111). *Phys. Rev. Lett.*, 101:026102, 2008.

[55] D A Kunkel. *Polarization phenomenon on organic nanostructures*. PhD thesis, Univesity of Nebraska, 2014.

[56] M J Comstock, N Levy, A Kirakosian, J Cho, F Lauterwasser, J H Harvey, D A Strubbe, J M J Frechet, D Trauner, S G Louie, and M F Crommie. Reversible Photomechanical Switching of Individual Engineered Molecules at a Metallic Surface. *Phys. Rev. Lett.*, 99:038301, 2007.

[57] A G Thomas and K L Syres. Adsorption of organic molecules on rutile TiO_2 and anatase TiO_2 single crystal surfaces. *Chem. Soc. Rev.*, 41:4207–4217, 2012.

[58] N Lorente, R Rurali, and H Tang. Single-molecule manipulation and chemistry with the STM. *J. Phys. Cond. Mat.*, 17, 2005.

[59] J V Barth. Molecular Architectonic on Metal Surfaces. *A Rev. Phys. Chem.*, 58:375–407, 2007.

[60] J Bardeen, L N Cooper, and J R Schrieffer. Theory of Superconductivity. *Phys. Rev.*, 108:1175–1204, 1957.

[61] J Tersoff and D R Hamann. Theory and Application for the Scanning Tunneling Microscope. *Phys. Rev. Lett.*, 50:1998–2001, 1983.

[62] J Tersoff and D R Hamann. Theory of the scanning tunneling microscope. *Phys. Rev. B*, 31:805–813, 1985.

[63] Z Klusek, W Kozlowski, Z Waqar, S Datta, J S Burnell-Gray, I V Makarenko, N R Gall, E V Rutkov, A Y Tontegode, and A N Titkov. Local electronic edge states of graphene layer deposited on Ir(111) surface studied by STM/CITS. *Appl. Surf. Sci.*, 252:1221 – 1227, 2005.

[64] Z Alpichshev, J G Analytis, J-H Chu, I R Fisher, Y L Chen, Z X Shen, A Fang, and A Kapitulnik. STM Imaging of Electronic Waves on the Surface of Bi2Te3: Topologically Protected Surface States and Hexagonal Warping Effects. *Phys. Rev. Lett.*, 104:016401, 2010.

[65] Y Yamagishi, S Nakashima, K Oiso, and T K Yamada. Recovery of nanomolecular electronic states from tunneling spectroscopy: LDOS of low-dimensional phthalocyanine molecular structures on Cu(111). *Nanotech.*, 24:395704, 2013.

[66] K Petukhov, M S Alam, H Rupp, S Stromsdorfer, P Muller, A Scheurer, R W Saalfrank, J Kortus, A Postnikov, M Ruben, L K Thompson, and J-M Lehn. STM spectroscopy of magnetic molecules. *Coord. Chem. Rev.*, 253:2387 – 2398, 2009.

[67] T Frederiksen, M Paulsson, and H Ueba. Theory of action spectroscopy for single-molecule reactions induced by vibrational excitations with STM. *Phys. Rev. B*, 89:035427, 2014.

[68] N Okabayashi, Y Konda, and T Komeda. Inelastic Electron Tunneling Spectroscopy of an Alkanethiol Self-Assembled Monolayer Using Scanning Tunneling Microscopy. *Phys. Rev. Lett.*, 100:217801, 2008.

[69] Y Sainoo, Y Kim, T Okawa, T Komeda, H Shigekawa, and M Kawai. Excitation of Molecular Vibrational Modes with Inelastic Scanning Tunneling Microscopy Processes: Examination through Action Spectra of *cis*-2-Butene on Pd(110). *Phys. Rev. Lett.*, 95:246102, 2005.

[70] J Repp, G Meyer, S M Stojkovi, A Gourdon, and C Joachim. Molecules on Insulating Films: Scanning-Tunneling Microscopy Imaging of Individual Molecular Orbitals. *Phys. Rev. Lett.*, 94:026803, 2005.

[71] Y-C Chen, D G de Oteyza, Z Pedramrazi, C Chen, F R Fischer, and M F Crommie. Tuning the Band Gap of Graphene Nanoribbons Synthesized from Molecular Precursors. *ACS Nano*, 7:6123–6128, 2013.

[72] T Masateru, T Makusu, Y Kazumichi, and K Tomoji. Inelastic electron tunneling spectroscopy of single-molecule junctions using a mechanically controllable break junction. *Nanotech.*, 20:434008, 2009.

[73] G Binnig, H Rohrer, C Gerber, and E Weibel. 7 x 7 Reconstruction on Si(111) Resolved in Real Space. *Phys. Rev. Lett.*, 50:120–123, 1983.

[74] Markus Ternes. *Scanning tunneling spectroscopy at the single atom scale*. PhD thesis.

[75] G. Binnig, C. F. Quate, and Ch. Gerber. Atomic Force Microscope. *Phys. Rev. Lett.*, 56:930–933, 1986.

[76] J Moser, A Verdaguer, D Jimnez, A Barreiro, and A Bachtold. The environment of graphene probed by electrostatic force microscopy. *Appl. Phys. Lett.*, 92, 2008.

[77] C Ronny, C Guy, S Asaf, R Eran, and B Uri. Electrostatic Force Microscopy Study of Single AuCdSe Hybrid Nanodumbbells: Evidence for Light-Induced Charge Separation. *Nano Lett.*, 9:2031–2039, 2009.

[78] S H Yang, M Nosonovsky, H Zhang, and K-H Chung. Nanoscale water capillary bridges under deeply negative pressure. *Chem. Phys. Lett.*, 451:88 – 92, 2008.

[79] E. Sahagún, P. García-Mochales, G. M. Sacha, and J. J. Sáenz. Energy Dissipation due to Capillary Interactions: Hydrophobicity Maps in Force Microscopy. *Phys. Rev. Lett.*, 98:176106, 2007.

[80] L Gross, F Mohn, N Moll, P Liljeroth, and G Meyer. The Chemical Structure of a Molecule Resolved by Atomic Force Microscopy. *Science*, 325:1110–1114, 2009.

[81] S Schreiber, M Savla, D V Pelekhov, D F Iscru, C Selcu, P Chris Hammel, and G Agarwal. Magnetic Force Microscopy of Superparamagnetic Nanoparticles. *Small*, 4(2), 2008.

[82] M. Jaafar, J. Gomez-Herrero, A. Gil, P. Ares, and A. Asenjo M. Vazqueza. Variable-field magnetic force microscopy. *Ultramicroscopy*, 109:693 – 699, 2009.

[83] S Morita, F J Giessibl, E Meyer, and R Wiesendanger. *Noncontact Atomic Force Microscopy*. Springer, 2009.

[84] S Jesse, A P Baddorf, and S V Kalinin. Switching spectroscopy piezoresponse force microscopy of ferroelectric materials. *Appl. Phys. Lett.*, 88, 2006.

[85] B J Rodriguez, S Jesse, A P Baddorf, and S V Kalinin. High Resolution Electromechanical Imaging of Ferroelectric Materials in a Liquid Environment by Piezoresponse Force Microscopy. *Phys. Rev. Lett.*, 96:237602, 2006.

[86] A Gruverman and S V Kalinin. Piezoresponse force microscopy and recent advances in nanoscale studies of ferroelectrics. *J. Mat. Sci.*, 41:107–116.

[87] A Gruverman, D Wu, and J F Scott. Piezoresponse Force Microscopy Studies of Switching Behavior of Ferroelectric Capacitors on a 100-ns Time Scale. *Phys. Rev. Lett.*, 100:097601, 2008.

[88] P Gaethner and K Dransfeld. Local poling of ferroelectric polymers by scanning force microscopy. *Appl. Phys. Lett.*, 61:1137–1139, 1992.

[89] M. P. Seah and W. A. Dench. Quantitative electron spectroscopy of surfaces: A standard data base for electron inelastic mean free paths in solids. *Surface and Interface Analysis*, 1:2–11, 1979.

[90] Louis de Broglie. XXXV. A tentative theory of light quanta. *Philosophical Magazine Series 6*, 47:446–458, 1924.

[91] C Davisson and L H Germer. Diffraction of Electrons by a Crystal of Nickel. *Phys. Rev.*, 30:705–740, 1927.

[92] C Nordling, E Sokolowski, and K Siegbahn. Precision Method for Obtaining Absolute Values of Atomic Binding Energies. *Phys. Rev.*, 105:1676–1677, 1957.

[93] M R Alexander, G E Thompson, X Zhou, G Beamson, and N Fairley. Quantification of oxide film thickness at the surface of aluminium using XPS. *Surf. Inter. Anal.*, 34, 2002.

[94] I G Hill, A Kahn, Z G Soos, and R A Pascal Jr. Charge-separation energy in films of pi-conjugated organic molecules. *Chem. Phys. Lett.*, 327:181 – 188, 2000.

[95] I G Hill, D Milliron, J Schwartz, and A Kahn. Organic semiconductor interfaces: electronic structure and transport properties. *Appl. Surf. Sci.*, 166:354 – 362, 2000.

[96] H Ishii and K Seki. Energy level alignment at organic/metal interfaces studied by UV photoemission: breakdown of traditional assumption of a common vacuum level at the interface. *IEEE Trans. Elec. Dev.*, 44:1295–1301, 1997.

[97] I G Hill, A Kahn, J Cornil, D A dos Santos, and J L Brdas. Occupied and unoccupied electronic levels in organic -conjugated molecules: comparison between experiment and theory. *Chem. Phys. Lett.*, 317:444 – 450, 2000.

[98] E V Tsiper, Z G Soos, W Gao, and A Kahn. Electronic polarization at surfaces and thin films of organic molecular crystals: PTCDA. *Chem. Phys. Lett.*, 360:47 – 52, 2002.

[99] Takeo Furukawa. Ferroelectric properties of vinylidene fluoride copolymers. *Phase Transitions*, 18(3-4):143–211, 1989.

[100] Kei Noda, Kenji Ishida, Atsushi Kubono, Toshihisa Horiuchi, Hirofumi Yamada, and Kazumi Matsushige. Remanent polarization of evaporated films of vinylidene fluoride oligomers. *Journal of Applied Physics*, 93, 2003.

[101] Sachio Horiuchi and Yoshinori Tokura. Organic ferroelectrics. *Nat Mater*, 7:357–365, 2008.

[102] Da-Wei Fu, Hong-Ling Cai, Yuanming Liu, Qiong Ye, Wen Zhang, Yi Zhang, Xue-Yuan Chen, Gianluca Giovannetti, Massimo Capone, Jiangyu Li, and Ren-Gen Xiong. Diisopropylammonium Bromide Is a High-Temperature Molecular Ferroelectric Crystal. *Science*, 339(6118):425–428, 2013.

[103] S Horiuchi, Y Tokunaga, G Giovannetti, S Picozzi, H Itoh, R Shimano, R Kumai, and Y Tokura. Above-room-temperature ferroelectricity in a single-component molecular crystal. *Nature*, 463:789–792, 2010.

[104] A. Yu. Emelyanov, N. A. Pertsev, and A. L. Kholkin. Effect of external stress on ferroelectricity in epitaxial thin films. *Phys. Rev. B*, 66:214108, 2002.

[105] Per-Gunnar Jonsson and Walter C Hamilton. Hydrogen Bond Studies. LX A Single Crystal Neutron Diffraction Study of Trichloroacetic Acid Dimer. *Journal of Chemical Physics*, 56:4433–4439, 1972.

[106] J. Trotter and T. Zobel. 826. Stereochemistry of arsenic. Part XVI. Cacodylic acid. *J. Chem. Soc.*, pages 4466–4471, 1965.

[107] Gilli Gastone, Bellucci Fabrizio, Ferretti Valeria, and Bertolasi Valerio. Evidence for resonance-assisted hydrogen bonding from crystal-structure correlations on the enol form of the .beta.-diketone fragment. *Journal of the American Chemical Society*, 111:1023–1028, 1989.

[108] S Horiuchi, R Kumai, and Y Tokura. Hydrogen-bonding molecular chains for high-temperature ferroelectricity. *Advanced Materials*, 23:2098–2103, 2011.

[109] Donna A Kunkel, James Hooper, Scott Simpson, Sumit Beniwal, Katie L Morrow, Douglas C Smith, Kimberley Cousins, Stephen Ducharme, Eva Zurek, and Axel Enders. Rhodizonic Acid on Noble Metals: Surface Reactivity and Coordination Chemistry. *The Journal of Physical Chemistry Letters*, 2013.

[110] Donna A Kunkel, James Hooper, Scott Simpson, Geoffrey A Rojas, Stephen Ducharme, Timothy Usher, Eva Zurek, and Axel Enders. Proton transfer in surface-stabilized chiral motifs of croconic acid. *Physical Review B*, 2013.

[111] T Mochida, S Matsumiya, A Izuoka, N Sato, T Sugawara, and Y Sugawara. Structure of 3-hydroxyphenalenone. *Acta Crystallogr. Sect. C Cryst. Struct. Commun.*, 48:680–683, 1992.

[112] F Silly, A Q Shaw, M R Castell, G A D Briggs, M Mura, N Martsinovich, and L Kantorovich. Melamine Structures on the Au(111) Surface. *J. Phys. Chem. C*, 112:11476–11480, 2008.

[113] M Mura, F Silly, V Burlakov, M R Castell, G A D Briggs, and L N Kantorovich. Formation mechanism for a hybrid supramolecular network involving cooperative interactions. *Phys. Rev. Lett.*, 108:176103, 2012.

[114] Yinying Wei, Steve W Robey, and Janice E Reutt-Robey. Flux-Selected Titanyl Phthalocyanine Monolayer Architecture on Ag (111). *J. Phys. Chem. C*, 112:18537–18542, 2008.

[115] Wende Xiao, Xinliang Feng, Pascal Ruffieux, Oliver Groning, Klaus Mullen, and Roman Fasel. Self-assembly of chiral molecular honeycomb networks on Au(111). *J. Am. Chem. Soc.*, 130:8910–8912, 2008.

[116] Nan Jiang, Yeliang Wang, Qi Liu, Yuyang Zhang, Zhitao Deng, Karl-Heinz Ernst, and Hong-Jun Gao. Polymorphism and chiral expression in two-dimensional subphthalocyanine crystals on Au(111). *Phys. Chem. Chem. Phys.*, 12:1318–1322, 2010.

[117] J A Theobald, N S Oxtoby, M A Phillips, N R Champness, and P H Beton. Controlling molecular deposition and layer structure with supramolecular surface assemblies. *Nature*, 424:1029–1031, 2003.

[118] Mario Ruben, Dietmar Payer, Aitor Landa, Alessio Comisso, Chiara Gattinoni, Nian Lin, Jean-Paul Collin, Jean-Pierre Sauvage, Alessandro De Vita, , and Klaus Kern. 2D supramolecular assemblies of benzene-1,3,5-triyl-tribenzoic acid: temperature-induced phase transformations and hierarchical organization with macrocyclic molecules. *J. Am. Chem. Soc.*, 128:15644–15651, 2006.

[119] James Hooper, Donna A Kunkel, Scott Simpson, Sumit Beniwal, Axel Enders, and Eva Zurek. Chiral surface networks of 3-HPLN A molecular analog of rounded triangle assembly. *Surf. Sci.*, 629:65–74, 2014.

[120] Sumit Beniwal, Shuang Chen, Donna A Kunkel, James Hooper, Scott Simpson, Eva Zurek, Xiao Cheng Zeng, and Axel Enders. Kagome-like lattice of π-π stacked 3-hydroxyphenalenone on Cu(111). *Chem. Commun.*, 50:8659–8662, 2014.

[121] Nian Lin, Alexandre Dmitriev, Jens Weckesser, Johannes V Barth, and Klaus Kern. Real-time single-molecule imaging of the formation and dynamics of coordination compounds. *Angew. Chem. Int. Ed. Engl.*, 41:4779–4783, 2002.

[122] Donna A Kunkel, James Hooper, Scott Simpson, Sumit Beniwal, Katie L Morrow, Douglas C Smith, Kimberly Cousins, Stephen Ducharme, Eva Zurek, and Axel Enders. Rhodizonic Acid on Noble Metals: Surface Reactivity and Coordination Chemistry. *J. Phys. Chem. Lett.*, 4:3413–3419, 2013.

[123] C C Perry, S Haq, B G Frederick, and N V Richardson. Face specificity and the role of metal adatoms in molecular reorientation at surfaces. *Surf. Sci.*, 409:512–520, 1998.

[124] M N Faraggi, C Rogero, A Arnau, M Trelka, D Écija, C Isvoranu, J Schnadt, C Marti-Gastaldo, E Coronado, J M Gallego, R Otero, and R Miranda. Role of Deprotonation and Cu Adatom Migration in Determining the Reaction Pathways of Oxalic Acid Adsorption on Cu(111). *J. Phys. Chem. C*, 115:21177–21182, 2011.

[125] Steven L Tait, Hyuna Lim, Arjun Theertham, and Peter Seidel. First layer compression and transition to standing second layer of terephthalic acid on Cu(100). *Phys. Chem. Chem. Phys.*, 14:8217–8223, 2012.

[126] T Miyamachi, M Gruber, V Davesne, M Bowen, S Boukari, L Joly, F Scheurer, G Rogez, T K Yamada, P Ohresser, E Beaurepaire, and W Wulfhekel. Robust spin crossover and memristance across a single molecule. *Nat. Comm.*, 3:938, 2012.

[127] Ben Warner, Jenny C Oberg, Tobias G Gill, Fadi El Hallak, Cyrus F Hirjibehedin, Michele Serri, Sandrine Heutz, Marie-Anne Arrio, Philippe Sainctavit, Matteo Mannini, Giordano Poneti, Roberta Sessoli, and Patrick Rosa. Temperature- and Light-Induced Spin Crossover Observed by X-ray Spectroscopy on Isolated Fe(II) Complexes on Gold. *J. Phys. Chem. Lett.*, 4:1546, 2013.

[128] Xin Zhang, Tatiana Palamarciuc, Patrick Rosa, Jean-Francois Letard, Bernard Doudin, ZhengZheng Zhang, Jian Wang, and Peter A Dowben. Electronic Structure of a Spin Crossover Molecular Adsorbate. *J. Phys. Chem. C*, 116:23291–23296, 2012.

[129] Andreas Hauser. Intersystem crossing in the $[Fe(ptz)_6](BF_4)_2$ spin crossover system (ptz=1-propyltetrazole). *Journal of Chemical Physics*, 94(4):2741–2749, 1991.

[130] Xin Zhang, Sai Mu, Guillaume Chastanet, Nathalie Daro, Tatiana Palamarciuc, Patrick Rosa, Jean-Francois Letard, Jing Liu, George E Sterbinsky, Dario A Arena, Celine Etrillard, Bohdan Kundys, Bernard Doudin, and Peter A Dowben. Complexities in the Molecular Spin Crossover Transition. *J. Phys. Chem. C*, 119:16293–16302, 2015.

[131] Thiruvancheril G Gopakumar, Matthias Bernien, Holger Naggert, Francesca Matino, Christian F Hermanns, Alexander Bannwarth, Svenja Muhlenberend, Alex Kruger, Dennis Kruger, Fabian Nickel, Waldemar Walter, Richard Berndt, Wolfgang Kuch, and Felix Tuczek. Spin-Crossover Complex on Au(111): Structural and Electronic Differences Between Mono- and Multilayers. *Chem. - Eur. J.*, 19:15702–15709, 2013.

[132] Manuel Gruber, Vincent Davesne, Martin Bowen, Samy Boukari, Eric Beaurepaire, Wulf Wulfhekel, and Toshio Miyamachi. Spin state of spin-crossover complexes: From single molecules to ultrathin films. *Physical Review B*, 89:195415, 2014.

[133] Alex Pronschinske, Yifeng Chen, Geoffrey F Lewis, David A Shultz, Arrigo Calzolari, Marco Buongiorno Nardelli, and Daniel B Dougherty. Modification of Molecular Spin Crossover in Ultrathin Films. *Nano Lett.*, 13:1429–1434, 2013.

[134] S Beniwal, X Zhang, S Mu, A Naim, P Rosa, G Chastanet, J-F Letard, J Liu, G E Sterbinsky, D A Arena, P A Dowben, and A Enders. Surface-induced spin state

locking of the [Fe(H_2B(pz)$_2$)$_2$(bipy)] spin crossover complex. *Journal of Physics: Condensed Matter*, 28:206002, 2016.

[135] Tatiana Palamarciuc, Jenny C Oberg, Fadi El Hallak, Cyrus F Hirjibehedin, Michele Serri, Sandrine Heutz, Jean-François Létard, and Patrick Rosa. Spin crossover materials evaporated under clean high vacuum and ultra-high vacuum conditions: from thin films to single molecules. *Journal of Materials Chemistry*, 22:9690–9695, 2012.

[136] P E Blöchl. Projector augmented-wave method. *Phys. Rev. B*, 50:17953–17979, 1994.

[137] G Kresse and J Hafner. *Ab initio* molecular dynamics for open-shell transition metals. *Phys. Rev. B*, 48:13115–13118, 1993.

[138] G Kresse and J Furthmüller. Efficient iterative schemes for *ab initio* total-energy calculations using a plane-wave basis set. *Phys. Rev. B*, 54:11169–11186, 1996.

[139] Jose Antonio Real, M Carmen Munoz, Juan Faus, , and Xavier Solans. Spin Crossover in Novel Dihydrobis(1-pyrazolyl)borate [H_2B(pz)$_2$]-Containing Iron(II) Complexes. Synthesis, X-ray Structure, and Magnetic Properties of [FeL(H_2B(pz)$_2$)$_2$] (L = 1,10-Phenanthroline and 2,2-Bipyridine). *Inorganic Chemistry*, 36:3008–3013, 1997.

[140] A I Liechtenstein, V I Anisimov, and J Zaanen. Density-functional theory and strong interactions: Orbital ordering in mott-hubbard insulators. *Phys. Rev. B*, 52:R5467–R5470, 1995.

[141] Thiruvancheril G Gopakumar, Francesca Matino, Holger Naggert, Alexander Bannwarth, Felix Tuczek, and Richard Berndt. Electron-Induced Spin Crossover of Single Molecules in a Bilayer on Gold. *Angew. Chem. Int. Ed.*, 51:6262–6266, 2012.

[142] Alex Pronschinske, Robert C Bruce, Geoff Lewis, Yifeng Chen, Arrigo Calzolari, Marco Buongiorno-Nardelli, David A Shultz, Wei You, and Daniel B Dougherty. Iron(II) spin crossover films on Au(111): scanning probe microscopy and photoelectron spectroscopy. *Chem. Comm.*, 49:10446–10452, 2013.

[143] R P Gupta and S K Sen. Calculation of multiplet structure of core p-vacancy levels. *Phy. Rev. B*, 10:71–77, 1974.

[144] Shi Cao, Tula R Paudel, Kishan Sinha, Xuanyuan Jiang, Wenbin Wang, Evgeny Y Tsymbal, Xiaoshan Xu, and Peter A Dowben. The stability and surface termination of hexagonal $LuFeO_3$. *J. Phys. Cond. Mat.*, 27:175004, 2015.

[145] A P Grosvenor, B A Kobe, M C Biesinger, and N S McIntyre. Investigation of multiplet splitting of Fe 2p XPS spectra and bonding in iron compounds. *Surf. Inter. Anal.*, 36:1564–1574, 2004.

[146] R P Gupta and S K Sen. Calculation of multiplet structure of core p -vacancy levels. II. *Phys. Rev. B*, 12:15, 1975.

[147] Edward C Ellingsworth, Brittany Turner, and Greg Szulczewski. Thermal conversion of $[Fe(phen)_3](SCN)_2$ thin films into the spin crossover complex $Fe(phen)_2(NCS)_2$. *RSC Adv.*, 3:3745–3754, 2013.

[148] L Y Johansson, R Larsson, J Blomquist, C Cederström, S Grapengiesser, U Helgeson, L C Moberg, and M Sundbom. X-ray photoelectron and Mössbauer spectroscopy on a variety of iron compounds. *Chem. Phys. Lett.*, 24:508–513, 1974.

[149] Luis J Matienzo, William E Swartz, and Samuel O Grim. X-ray photoelectron spectroscopy of tetrahedral and square planar nickel(II) compounds. *Inorg. Nucl. Chem. Lett.*, 12:2762–2769, 1972.

[150] K Burger, H Ebel, and K Madeja. The effect of spin states of iron[II] on the XPS of its mixed complexes. *J. Elect. Spec. Rel. Phen.*, 28:115–121, 1982.

[151] Peter C J Graat and Marcel A J Somers. Simultaneous determination of composition and thickness of thin iron-oxide films from XPS Fe 2p spectra. *Appl. Surf. Sci.*, 100:36–40, 1996.

[152] Tien-Chih Lin, Gayatri Seshadri, and Jeffry A Kelber. A consistent method for quantitative XPS peak analysis of thin oxide films on clean polycrystalline iron surfaces. *Appl. Surf. Sci.*, 119:83–92, 1997.

[153] T Yamashita and P Hayes. Analysis of XPS spectra of Fe^{2+} and Fe^{3+} ions in oxide materials. *Appl. Surf. Sci.*, 254:2441–2449, 2008.

[154] Li Song, Zheng Liu, Arava Leela Mohana Reddy, Narayanan Tharangattu Narayanan, Jaime Taha-Tijerina, Juan Peng, Guanhui Gao, Jun Lou, Robert Vajtai, and Pulickel M Ajayan. Binary and Ternary Atomic Layers Built from Carbon, Boron, and Nitrogen. *Adv. Mater.*, 24:4878–4895, 2012.

[155] S Azevedo and R de Paiva. Structural stability and electronic properties of carbon-boron nitride compounds. *Eur. Phys. Lett.*, 75:126, 2006.

[156] S Bhandary and B Sanyal. *Graphene-Boron Nitride Composite: A Material with Advanced Functionalities*. IntechOpen, 2012.

[157] Q Peng, A Zamiri, and S De. Tunable Band Gaps of Mono-layer Hexagonal BNC Heterostructures. *arXiv: cond. mat*, 2011.

[158] Jun Zhu, Sumanta Bhandary, Biplab Sanyal, and Henrik Ottosson. Interpolation of Atomically Thin Hexagonal Boron Nitride and Graphene: Electronic Structure and Thermodynamic Stability in Terms of All-Carbon Conjugated Paths and Aromatic Hexagons. *J. Phys. Chem. C*, 115:10264–10271, 2011.

[159] Amy Y Liu, Renata M. Wentzcovitch, and Marvin L Cohen. Atomic arrangement and electronic structure of BC_2N . *Phys. Rev. B*, 39:1760–1765, 1989.

[160] Lei Liu, Jewook Park, David A Siegel, Kevin F McCarty, Kendal W Clark, Wan Deng, Leonardo Basile, Juan Carlos Idrobo, An-Ping Li, and Gong Gu. Heteroepitaxial Growth of Two-Dimensional Hexagonal Boron Nitride Templated by Graphene Edges. *Science*, 343:163–167, 2014.

[161] Dacheng Wei, Yunqi Liu, Yu Wang, Hongliang Zhang, Liping Huang, and Gui Yu. Synthesis of N-Doped Graphene by Chemical Vapor Deposition and Its Electrical Properties. *Nano Lett.*, 9:1752–1758, 2009.

[162] Wenlong Wang, Yoshio Bando, Chunyi Zhi, Wangyang Fu, Enge Wang, and Dmitri Golberg. Aqueous Noncovalent Functionalization and Controlled Near-Surface Carbon Doping of Multiwalled Boron Nitride Nanotubes. *J. Am. Chem. Soc.*, 130:8144–8145, 2008.

[163] Yongji Gong, Gang Shi, Zhuhua Zhang, Wu Zhou, Jeil Jung, Weilu Gao, Lulu Ma, Yang Yang, Shubin Yang, Ge You, Robert Vajtai, Qianfan Xu, Allan H MacDonald, Boris I Yakobson, Jun Lou, Zheng Liu, and Pulickel M Ajayan. Direct chemical conversion of graphene to boron- and nitrogen- and carbon-containing atomic layers. *Nat. Comm.*, 5:1–8, 2014.

[164] Regis Decker, Yang Wang, Victor W Brar, William Regan, Hsin-Zon Tsai, Qiong Wu, William Gannett, Alex Zettl, and Michael F Crommie. Local Electronic Properties of Graphene on a BN Substrate via Scanning Tunneling Microscopy. *Nano Lett.*, 11:2291–2295, 2011.

[165] Lijie Ci, Li Song, Chuanhong Jin, Deep Jariwala, Dangxin Wu, Yongjie Li, Anchal Srivastava, Z. F. Wang, Kevin Storr, Luis Balicas, Feng Liu, and Pulickel M Ajayan1. Atomic layers of hybridized boron nitride and graphene domains. *Nat. Mat.*, 9:430–435, 2010.

[166] Suo Zhu Bai, Bin Yao, Guo Zhong Xing, Ke Zhang, and Wen-Hui Su. Synthesis, conductivity and high-pressure phase transition of amorphous boron carbon nitride. *Phys. B Cond. Mat.*, 396:214–219, 2007.

[167] Md. Abdul Mannan, Masamitsu Nagano, Tetsuya Kida, Norie Hirao, and Yuji Baba. Characterization of BCN films synthesized by radiofrequency plasma enhanced chemical vapor deposition. *J. Phys. Chem. Sol.*, 70:20–25, 2009.

[168] Md. Abdul Mannan, Hideyuki Noguchi, Tetsuya Kida, Masamitsu Nagano, Norie Hirao, and Yuji Baba. Chemical bonding states and local structures of the oriented hexagonal BCN films synthesized by microwave plasma CVD. *Mat. Sci. Semi. Pro.*, 11:100–105, 2008.

[169] Md. Abdul Mannan, Hideyuki Noguchi, Tetsuya Kida, Masamitsu Nagano, Norie Hirao, and Yuji Baba. Growth and characterization of stoichiometric BCN films on highly oriented pyrolytic graphite by radiofrequency plasma enhanced chemical vapor deposition. *Thin Solid Films*, 518:4163–4169, 2010.

[170] Md. Abdul Mannan, Yuji Baba, Tetsuya Kida, Masamitsu Nagano, Iwao Shimoyama, Norie Hirao, and Hideyuki Noguchi. Orientation of B-C-N hybrid films deposited on Ni (111) and polycrystalline Ti substrates explored by X-ray absorption spectroscopy. *Thin Solid Films*, 519:1780–1786, 2011.

[171] A Perrone, A P Caricato, A Luches, M Dinescu, C Ghica, V Sandu, and A Andrei. Boron carbonitride films deposited by pulsed laser ablation. *Applied Surface Science*, 133:239–242, 1998.

[172] H Ling, J D Wu, J Sun, W Shi, Z F Ying, and F M Li. Electron cyclotron resonance plasma-assisted pulsed laser deposition of boron carbon nitride films. *Diamond and Related Materials*, 11:1623–1628, 2002.

[173] W L Wang, X D Bai, K H Liu, Z Xu, D Golberg, Y Bando, and E G Wang. Direct Synthesis of B-C-N Single-Walled Nanotubes by Bias-Assisted Hot Filament Chemical Vapor Deposition. *J. Am. Chem. Soc.*, 128:6530–6531, 2006.

[174] K Suenaga, C Colliex, N Demoncy, A Loiseau, H Pascard, and F Willaime. Synthesis of Nanoparticles and Nanotubes with Well-Separated Layers of Boron Nitride and Carbon. *Science*, 278:653–655, 1997.

[175] Gang Chen, Lev N Zakharov, Mark E Bowden, Abhijeet J Karkamkar, Sean M Whittemore, Edward B Garner, Tanya C Mikulas, David A Dixon, Tom Autrey, and Shih-Yuan Liu. Bis-BN Cyclohexane: A Remarkably Kinetically Stable Chemical Hydrogen Storage Material. *J. Am. Chem. Soc.*, 137:134–137, 2015.

[176] Alpha T N'Diaye, Johann Coraux, Tim N Plasa, Carsten Busse, and Thomas Michely. Structure of epitaxial graphene on Ir(111). *New Journal of Physics*, 10:043033, 2008.

[177] D Usachov, A Fedorov, O Vilkov, V K Adamchuk, L V Yashina, L Bondarenko, A A Saranin, A Grüneis, and D V Vyalikh. Experimental and computational insight into the properties of the lattice-mismatched structures: Monolayers of h-BN and graphene on Ir(111). *Phys. Rev. B*, 86:155151, 2012.

[178] M O Watanabe, S Itoh, K Mizushima, and T Sasaki. Bonding characterization of BC2N thin films. *Applied Physics Letters*, 68:2962–2964, 1996.

[179] A B Preobrajenski, May Ling Ng, A S Vinogradov, and N Mrtensson. Controlling graphene corrugation on lattice-mismatched substrates. *Phys. Rev. B*, 78:073401, 2008.

[180] Md Nizam Uddin, Iwao Shimoyama, Yuji Baba, Tetsuhiro Sekiguchi, and Masamitsu Nagano. X-ray photoelectron spectroscopic observation on BCN hybrids synthesized by ion beam deposition of borazine. *JVST A*, 23:497–502, 2005.

[181] Wieslaw A Zdaniewski and Nancy L Brungard. X-ray Photoelectron Spectroscopy Studies of Metallic Diborides. *Journal of the American Ceramic Society*, 75:2849–2856, 1992.

[182] G Mavel, J Escard, P Costa, and J Castaing. ESCA surface study of metal borides. *Surface Science*, 35:109 – 116, 1973.

[183] J P Riviere, Y Pacaud, and M Cahoreau. Spectroscopic studies of BN films deposited by dynamic ion mixing. *Thin Solid Films*, 227:44 – 53, 1993.

[184] Emmanuel C Onyiriuka. Aluminum, Titanium Boride, and Nitride Films Sputter-Deposited from Multicomponent Alloy Targets Studied by XPS. *Applied Spectroscopy*, 47(1):35–37, 1993.

[185] Arunima K Singh, Kiran Mathew, Houlong L Zhuang, and Richard G Hennig. Computational Screening of 2D Materials for Photocatalysis. *Journal of Physical Chemistry Letters*, 6:1087–1098, 2015.

[186] Mengxi Liu, Yuanchang Li, Pengcheng Chen, Jingyu Sun, Donglin Ma, Qiucheng Li, Teng Gao, Yabo Gao, Zhihai Cheng, Xiaohui Qiu, Ying Fang, Yanfeng Zhang, and Zhongfan Liu. Quasi-Freestanding Monolayer Heterostructure of Graphene and Hexagonal Boron Nitride on Ir(111) with a Zigzag Boundary. *Nano Letters*, 14:6342–6347, 2014.

[187] Martina Corso, Willi Auwärter, Matthias Muntwiler, Anna Tamai, Thomas Greber, and Jürg Osterwalder. Boron Nitride Nanomesh. *Science*, 303(5655):217–220, 2004.

[188] Fabian Schulz, Robert Drost, Sampsa K. Hämäläinen, Thomas Demonchaux, Ari P. Seitsonen, and Peter Liljeroth. Epitaxial hexagonal boron nitride on Ir(111): A work function template. *Phys. Rev. B*, 89:235429, 2014.

[189] A N Caruso, P A Dowben, S Balkir, Nathan Schemm, Kevin Osberg, R W Fairchild, Oscar Barrios Flores, Snjezana Balaz, A D Harken, B W Robertson, and J I Brand. The all boron carbide diode neutron detector: Comparison with theory. *Materials Science and Engineering: B*, 135:129–133, 2006.

[190] K Osberg, N Schemm, S Balkir, J I Brand, M S Hallbeck, P A Dowben, and M W Hoffman. A Handheld Neutron-Detection Sensor System Utilizing a New Class of Boron Carbide Diode. *IEEE Sensors Journal*, 6:1531–1538, 2006.

[191] B W Robertson, S Adenwalla, A Harken, P Welsch, J I Brand, P A Dowben, and J P Claassen. A class of boron-rich solid-state neutron detectors. *Applied Physics Letters*, 80:3644–3646, 2002.

[192] Nina Hong, John Mullins, Keith Foreman, and S Adenwalla. Boron carbide based solid state neutron detectors: the effects of bias and time constant on detection efficiency. *Journal of Physics D: Applied Physics*, 43:275101, 2010.

[193] I. Lita and D. A. Visan. Implementation of a conditioning circuit for radiation detectors. In *Design and Technology in Electronic Packaging (SIITME), 2011 IEEE 17th International Symposium for*, pages 241–244, 2011.

[194] Anthony N Caruso, Ravi B Billa, Snjezana Balaz, Jennifer I Brand, and P A Dowben. The heteroisomeric diode. *Journal of Physics: Condensed Matter*, 16:L139, 2004.

[195] E Day, M J Diaz, and S Adenwalla. Effect of bias on neutron detection in thin semiconducting boron carbide films. *Journal of Physics D: Applied Physics*, 39:2920, 2006.

[196] A N Caruso. The physics of solid-state neutron detector materials and geometries. *Journal of Physics: Condensed Matter*, 22:443201, 2010.

[197] S Balaz, D I Dimov, N M Boag, K Nelson, B Montag, J I Brand, and P A Dowben. The electronic structure of 1,2-$PCB_{10}H_{11}$ molecular films: a precursor to a novel semiconductor. *Applied Physics A*, 84:149–159, 2006.

[198] Eckart Ruhl, Norman F Riehs, Swayambhu Behera, Justin Wilks, Jing Liu, H-W Jochims, Anthony N Caruso, Neil M Boag, Jeffry A Kelber, and Peter A Dowben. Photofragmentation of the closo-Carboranes Part II: VUV Assisted Dehydrogenation in the closo-Carboranes and Semiconducting $B_{10}C_2H_x$ Films. *Journal of Physical Chemistry A*, 114:7284–7291, 2010.

[199] Swayambhu Behera, Justin Wilks, Peter A Dowben, M Sky Driver, A N Caruso, and Jeffry A Kelber. Photo-induced site-specific nitridation of plasma-deposited $B_{10}C_2H_x$ films: A new pathway toward post-deposition doping of semiconducting boron carbides. *Surface Science*, 604:L51–L54, 2010.

[200] Frank L. Pasquale, Jing Liu, P.A. Dowben, and Jeffry A. Kelber. Novel semiconducting alloy polymers formed from ortho-carborane and 1,4-diaminobenzene. *Materials Chemistry and Physics*, 133:901–906, 2012.

[201] D N McIlroy, S-D Hwang, K Yang, N Remmes, P A Dowben, A A Ahmad, N J Ianno, J Z Li, J Y Lin, and H X Jiang. The incorporation of Nickel and Phosphorus dopants into Boron-Carbon alloy thin films. *Applied Physics A*, 67:335–342, 1998.

[202] Sunwoo Lee, John Mazurowski, G Ramseyer, and P A Dowben. Characterization of boron carbide thin films fabricated by plasma enhanced chemical vapor deposition from boranes. *Journal of Applied Physics*, 72:4925–4933, 1992.

[203] Sunwoo Lee and P A Dowben. The properties of boron carbide/silicon heterojunction diodes fabricated by Plasma-Enhanced Chemical Vapor Deposition. *Applied Physics A*, 58:223–227, 1994.

[204] SeongDon Hwang, N B Remmes, P A Dowben, and D N McIlroy. Nickel doping of boron carbide grown by plasma enhanced chemical vapor deposition. *JJVST B*, 14:2957–2960, 1996.

[205] Frank L Pasquale and Jeffry A Kelber. Site-specific electron-induced cross-linking of ortho-carborane to form semiconducting boron carbide. *Applied Surface Science*, 258:2639 – 2642, 2012.

[206] Colin D Bain and George M Whitesides. Molecular-Level Control over Surface Order in Self-Assembled Monolayer Films of Thiols on Gold. *Science*, 240:62–63, 1988.

[207] Frank L Pasquale, Yun Li, Jincheng Du, and Jeffry A Kelber. Novel alloy polymers formed from ortho -carborane and benzene or pyridine. *Journal of Physics: Condensed Matter*, 25:105801, 2013.